5-1-2013

# Charge Transport Studies of Proton and Ion Conducting Materials

Craig William Versek
*University of Massachusetts - Amherst*, cversek@gmail.com

# CHARGE TRANSPORT STUDIES OF PROTON AND ION CONDUCTING MATERIALS

A Dissertation Presented

by

CRAIG WM. VERSEK

Submitted to the Graduate School of the
University of Massachusetts Amherst in partial fulfillment
of the requirements for the degree of

DOCTOR OF PHILOSOPHY

May 2013

Physics

# CHARGE TRANSPORT STUDIES OF PROTON AND ION CONDUCTING MATERIALS

A Dissertation Presented

by

CRAIG WM. VERSEK

Approved as to style and content by:

Mark Tuominen, Chair

Anthony Dinsmore, Member

Adrian Parsegian, Member

Scott Auerbach, Member

Donald Candela, Department Chair
Physics

# ACKNOWLEDGMENTS

Thanks to my advisor Prof. Mark T. Tuominen, committee members Profs. Anthony Dinsmore, Adrian Parsegian, and Scott Auerbach as well as collaborators Profs. E. Bryan Coughlin, D. Venkataraman, Ryan C. Hayward, S. Thayumanavan. Even more thanks to collaborating grad students and post-docs past and present Michael Thorn, Ozgur Yavuzcetin, Shilpi Sanghi, Surangkhana "Ying" Martwiset, Tsunghan Tsai, Yangbin Chen, Chikkannagari "Mani" Nagamani, Scott Christensen, Dipankar Basak, Usha Viswanathan, Jacob Harvey, Eric Anderson, Dan Miranda, YuYing Tang, and Catherine Walker. Thanks to the talented Physics Department Machine Shop staff Ashley Webb (retired), Walter Pollard, Dick Letendre (deceased, we will miss him), and Rick Miastkowski. Thanks to the rest of the Physics Department staff, especially Jane Knapp, who really helped us navigate all the bureaucracy. Much valuable assistance and stimulating discussion was provided by the former MassCREST facilities director A. Chandrasekaran. Most of all, I would not have come this far without the support of my fiancée Dr. Melissa Eliot and my two fat white cats, Peach and Mario.

# ABSTRACT

## CHARGE TRANSPORT STUDIES OF PROTON AND ION CONDUCTING MATERIALS

MAY 2013

CRAIG WM. VERSEK

B.Sc., CARNEGIE MELLON UNIVERSITY

M.Sc., UNIVERSITY OF MASSACHUSETTS AMHERST

Ph.D., UNIVERSITY OF MASSACHUSETTS AMHERST

Directed by: Professor Mark Tuominen

The development of a high-throughput impedance spectroscopy instrumentation platform for conductivity characterization of ion transport materials is outlined. Collaborative studies using this system are summarized. Charge conduction mechanisms and conductivity data for small molecule proton conducting liquids, pyrazole, imidazole, 1,2,3-triazole, 1,2,4-triazole, and select mixtures of these compounds are documented. Furthermore, proton diffusivity measurements using a Pulse Field Gradient Nuclear Magnetic Resonance (PFG NMR) technique for imidazole and 1,2,3-triazole binary mixtures are compared. Studies of azole functionalized discotic and linear mesogens with conductivity, structural, and thermal characterizations are detailed.

# TABLE OF CONTENTS

# LIST OF TABLES

**Table** **Page**

# LIST OF FIGURES

**Figure** **Page**

# INTRODUCTION

Materials that can transport ions while blocking the flow of electrons play a critical role as separator/electrolyte in many kinds of electrochemical devices. In particular, high performance fuel cells are enabled by thin, yet mechanically robust membranes that conduct protons while preventing cross-over of fuel and oxidizer as well as electrical shorting of the electrodes. Battery applications require electrolytes that transport specific ions into and out of the cathode and anode during reduction and oxidation reactions on charging and discharging cycles. Electrochemical double layer capacitors store charge physically at the electrode/electrolyte interface. Given a particular electrochemical application, a research endeavor to develop novel electrolytes would clearly benefit from the ability to rapidly screen materials without the costly steps of device fabrication; often electrolyte materials synthesized for academic studies actually may not be suitable for integration into full devices, yet the relation between the chemical composition and charge transport properties may point the way to future improvements.

A principle goal of our research efforts has been developing an instrumentation platform for high-throughput conductivity measurement of electrolyte materials within a temperature controlled vacuum or humidified air environment. [60] To this aim we have supplemented commercial impedance spectroscopy instruments with custom hardware fixtures and in-house written automation software. The use of agile software design principles, informatics techniques for data handling and work-flow optimization, and improved experimental protocol has drastically increased the amount and quality of interdisciplinary research projects between our group in the Physics Department and other groups in the Chemistry Department and the Polymer Science

and Engineering Department at the University of Massachusetts Amherst. The details of the materials conductivity informatics platform will be discussed in chapter 2. In the interest of brevity, the collaborative studies on novel solid polymer proton conducting membranes [41] [19] [20] [45] [46], hydroxide ion transport membranes [58], and polymer lithium ion electrolytes [43] [61] [2] will be summarized in chapter 3.

We have commenced work to investigate the charge transport properties of particular low-melting point small molecule proton conducting liquids. The nitrogen heterocycles imidazole, pyrazole, 1,2,3-triazole and 1,2,4-triazole have amphiprotic amine sites that can accept or donate intrinsic or extrinsic protons, which diffuse anomalously fast along structural reorganizations of extended hydrogen bond networks – a process known as the *Grotthuss mechanism*; these materials might serve as a model system for proton transport in other materials. Interestingly, we have found that some mixtures of these compounds can exhibit conductivities that are enhanced over the pure state as well as extending the temperature range of the liquid state; the use of complementary functionalities might ultimately improve intrinsic material performance while avoiding some complications associated with extrinsic dopants. We have completed characterization of conductivity over elevated and subambient temperatures for these materials – as well as some select mixtures – using a two-probe impedance spectroscopy technique with ion blocking gold-plated electrodes. (See section 4.2.)

Collaborative work [8] has been published on 1,2,3-triazole functionalized discotic mesogens with interesting proton conductivity temperature dependence, which correlates to liquid crystalline phase transitions. (See section 4.3.) A related study [9] has profiled the temperature dependence of proton conductivity with respect to binary mixtures of linear mesogens functionalized with imidazole and 1,2,3-triazole moieties. Phase transitions inferred from differential scanning calorimetry data cor-

respond to regimes of different temperature dependence in the conductivity, which vary depending on the composition. (See section 4.4.)

The diffusion of ions within an electrolyte is often intimately correlated to conduction processes. We measure proton self-diffusivity using $^1$H PFG NMR in 1,2,3-triazole and a few solvent-free liquid mixtures with imidazole within the temperature range from $-10\,^\circ$C to $70\,^\circ$C. These data are compared against conductivity characterizations, and the concept of the *Haven ratio* – the ratio of the tracer diffusivity to conductivity-derived diffusivity which measures correlations in these processes – will be examined. (See chapter 5.)

The behavior of interfacial charge distributions of ions depends on the properties of the bulk electrolyte as well as physical and possible chemical interactions at particular electrode material surfaces. To better understand the mechanisms of charge carrier generation and mobility in these proton conducting systems, we have developed plans to investigate the phenomena of electrode polarization using low frequency impedance spectroscopy. However, preliminary results suggest that detailed interfacial effects dominate the response and it may not be possible, except in special cases, to infer additional bulk charge transport properties by modelling this portion of the impedance response. Instead, we will discuss the limitations of the Poisson-Boltzmann model and of the experimental techniques used, as applied to proton conducting liquids. (See chapter 6.)

# CHAPTER 1

# THEORY AND EXPERIMENTAL BACKGROUND

## 1.1 Charge Transport Physics in Electrolytes

Electrolytes are electrically conducting condensed-matter phases in which there are mobile ionic charges. A system composed of an electrolyte phase and at least two other conducting phases at the boundaries, called electrodes, through which electrical current may pass is known as an *electrochemical cell*. The application of a voltage across a pair of electrodes may induce rearrangements of electronic and ionic charge throughout the system and enable transfer of electrons through the simultaneous chemical reactions of *reduction* (a species acquires one or more electron) and *oxidation* (a species loses one or more electron), respectively, at the *cathode* and the *anode*. So called "red-ox" currents are classified as *faradaic* since they follow Faraday's law of electrolysis:

$$n = \frac{It}{zF} \tag{1.1}$$

where $n$ is the number of mols of substance reacted taking $z$ electrons per reaction when a faradaic current $I$ passes for a duration of time $t$; Faraday's constant $F = eN_A = 96,485.3365(21)\,\mathrm{C/mol}$ describes the electric charge of Avogadro's number $N_A = 6.022141 \times 10^{23}\,\mathrm{mol}^{-1}$ of electrons, each carrying fundamental charge $e = 1.6021766 \times 10^{-19}\,\mathrm{C}$. Movement of charges not resulting from chemical changes may also generate currents, typically transient in extent, which do not follow Faraday's law and hence are labelled *non-faradaic*. Bard and Faulkner [6] provide a detailed development of the thermodynamics and kinetics of both faradaic and non-faradaic processes in electrochemical cells. The bulk of the following exposition will

be concerned primarily with the physics that explains non-faradaic charge transport, rather than the chemistry that determines faradaic processes.

### 1.1.1 Electrostatics of Electrolyte Bulk

Poisson's equation applies in the bulk the electrolyte medium and the dielectric constant $\epsilon$ is typically assumed to be uniform, so that:

$$\boldsymbol{\nabla} \cdot \mathbf{E} = -\nabla^2 \phi = -\rho_f / \epsilon, \tag{1.2}$$

relating the divergence of the electric field $\mathbf{E} = -\boldsymbol{\nabla}\phi$ to the local *free charge density* $\rho_f$. As in the case of other conducting systems, rapid reorganization of charge carriers of both signs leads to *electroneutrality*, $\rho_f = 0$, within the bulk of the material. Hence, the interior of macroscopic phases are well approximated using Laplace's equation:

$$\nabla^2 \phi_{\text{bulk}} = 0 \tag{1.3}$$

Thus, all *excess charge densities*, $\rho \neq 0$, and *space-charge gradients*, $\boldsymbol{\nabla}\rho \neq 0$, can be treated as existing only at the boundaries of the electrolyte phase.

### 1.1.2 Dynamics of Electrolytes

The dynamics of an ionic species within an electrolyte phase is conveniently expressed through the definition of its *electrochemical potential*

$$\eta_i(\mathbf{r}, t) = \mu_i(\mathbf{r}, t) + z_i F \phi(\mathbf{r}, t), \tag{1.4}$$

a scalar field with units of energy per mol made up of a *chemical potential* $\mu_i$, which typically depends on *concentrations* and *activities*, and an electrostatic energy due to an *electric potential* $\phi$, where $z_i$ is *ionic charge valance* and $F$ is Faraday's constant.

[47] Electric currents in the electrolyte arise from the *flux* $\mathbf{j}_i(\mathbf{r},t)$ of charged species driven by gradients in their electrochemical potentials:

$$\mathbf{j}_i(\mathbf{r},t) = -c_i(\mathbf{r},t)u_i\boldsymbol{\nabla}\eta_i(\mathbf{r},t), \tag{1.5}$$

where $c_i(\mathbf{r},t)$ is the local *molar concentration* and $u_i$ is the *mobility*. The total local current density within the system is a sum over all the charge fluxes

$$\mathbf{i}(\mathbf{r},t) = F\sum_i z_i\mathbf{j}_i(\mathbf{r},t) \tag{1.6}$$

Additionally, the *continuity equations*

$$\frac{\partial c_i(\mathbf{r},t)}{\partial t} = -\boldsymbol{\nabla}\cdot\mathbf{j}_i(\mathbf{r},t) + R_i(\mathbf{r},t) \tag{1.7}$$

ensure the conservation of charge and mass locally, and the source terms $R_i$ allow for transmission at interfaces and the generation or recombination of charge carriers in the bulk. Specification of appropriate forms for the chemical potentials and boundary conditions yields a coupled system of partial differential equations that can be solved for concentration and current profiles.

### 1.1.3 Conductivity of Electrolytes

In the absence of all charge gradients (all $\mu_i(\mathbf{r},t)$ are spatially homogeneous) the form of the electrochemical potential eq. 1.4 reduces to that of the electric potential - within a constant term, such that the driving force for ionic currents is simply

$$-\boldsymbol{\nabla}\eta_i(\mathbf{r},t) = -z_iF\boldsymbol{\nabla}\phi(\mathbf{r},t) = z_iF\mathbf{E} \tag{1.8}$$

Such a concentration gradient free scenario can be created by allowing charge to pass reversibly through the boundaries of the system or, with charge-blocking boundary

conditions, by switching the direction of the electric field quickly enough that charge does not have sufficient time to accumulate at the interfaces. If we assume the application of a spatially uniform electric field, then current will flow in the same direction. Hence, the total current density eq. 1.6 follows Ohm's law

$$i = \sigma \left| \mathbf{E} \right|, \tag{1.9}$$

where

$$\sigma = F^2 \sum_i z_i^2 c_i u_i, \tag{1.10}$$

an intensive quantity, is referred to as the *conductivity* of the bulk electrolyte. More generally, conductivity can be a tensor quantity, possibly showing anisotropic dependence in certain materials, such as single crystals, aligned liquid crystals, and morphologically aligned polymers.

For example, a uniform electric field can be created by controlling the voltage $V$ across parallel plate electrodes with cross-sectional area $A$ and separation $d$, such that $|\mathbf{E}| = V/d$. The total current is directed with the electric field, perpendicular to the plates

$$I = Ai = \left( \frac{A\sigma_\perp}{d} \right) V = (1/R)V \tag{1.11}$$

where $R$ is identified here as the *resistance* to ionic current directed through the electrolyte volume perpendicular to the electrodes – an extensive quantity. As stated previously, this ohmic behavior for electrolytes only applies when charge gradients are effectively absent. The *through-plane conductivity* can be equated to

$$\sigma_\perp = \frac{d}{AR}, \tag{1.12}$$

suggesting various methods for determination of this intensive quantity from experimentally measurable extensive quantities – one of which is described in the Impedance Spectroscopy subsection 1.2.4 "Modelling Electrolyte in Blocking Cell".

## 1.2 Impedance Spectroscopy

Impedance Spectroscopy (IS) is a versatile experimental technique for probing the transport of charges in electrochemical systems using a small amplitude sinusoidal perturbing voltage over a spectrum of frequencies; accurate analysis assumes the measurement of a linear current response in steady state, where, in general, the magnitude and relative phase depend on frequency. The *impedance transfer function* (or just *impedance*), which maps the system response at each frequency to a magnitude and phase-shift or to in-phase *resistance* and 90° out-of-phase *reactance* components, can be computed either with analog circuitry or in software by dividing the input voltage signal by the output current signal in frequency domain representation. A typical experimental application of IS is to model contiguous portions of the measured impedance spectrum with that of equivalent circuits composed of ideal elements; complex nonlinear least squares (CNLS) analysis is then used to find best fit parameters of the model.[38]

### 1.2.1 Frequency Domain Analysis of the Impedance Function

The mathematics for this linear alternating current (AC) system is simplified by working with complex-valued voltage and current variables expressed in the frequency domain

$$\tilde{V}(\omega) = V_0 e^{j\omega t}$$

$$\tilde{I}(\omega) = I_0\left(\omega\right) e^{j(\omega t - \theta(\omega))}$$

that are related to the real-valued time domain voltage and current signals as

$$v(t) \equiv \mathrm{Re}\left\{\tilde{V}\right\} = V_0 \cos(\omega t)$$

$$i(t) \equiv \mathrm{Re}\left\{\tilde{I}\right\} = I_0(\omega)\cos(\omega t - \theta(\omega)), \tag{1.13}$$

where $j \equiv \sqrt{-1}$ and $\theta$ is the phase difference between the signals. An analogy of Ohm's law can now be made for AC systems by defining the complex *impedance* function

$$Z(\omega) = \frac{\tilde{V}(\omega)}{\tilde{I}(\omega)} = |Z|e^{j\theta} \tag{1.14}$$

which is a time independent quantity with a frequency dependent phase $\theta$ and magnitude $|Z| = V_0/I_0(\omega)$.

### 1.2.2 Data Representation

Impedance can be expressed in complex plane coordinates using the following definitions

$$Z(\omega) = Z' + Z''j$$

$$Z' \equiv \mathrm{Re}\{Z\} = |Z|\cos(\theta)$$

$$Z'' \equiv \mathrm{Im}\{Z\} = |Z|\sin(\theta) \tag{1.15}$$

or converted back to polar coordinates using

$$|Z| = \sqrt{Z'^2 + Z''^2} \tag{1.16}$$

$$\theta = \arctan(Z''/Z') \tag{1.17}$$

A vector diagram, known as the *Nyquist plot* can be constructed by associating $Z'$ and $Z''$, respectively, with the $x$ and $y$ coordinates of a plane - by convention the $y$-axis is typically inverted. Also, graphs of $|Z|$ and $\theta$ vs. $\log(\omega)$, called *Bode plots*, are frequently used for representing impedance spectral data.

### 1.2.3 Impedance Analysis of Electrical Circuits

The derivation of impedance transfer functions is a powerful tool for analyzing the frequency response of two-terminal electrical circuit networks composed of resistors, capacitors, inductors, and other elements in series and parallel combinations. In turn,

circuit networks provide a means to model the complex electrical response measured in impedance spectroscopy experiments, since separate charge transport processes can often be modeled as ideal circuit elements. To derive an impedance function for a *linear* circuit element the following *ansatz* procedure can be used: first a linear relation between voltage V, current I, and derivatives of each in the time domain is stated; then, complex sinusoidal voltages and currents will be substituted into the relation accordingly

$$V \to \Delta V e^{j\omega t}$$

$$I \to \Delta I e^{j\omega t}$$

where the symbol $\Delta$ denotes a time independent complex amplitude; and, finally, impedance can be solved for algebraically as

$$Z = \Delta V / \Delta I$$

For two circuit elements, 1 and 2, the impedances of series combinations add,

$$Z_{1,2} = Z_1 + Z_2 \tag{1.18}$$

and the impedances of parallel combinations enter a harmonic mean,

$$Z_{1||2} = \frac{1}{\frac{1}{Z_1} + \frac{1}{Z_2}} \tag{1.19}$$

The behavior of an ideal *resistor* is defined by Ohm's law

$$V = IR \to \Delta V e^{j\omega t} = \Delta I e^{j\omega t} R$$

where R is the resistance, so that the impedance is the frequency independent and purely real (resistive)

$$Z_R = R \tag{1.20}$$

A *capacitor* stores charge $q$ in proportion to an applied voltage, where the capacitance $C$ is the constant of proportionality

$$q = CV$$

The current-voltage defining relation is found by taking the time derivative of the above equation and noting that $I \equiv \frac{dq}{dt}$

$$I = C\frac{dV}{dt} \rightarrow \Delta I e^{j\omega t} = j\omega C \Delta V e^{j\omega t}$$

thus, the impedance is purely imaginary (reactive) at a phase of $-90°$

$$Z_C = 1/j\omega C \tag{1.21}$$

An *inductor* reacts to the changing current through it; accordingly,

$$V = L\frac{dI}{dt} \rightarrow \Delta V e^{j\omega t} = j\omega L \Delta I e^{j\omega t}$$

so that the impedance is also purely imaginary (reactive), but with a phase of $+90°$

$$Z_L = j\omega L \tag{1.22}$$

The *constant phase element* (CPE), which is useful for modelling certain ionic or electrochemical responses, can be "tuned" to have both resistive and reactive behavior. One representation of the CPE impedance

$$Z_{\text{CPE}} = \frac{1}{T(j\omega)^\alpha}, \text{ where } 0 \leq \alpha \leq 1 \tag{1.23}$$

uses an exponent $\alpha$ to yield a complex frequency response and an additional parameter $T$ which suggests a generalized capacitance with frequency dispersion when $0 < \alpha < 1$.

When $\alpha = 1$ the impedance is identical to a capacitor with $C = T$ and when $\alpha = 0$ it is identical to a resistor with $R = 1/T$. Though convenient for curve fitting, this parameter is dimensionally variable such that the units $[T] = \mathrm{s}^{\alpha}/[Z]$ which may complicate its physical interpretation. As the name suggests, the impedance of a CPE gives a line of constant phase angle in the Nyquist plot representation.

A special case of the CPE in which $\alpha = \frac{1}{2}$ gives rise to an *infinite Warburg element* which is useful for modelling charge diffusion processes. The impedance has equal real and imaginary components

$$Z_{\mathrm{W}} = \frac{A_{\mathrm{W}}}{\omega^{\frac{1}{2}}}(1 + j) \tag{1.24}$$

where the $A_{\mathrm{W}}$ is the Warburg coefficient.

### 1.2.4 Modelling an Electrolyte in a Blocking Cell

A simple two-probe cell for measuring the electrical response of materials consists of a sample of thickness $d$ sandwiched between two inert metal electrodes of area $A$. For generality, we will assume that either the voltage across the electrodes or the current through the cell can be controlled as an arbitrary function of time and the corresponding current or voltage response is measured. We will investigate individual aspects of the electrical response that apply to all such cells and motivate analogous circuit elements for these processes. The total cell response can then be modelled as a two terminal circuit composed of series and parallel combinations of these elements and an impedance transfer function $Z$ can be derived as outlined in section 1.2.3.

When an electric field is applied to a material an internal polarization develops extremely rapidly, with time constants on the order of $10^{-16}\,\mathrm{s}$, due to microscopic shifts in bound charges within atoms and molecules [47]; such processes are considered instantaneous with respect to the charge transport being probed by impedance spectroscopy at frequencies of several MHz and below, so can be lumped into a bulk

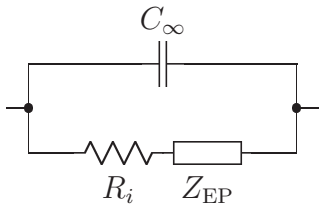


**Figure 1.1.** Equivalent circuit model for idealized two-probe electrolyte measurement.

dielectric constant $\epsilon$. Hence, the infinite frequency dielectric response of the bulk cell can be treated as that of a capacitor with capacitance $C_\infty = \epsilon A/d$.

As shown in section 1.1.3, the application of a sustained electric field over an electrolyte leads to the migration of mobile charge, creating an instantaneous current in direct proportion to the voltage across the electrode; this ion migration current is due to the electrolyte conductivity and can be modeled as an ohmic resistor with resistance $R_i = \frac{d}{A\sigma}$ which must be in parallel to any charging currents from the bulk cell capacitance.

In a cell with charge-blocking electrodes, equal amounts of electronic charge from the electrodes and ionic charge from the electrolyte will build up at the interfaces creating space-charge gradients. The formation of these local charge excesses create countervailing electric fields and, thus, a decay in the transient current until equilibrium is restored, an effect known as *electrode polarization*. Any sub-circuit model of this interfacial response is naturally placed in series with the bulk ionic resistance and in parallel to the bulk cell capacitance.

The frequency response of the electrode polarization which arises from double-layer charging effects (see section 6.3) is often complicated, but typically contains both resistive and reactive components – the qualitative behavior depends on the nature of the electrolyte and electrode interface; for now we will characterize this process as a general impedance $Z_{\mathrm{EP}}$ in series with the ion migration resistance $R_i$ and in parallel to the bulk cell capacitance $C_\infty$. (See figure 1.1.) To satisfy the notion of

charge-blocking electrodes, we specify the rather weak constraint that

$$|Z_{\mathrm{EP}}| \to \infty \text{ as } \omega \to 0 \tag{1.25}$$

i.e., there is no conductivity in the DC limit. Furthermore, the blocking electrode polarization impedance might be considered, fairly generally, as an open ended *ladder network* composed of a finite or infinite continuation of resistances in series with parallel capacitances between each terminal, such that it has the expansion

$$Z_{\mathrm{EP}} = \frac{1}{j\omega C_1 + \frac{1}{R_1 + \frac{1}{j\omega C_2 + \cdots}}} \tag{1.26}$$

### 1.2.5 Experimental Considerations and Corrections

Using the rules of sec. 1.2.3, the total impedance for this charge-blocking electrolyte cell is

$$Z_{\mathrm{cell}} = \frac{1}{j\omega C_\infty + \frac{1}{R_i + Z_{\mathrm{EP}}(\omega)}} \tag{1.27}$$

The bulk processes of electrolyte polarization and conductance may be considered to have a characteristic frequency

$$\omega_0 = \frac{1}{R_i C_\infty} = \frac{\sigma}{\epsilon} \tag{1.28}$$

which is an intrinsic quantity, independent of cell geometry. Often one finds that all of the characteristic frequencies associated with the $RC$ products within the $Z_{\mathrm{EP}}$ expansion are much lower than that of the bulk, since they are associated with double layer capacitances which are typically several orders of magnitude greater than the bulk dielectric capacitance (see section 6.3). If we let $\omega_{\mathrm{EP}}^{max}$ be the highest such frequency, then we have the scenario where $\omega_{\mathrm{EP}}^{max} \ll \omega_0$. Hence, in a sufficiently high

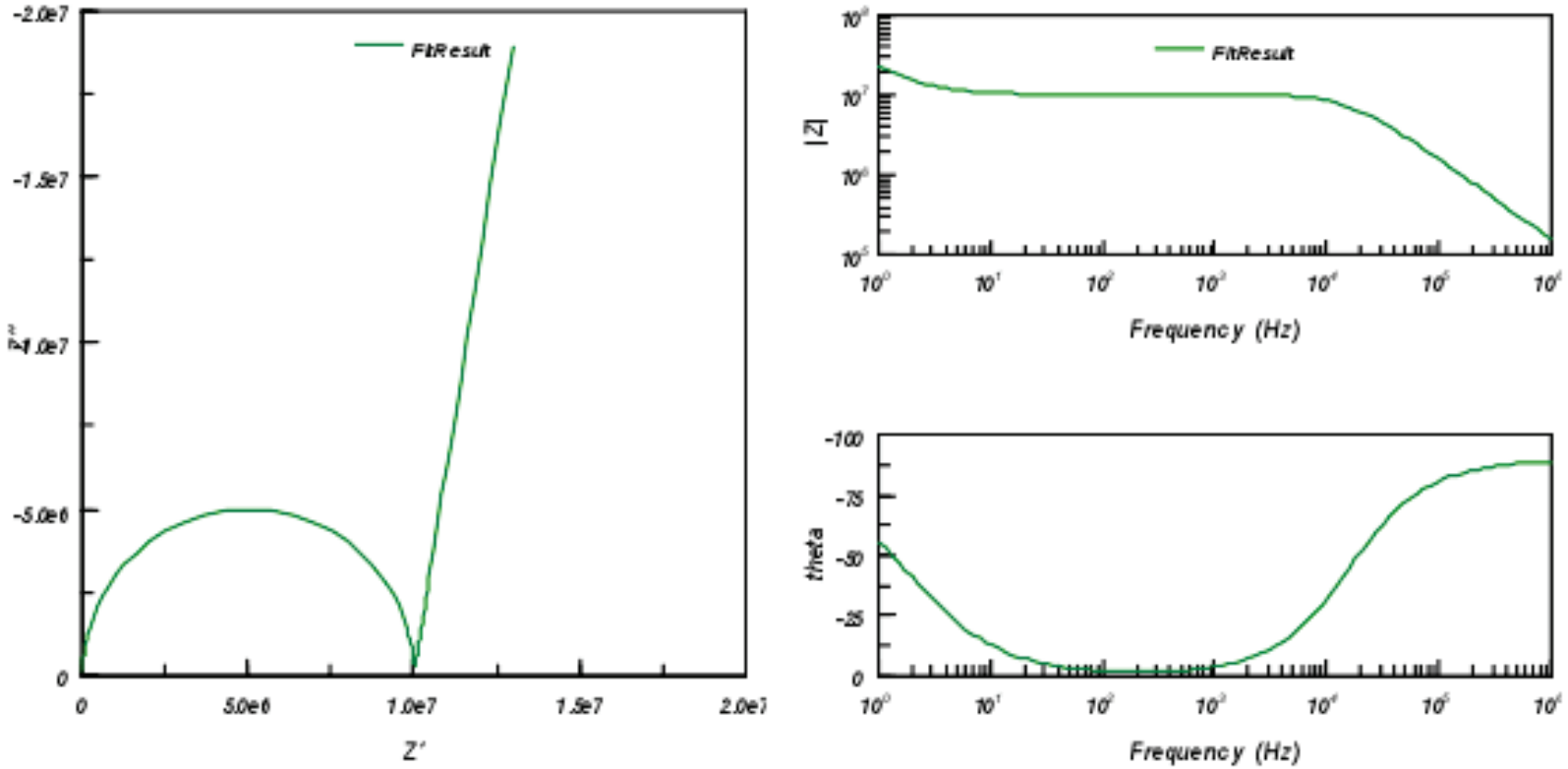


(a) Nyquist plot

(b) Bode plot

**Figure 1.2.** Simulated impedance spectrum for ideal two-probe electrolyte circuit. Here $R_i = 10^7\,\Omega$, $C_\infty = 10^{-12}\,\mathrm{F}$, and $Z_{\mathrm{EP}} = \frac{1}{T(j\omega)^\alpha}$ is modeled as a CPE with $T = 10^{-8}\,\mathrm{s}^\alpha/\Omega$ and $\alpha = 0.9$. Note that the semi-circular arc in the Nyquist diagram represents the bulk dielectric relaxation of the entire cell with time constant $\tau = R_i C_\infty = 10\,\mu\mathrm{s}$ - the frequency at the top corresponds to $f_0 = 1/2\pi\tau \approx 16\,\mathrm{kHz}$. Heading clockwise along the arc (to lower frequencies), $Z'' \to 0$ and $Z' \to R_i$, which corresponds to the plateau region in the bode plot of $|Z|$ spanning 4 orders of magnitude on the frequency axis.

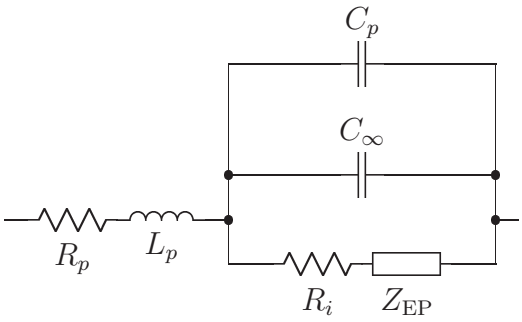


**Figure 1.3.** Equivalent circuit model for two-probe electrolyte measurement with "parasitic" experimental artifacts.

range of frequencies we can ignore all contributions from the electrode polarization, $|Z_{\mathrm{EP}}| \approx 0$, so that the impedance is approximately that of just the bulk contributions

$$Z_{\mathrm{cell}} \approx \frac{R_i}{1 + j\omega R_i C_\infty}, \text{ where } \omega \gg \omega_{\mathrm{EP}}^{max} \tag{1.29}$$

Impedance artifacts due to wiring and cell construction may significantly effect the measured spectra and, if not sufficiently minimized, should at least be accounted for in the modelling of the total cell response. A basic model of "parasitic" impedances consists of a series resistance $R_p$ and inductance $L_p$ and a parallel capacitance $C_p$ with respect to the cell. (See figure 1.3.) In many electrolytes of low conductivity and sufficiently long current paths between electrodes, it may be assumed that $R_p \ll R_i$ and so may be neglected. There are often experimental situations in which the parasitic capacitance $C_p$ of the cabling, in parallel to that of the cell, is on the same order of magnitude or greater than the sample induced capacitance and must be included as a correction, so that

$$\omega_0 = \frac{1}{R_i(C_\infty + C_p)} \neq \frac{\sigma}{\epsilon} \tag{1.30}$$

Parasitic inductance impedances become more significant at higher frequencies and contribute a positive phase shift that may distort the semicircular arcs of the bulk response, especially in the vicinity of the $LC$ resonance $\omega_{LC} = 1/\sqrt{L_p(C_\infty + C_p)}$.

# CHAPTER 2

# MATERIALS CONDUCTIVITY INFORMATICS MIDDLEWARE PLATFORM

As part of the National Science Foundation funded "Center for Fueling the Future" (grant CHE-0739227), we were involved in an interdisciplinary effort to study proton conductivity in specially designed polymer membranes, which are critical fuel cell components. Our team was tasked with characterizing and investigating the bulk proton transport phenomena in these novel materials, synthesized by other teammates from Chemistry and Polymer Science departments. In order to assist the search for highly efficient proton conductors, we decided to take an informatics approach to high-throughput characterization and computer assisted data analysis. Our thought was that if we can automate the measurement of many samples in parallel, then the multivariate space of material properties can more rapidly be explored. Not only will we be able to optimize our chemical design process, we will obtain a more fundamental understanding of the physics of proton transport. Further collaborations have benefited from the experimental infrastructure that we developed in the course of this Phase I grant.

## 2.1 Project Objectives

The typical patterns of experimentation in chemical and materials science are complicated by the heterogeneity of characterization data. Commonly, each experimental station has its own computer running commercial control software that outputs data in a proprietary format. It is left to the researcher to organize and analyze these large,

varied data sets in a systematic fashion. With each scientist having a unique system for record-keeping and data management, it can be difficult for others to investigate the data independently, including within larger multidisciplinary groups. Another challenge comes from the varied ways in which raw data is processed, analyzed, and presented to produce the results of a scientific inquiry. If this information is not somehow standardized, well-annotated and preserved, opportunities for collaboration and data mining could be lost, as well as the integrity of the scientific protocol under which data was collected.

The goals of standardization, accountability, and broad collaboration led us to innovate new research infrastructure and information systems inspired by advances in bioinformatics, business data-flow management, and Internet technologies. Although commercial software laboratory information management systems (LIMS) exist, they have limitations for our work. LIMS are primarily targeted for homogeneous data encountered in the bioinformatics field, are not easily extensible to the specific needs of a new research area, and cannot easily facilitate automated data collection from varied instruments. [48] To address the problem of data format and computational platform heterogeneity, we have leveraged the interoperability and extensibility of open-source software tools and standards.

The project is based on a custom middleware automation framework, named `automat`, using the open-source programming language Python. [1] For analyzing and processing scientific data, Python is quite flexible in handling complex data formats and integrating with other scientific software packages. Our system drives instrumentation and measurement conditions over multiple parameters in a preprogrammed experimental course. This "set it and forget it" approach not only frees up

[1] "Python Programming Language – Official Website", `http://www.python.org`

experimenters' time for more creative tasks, it promotes standardized techniques and quality control of data.

## 2.2 Middleware Framework Architecture

In the experimental informatics systems that we are developing, a set of custom automation programs, the middleware layer, coordinates multiple hardware and software components. We have chosen to code the middleware primarily in the Python programming language, an open source software development environment with a growing user-base in both general purpose and scientific computing applications. The high-level syntax, flexible text and numerical processing, and extensibility of this so called "scripting" language have contributed to its reputation as an excellent "glue" for creating complex applications out of existing software components. [11] Python comes with a large standard library and has numerous third-party extensions which add support for many application domains such as hardware communications interfaces, Internet technologies, database integration, numerical array processing and scientific analysis/visualization. The modular coding style that this programming language encourages makes it ideal for building frameworks of reusable software components. We have taken the initial steps in developing a middleware framework, which we have named `automat`, in order to support laboratory automation and experimental informatics infrastructure.

### 2.2.1 Hardware Interfacing

#### 2.2.1.1 Platform Compatibility

The choice of computing platform and operating system, unfortunately, constrains the range of hardware compatibility that a system builder can achieve. Some manufacturers of instruments choose to design proprietary interfaces which support only one or a strictly limited set of operating systems; such industry trends tend to dis-

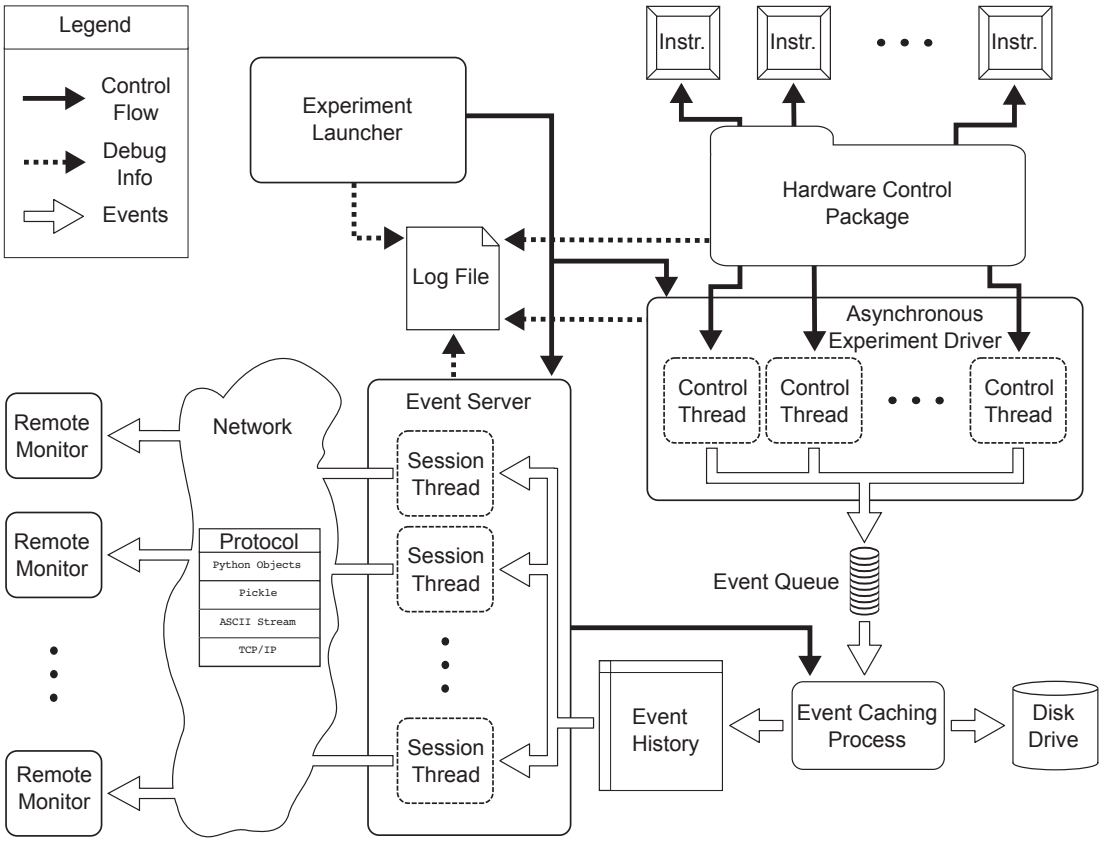


**Figure 2.1.** Schematic representation of the architecture of `automat`, an experimental informatics middleware framework in Python.

advantage computing platforms of secondary popularity, such as the Unix software compatible Linux distributions and Apple's Mac OS X. The developer who wants to build systems using the large base of available Unix compatible open source software with an operating system which provides appropriate support - like the aforementioned - must more carefully consider hardware compatibility issues. Fortunately, many scientific and test instrument manufacturers equip their devices with open interface standards like RS-232 serial buses or the IEEE-488 GPIB protocol. These communication protocols can, in principle, be used within any sufficient programming environment - the Python language has several ways to add support for such protocols. [2] [3] We caution, however, that a device having a standard protocol only solves part of the compatibility problem; the vendor must also provide extensive documentation of the interface – often a set of textual commands – before the end-user can adequately control the instrument with custom middleware components.

#### 2.2.1.2 Code Reusability

Another problem with hardware interfacing that `automat` addresses is how to mitigate the cumbersome low-level details associated with typical communications protocols. It is often the case that several, or even dozens, of commands must be issued to a device to perform a common task. Best practices in the software development community urge programmers not to duplicate literally blocks of similar code, since such behavior can quickly lead to poorly organized, difficult to maintain programs with limited device compatibility. This redundancy of code can be reduced by composing commonly associated commands into higher-level functions, which can be reused with varying inputs and outputs. A set of these high-level control functions - in the Python language - can reside in a single file code module that can be dynam-

[2] "pySerial v2.6 documentation", `http://pyserial.sourceforge.net`

[3] "Linux GPIB Package Homepage ", `http://linux-gpib.sourceforge.net`

ically imported and used by a running application. Such encapsulated modules of code form the basis of an extensible custom software library of reusable instrument control interfaces. More subtle code redundancy and organizational issues arise when one considers a whole collection of interface modules for a diverse set of instruments: How can similar instruments share code in order to enhance code reuse? How might one classify, arrange within a file system, and then retrieve an individual device module? Our framework attempts to tackle this code library organization problem by relying on object-oriented design patterns and special software packaging features of the Python language to create a hierarchy of interfaces of varying generality.

#### 2.2.1.3 The Hardware Control Package

The *hardware control package* of `automat` arranges control modules in a hierarchy of three interface abstraction layers that exploit existing patterns of interface design to enhance code reusability. A hardware interface, in object-oriented programming terms, is a class that encapsulates the methods and data structures needed to implement units of functionality for a type of device. To interact with an actual device, an application must create an *object* of the interface class, providing the necessary initialization information such as the hardware address (e.g., serial port or GPIB address). This interface object provides a "handle" for device control that can be passed to various segments of the program flow. Furthermore, the class-based approach enables a simple mechanism for controlling multiple devices of the same type: an interface object is created for each unique hardware address; the programmer does not need to specify an address in every function call, as is often the case in non-object-oriented implementations. The *model interface* level is the most hardware specific code which refers directly to the communication protocol used for a particular model of instrument. Often manufacturers will release a product line of models which have very similar interfaces with only minor variations; the developer, optionally, can factor

out this overlapping protocol redundancy by creating a higher-level, *make interface*, which can control more than one model from the same vendor. The *make interface* is implemented as a wrapper class, which has a handle on the lower-level *model interface* and exports higher-level functionalities that can be expressed by composing methods common among different models. Likewise, some instruments have functionality similar to those from other manufacturers. If it is convenient to abstract the general functionalities of a whole class of devices, then the programmer can develop an interface at the *type* level, which is a wrapper class for different make interfaces. Only the *model interface* is required to control a particular device, but generalizing the device control with *make* and *type* interfaces can simplify the programming of applications and enable a greater range of compatible devices.

So far we have only discussed the logical structure of the interface hierarchy - the code base itself could be shoved into one big file, split into many files, or even strewn all over the file system. We believe that the best system for organizing the code is to distribute each interface class as a single file module placed within a nested directory structure reflecting the *type*, *make*, *model* logical structure of increasing hardware specificity. Python provides a code importation feature called a "package" which maps portions of a directory tree containing module files to a nested namespace accessible to running applications. Each hardware control module can be categorized into a directory path by specifying the *type* name of the device as the first type subdirectory from the package directory "`devices`," the manufacturer name as the second make subdirectory, and the model name plus the required extension "`.py`" as the module filename, in which the model interface is contained. The more general *make interface* is contained in a module file stored in the *make subdirectory*, where the filename is the make name adjoined to the *device type* name with an underscore character. Similarly, the most general type interface may be found in a module of the same name as the *type* subdirectory in which it is located. Within the Python environment, modules

can be imported by referring to their positions in the package subdirectories in a hard-coded *static import statement*. In order to load modules specified by variables in a configuration file at runtime, we developed a simple *dynamic* loading mechanism, which is a function called `load_device` that locates the file based on its *type*, *make*, *model* classification. This code organization scheme affords developers a means to categorize a large variety of device control modules in an extensible and maintainable system.

For example, consider classifying a Solartron brand potentiostat, model SI1287: the directory path of the module file containing the *model interface*

`devices/potentiostat/solartron/SI1287.py`

the *make interface*

`devices/potentiostat/solartron/solartron_potentiostat.py`

and the *type interface*

`devices/potentiostat/potentiostat.py`

we could load the model interface module with the *hard-coded static import statement*

`from devices.potentiostat.solartron import SI1287` or the module could be loaded dynamically using

```
dev_type = "potentiostat"
dev_make = "solartron"
dev_model = "SI1287"
```

`load_device(dev_type, dev_make, dev_model)` where the values of the three variables `dev_type`, `dev_make`, and `dev_model` could have come from a configuration file. We could extend the package by writing modules for other models of Solartron potentiostats, such as the SI1296, which would share the *make interface* `solartron_potentiostat`. Maybe later we would want to integrate potentiostats made by the Novocontrol company; then, we would add the make subdirectory

`devices/potentiostat/novocontrol/`

and create the make interface module

`devices/potentiostat/novocontrol/novocontrol_potentiostat.py`

and the modules for the various model interfaces.

### 2.2.2 Asynchronous Experiment Driver

Depending on the experiment, the coordination of multiple instruments could be a straight-forward sequential process or it could require a complicated dance involving wait-states, signaling, and event scheduling. Simple experimental tasks, such as a short-duration electronic measurements, can be reasonably expressed as programs involving a single flow of control, which blocks the program until it completes. However, there are often times when a program needs to do several things at once (i.e. "concurrently"), such as control an instrument, monitor the status of a sensor at regular intervals, respond to user input, and plot new data as it arrives; such applications are considered to be input/output (I/O) bound, in contrast to central processing unit (CPU) bound tasks such as involved numerical computations. Trying to accomplish all these disparate tasks sequentially in the same control loop may become a cumbersome and inefficient – if not impossible – programming job when logically independent processes are forced to wait for each other to complete. Python provides a high-level interface for a typical solution to this *concurrency* dilemma for I/O bound programs: allowing for multiple parallel execution flows, or *threads*, to run independently in the same program. [4]

The *multithreading* paradigm opens up a whole new set of challenges to the software developer. All threads execute *asynchronously*, meaning that the time ordering of instructions amongst different threads is not well-defined. While useful for unblock-

[4] "threading – Higher-level threading interface", `http://docs.python.org/2/library/threading.html`

ing logically parallel program sequences, asynchrony complicates the sharing of data and coordination of tasks between threads. Some synchronization can be imposed by using signals to force threads to wait on each others' completion. If used incautiously, multithreading can lead to difficult to debug problems that can appear unpredictably: *race conditions* occur when two or more threads make changes to the same shared object in an unpredictable order, potentially causing data corruption; *deadlock* situations arise when two or more threads are blocked, waiting for signals from each other that will never arrive. [26] To mitigate the potential difficulties caused by non-thread-safe shared data structures and convoluted signaling, the `automat` framework uses a simplified thread interaction model, called the *multiple producer single consumer* pattern. Each thread behaves as a nearly independent process, sharing only one data structure, a standard *queue* container object. (Python's thread-safe `Queue` class [5] automatically implements a synchronization protocol that prevents race conditions.) Signaling between threads should be kept to a minimum, used only for critical functions such as shutdown. Every *producer* thread can perform control and data acquisition tasks on *mutually exclusive* hardware systems and place any generated data onto the queue. Only a single *consumer* thread can remove data from the queue, thus aggregating all inter-thread communications to a single control-point in the code and eliminating any deadlock conditions which might haven arisen in more complicated signaling patterns.

### 2.2.3 Event Processing Subsystem

The queue data structure, which helps to coordinate multiple threads safely, also provides our framework with a mechanism to generalize the flow of information in both sequential and asynchronously controlled experiments. Although queues can contain any arbitrary object in Python, we can standardize the form of this data to

[5] "Queue – A synchronized queue class", `http://docs.python.org/2/library/queue.html`

create a system for passing messages along with packets of information throughout the program. In our framework, we call these messages *events*, which are composed of a pairing of a *string* type identifier and a *dictionary* [6] type associative data mapping. The identifier of the event can be used by subsequent data processing stages in order to extract the information contained within the dictionary, group similar data together, and to parse out meaningful data structures composed from multiple events. Events are created asynchronously by any of the control threads in the program and form a stream from the outgoing end of the *event queue*. (See figure 2.1.) The *event caching process* is the thread that *consumes* these events from the queue and does a few things to manage this stream of information: this process stores all events in a list structure, effectively keeping a history of all the produced data in memory; also, it feeds events to a *parser* object which groups data, recognizes patterns, and then generates data files on disk when sufficient information has arrived. The in-memory *event history* serves a critical function in the remote monitoring system (described later on). Since all events and derived data files are automatically cached on the hard disk, an unexpected interruption of the program does not cause unnecessary data loss. The current event caching model works well for long-running experiments with moderate to slow data rates, but could easily be adapted to quicker data rates by delaying disk writes in order to acquire larger chunks of data in memory or by reducing/compressing the data on the fly.

### 2.2.4 Remote Monitoring

The ability to remotely monitor long-running experiments provides time saving information as well as being a valuable safety feature. `automat` provides generic code modules that take advantage of the event-based information stream to extend experiment automation programs with Internet accessible monitoring capabilities. A

[6] "Mapping Types – dict", `http://docs.python.org/2/library/stdtypes.html#dict`

separate *event server* process, which shares read-only access to the *event history*, can relay events to any number of remotely connecting client programs at any time during the experiment. Tools provided in the standard library allow for the rapid development of a generic multithreaded server [7] with a simple protocol for client-server communications of arbitrary Python objects, like our framework's events. The Python `pickle` module [8] serializes, or "pickles," objects into an ASCII coded format, which can then be transmitted through a file-like stream over an Internet socket using the standard TCP/IP protocol. On the receiving end, objects can be "unpickled" from the socket stream and used in the client program. Upon connecting to the *event server*, a remote monitoring client receives a list of all the events which have been previously generated in the experiment, allowing for the status of the monitor to be made current. Each connection is serviced by a separate thread that automatically updates each monitoring client, sending new events as they arrive.

### 2.2.5 Experiment Configuration and Launching

Experiments utilizing various components of the framework can be launched in several ways. For development simplicity, the needed components can be imported and configured within a single script file which is run from the console. Simple command line arguments may be the most efficient choice of interface for programs without many options. However, for programs with complicated configurations or a need for user interaction, a *graphical user interface* (GUI) might be appropriate. The design of GUI programs is a challenging exercise in itself; fortunately, the event-based multithreaded architecture of `automat` fits well into event-driven GUI paradigms, whereas long-running unthreaded processes would block the handling of user input.

---

[7] "SocketServer – A framework for network servers", `http://docs.python.org/2/library/socketserver.html`

[8] "pickle – Python object serialization", `http://docs.python.org/2/library/pickle.html`

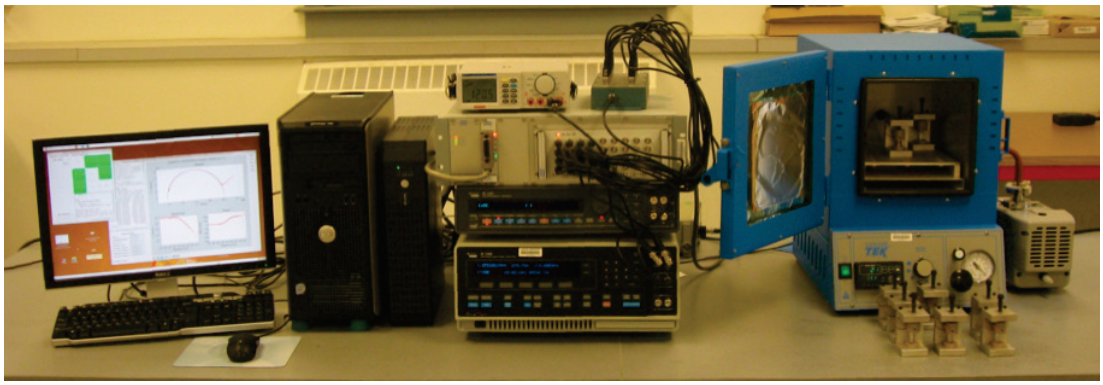

**Figure 2.2.** Hardware for high-throughput conductivity characterization.

Whether it is a console or graphical interface, the *experiment launcher* needs to configure and start the *asynchronous experiment driver*, which is composed of multiple control threads, and optionally start the *event server* process if remote monitoring is enabled. By standardizing the multithreading model and the flow of asynchronously generated data, the *experiment automation framework* aims to provide a toolkit from which developers can rapidly create sophisticated systems of instrument control.

## 2.3 Hardware

The primary system for measurement of materials consists of a Solartron 1260 Impedance/Gain Phase Analyzer that is multiplexed over eight channels of a custom designed sample holder array. Each sample holder fits one of a few standard electrode assemblies, appropriate for solid/polymer samples, confined liquid samples, or in-situ humidified membranes. The array may be placed in a vacuum oven (Cascade TEK TVO-2) for strict anhydrous characterization or in an environmental control chamber (ESPEC SH-241) for equilibration at a precise relative humidity and temperature.

## 2.4 Software

We have developed a robust and extensible suite of programs in the Python language, specifically designed to streamline the collection and analysis of impedance data. This software package, called `pyEIS` (Python Electrochemical Impedance Spectroscopy) is built on top of our `automat` framework.

### 2.4.1 Experiment Launcher

The highly configurable yet convenient `pyEIS` "Experiment Launcher" application (see figure 2.3) allows for precise specification of experimental variables and additional documentation. Two instrument control modes are currently available to schedule measurements at specified temperature set-points or recurrent time intervals, in fully-automated or flexible user-guided experiments. Incoming data points are immediately saved in an accessible format, so that researchers can analyze results *in situ*, guiding further experimental steps.

### 2.4.2 Impedance Analyzer

The automated instrumentation setup is capable of producing more data than can be reasonably analyzed by "old-fashioned" spreadsheet methods, so we've developed tools to improve both the quality and efficiency of subsequent data-reduction steps. The `pyEIS` "Impedance Analyzer" application (see figure 2.4) allows researchers to conveniently extract conductivity values by impedance function fitting and inclusion of user-specified experimental parameters and other metadata, such as geometry factors and temperature. Even while the system is still gathering measurements, results can be analyzed, resumed, and updated with incoming data sets. Conductivity can be plotted as a function of temperature on a standard Arrhenius graph or charted over time, and the reduced data can be exported to spreadsheet formats as well.

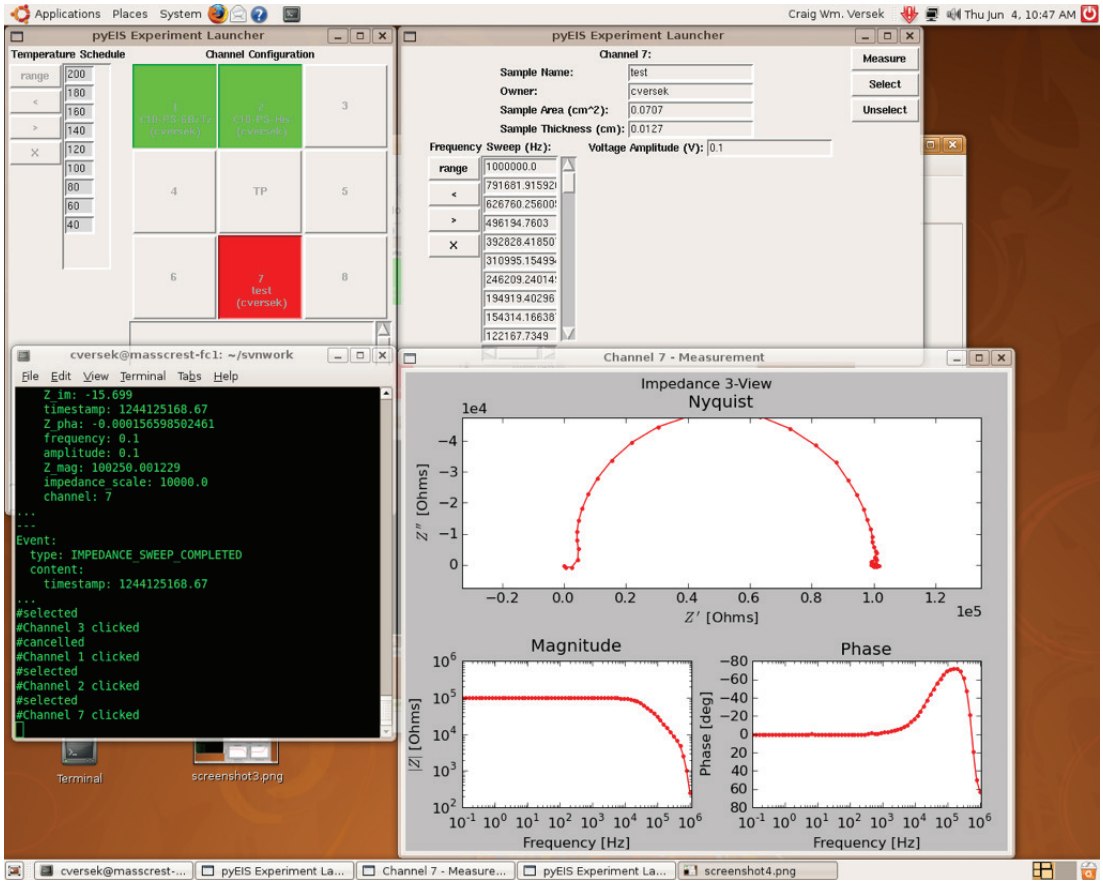


**Figure 2.3.** Screenshot of pyEIS Experiment Launcher software tool.

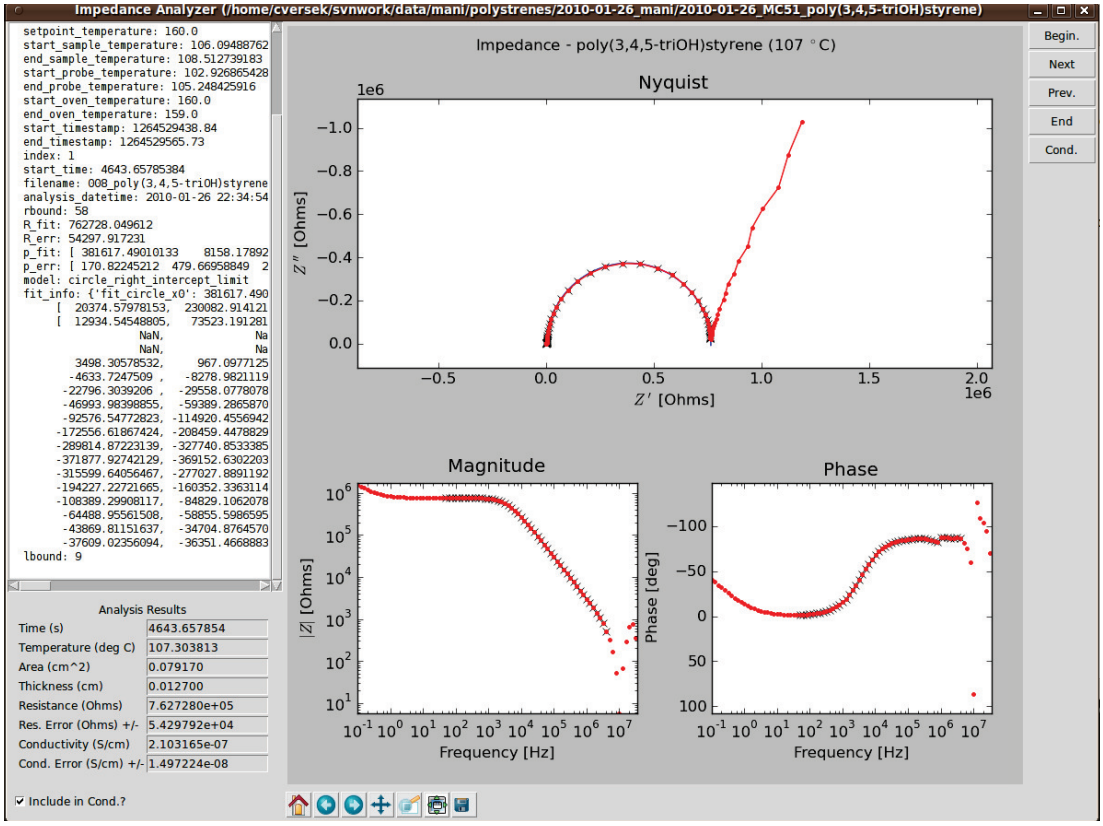


**Figure 2.4.** Screenshot of `pyEIS` Impedance Analyzer software tool.

### 2.4.3 Conductivity Comparison

Experimental projects often involve measurements of multiple samples over extended periods of time, which researchers tend organize according to their own scheme. We have developed software tools which can discover data sets within these informal file-system structures. Raw data sets and associated analysis files are stored in a simple and extensible hierarchical file structure which is backed-up using Subversion open-source version control software. [9] Authorized users can synchronize relevant branches of this data repository to other computers across the Internet, in order to facilitate remote data analysis and sharing of results. The `pyEIS` "Conductivity Comparison" application (see figure 2.5) discovers pre-analyzed conductivity data sets within arbitrarily nested file folders providing a flexible, low-maintenance database-like view which enables rapid sample comparisons. This tool immediately empowers researchers to understand the "big-picture," the often complex interrelation of their systems properties, as well as enabling them to create publication quality plots on the fly.

## 2.5 Experimental Protocol

A new protocol has been developed to ensure accurate measurements under quasi-static thermal equilibrium conditions: the sample is held at high temperature under vacuum while monitoring conductivity at regular time intervals until equilibration is obtained, then the temperature dependence is reported upon slowly cooling to ambient temperature. Conductivity results tend to stabilize after small molecule contaminants diffuse out and any structural annealing progresses to completion. (See example data in figure 2.6.) This technique clarifies the effects of and eliminates

[9] "Apache Subversion", `http://subversion.apache.org`

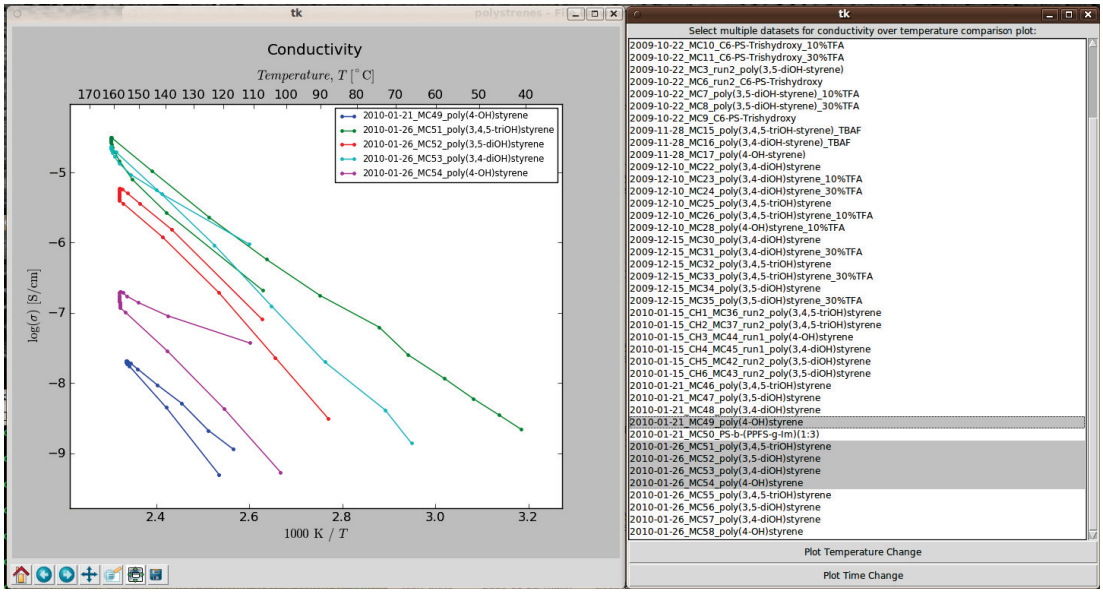


**Figure 2.5.** Screenshot of `pyEIS` Conductivity Comparison software tool.

potential measurement artifacts due to non-equilibrium conditions, such as residual solvent contamination, thermal decomposition, or aging of the morphological state.

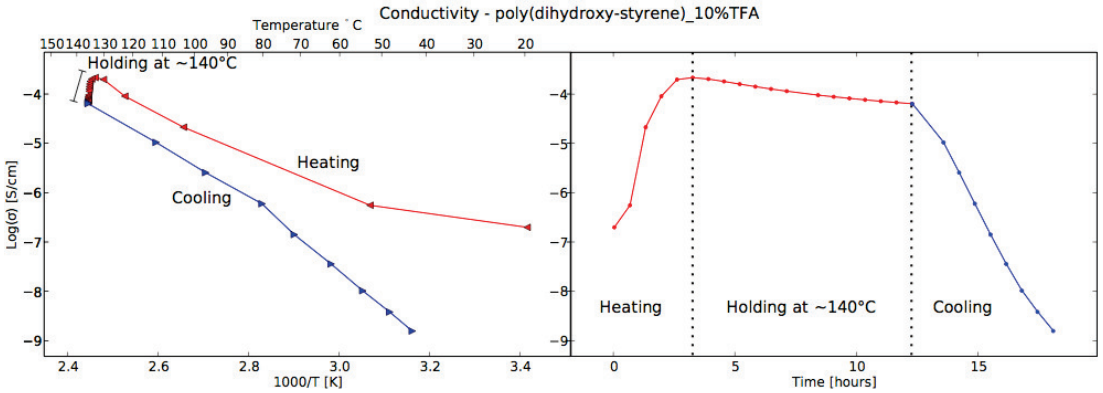


**Figure 2.6.** Example conductivity data illustrating vacuum baking protocol.

# CHAPTER 3

# COLLABORATIVE ION CONDUCTING MATERIAL STUDIES

Our group's interest in ion conducting materials dates back to an initial collaboration with the Coughlin Group in the Polymer Science department at UMass Amherst to develop and characterize novel materials that could conduct protons at high temperatures and low humidities for advanced fuel cell applications. Tuominen Group member Ozgur Yavuzcetin developed the first generation (Electrochemical) Impedance Spectroscopy (EIS) [1] system which was applied to characterize the conductivity of these materials under vacuum conditions and elevated temperatures. (See section 3.2.) This system used a Solartron 1255B Frequency Response Analyzer paired with a Solartron 1287 Electrochemical Interface and a modified Thelco vacuum oven, controlled by custom LabVIEW [2] software. [12] (See figure 3.1(a).)

The start of a new interdisciplinary research center on campus, "Center for Fueling the Future" (NSF grant CHE-0739227), whose focus was a deeper understanding proton transport processes across all length scales in materials, brought increased collaboration to our lab. Colleague Michael Thorn and I were initially supported under this grant and we have participated in many collaborations as a result. (See table

[1]There has been some debate as whether or not to include the "electrochemical" descriptor, since the technique generally extends to more areas than traditional electrochemistry; however, the term "EIS" is used frequently in the proton transport literature and is – in my opinion – a more substantial acronym than "IS".

[2]Laboratory Virtual Instrumentation Engineering Workbench (LabVIEW) [1] is a proprietary development environment from National Instruments which specializes in graphical test and measurement applications.

3.1 for a complete list of publications.) We brought the desire to apply informatics techniques in order to streamline the workflow of the second generation EIS system; our efforts first resulted in a rewrite of the software – still using LabVIEW – in order to improve the temperature control and data logging capabilities of the system. (See figure 3.1(b).) A few studies with collaborators from the Thayumanavan Group (Chemistry Department) were conducted with this version of the system (see section 3.3), but limited capacity and issues with maintenance [3] provided a major bottleneck to ideally productive research.

Fortunately, an equipment and facilities grant (ARO #?) allowed us to redesign the EIS system from scratch for the new Massachusetts Center for Renewable Energy Science and Technology (MassCREST) Charge Transport Laboratory. We developed a custom pluggable sample holder array, [4] virtually "foolproofing" the setup while increasing the measurement capacity to 8 samples. Having purchased all new equipment that needed to be integrated into the system, we decided to use the open source programming language Python in order to develop a scalable application framework which would better accommodate future expansion. (See chapter 2.) The development of this third generation EIS system took a massive amount of effort on both the hardware and software [5] fronts. But this extra work up front paid off – at one point we estimated the EIS usage statistics since the debut of the new system: the sample

---

[3] A user could measure up to 4 samples simultaneously on a good day, but often the fragile high-temperature connections would break, leaving an average of two usable channels. Furthermore, maintaining the software became unwieldy as new features were added.

[4] Credit for machining and design support for the original sample holder array goes to the talented Physics Department Machine Shop staff Ashley Webb (retired) and Walter Pollard. Later machining work for humidity resistant sample holders was performed by – the also talented – Dick Letendre (deceased, we will miss him) and Rick Miastkowski.

[5] A recent count of lines of code (using the Unix command "`find . -name '*.py' | xargs wc -l`" at the package root) totals over $22,000$ in dozens of files. But since Python is a highly expressive language, one can get more done with less code than traditional compiled languages such as C++ and Java which may – according to some Internet guesstimates [56] [5] – take anywhere from 5 to 20 times the lines (in my experience it's been on the upper end).

measurement rate had increased $\sim 4$ times; the raw data output rate increased $\sim 8$ times; and our time to analyze and compare data sets has been reduced by at least 10 times.

**Table 3.1.** Works completed and in progress.

| **Title** | **Type** | **Status** | **Ref.** |
|---|---|---|---|
| "Proton conducting polymers containing 1H-1,2,3-triazole moieties." | Article, *J. Polymer Sci. A* | published, Jan. 2009 | Martwiset [41] |
| "Morphological Effects on Proton Transport in Self-Assembled Anhydrous Polymers" | Poster, *Bulletin of the American Physical Society* | completed, March 2010 | Christensen [20] |
| "Enhancement of anhydrous proton transport by supramolecular nanochannels in comb polymers" | Article, *Nature Chemistry* | published, Apr. 2010 | Chen [19] |
| "Proton conduction in 1H-1,2,3-triazole polymers: Imidazole-like or pyrazole-like?" | Article, *J. Polymer Sci. A* | published, May 2010 | Nagamani [45] |
| "Using Open-Source Scripting Languages for Rapid-Development of Informatics Capabilities" | Presentation, *Nanoinformatics 2010* | completed, Nov. 2010 | Versek [60] |
| "Proton conduction in discotic mesogens" | Communication, *Chem. Commun.* | published, Apr. 2011 | Basak [8] |
| "Importance of dynamic hydrogen bonds and reorientation barriers in proton transport" | Communication, *Chem. Commun.* | published, May 2011 | Nagamani [46] |
| "Block Copolymers Containing Quaternary Benzyl Ammonium Cations for AAEMFC" | Book Chapter, *ACS Symposium Series* | submitted, Aug. 2011 | Tsai [58] |
| "Physicochemical properties of 1,2,3-triazolium ionic liquids" | Article, *RSC Advances* | published, Nov. 2011 | Sanghi [51] |
| "Synthesis and structure–conductivity relationship of PS-block-PVBTMA for alkaline anion exchange membrane fuel cells" | Article, *Journal of Polymer Science Part B: Polymer Physics* | published, Sept. 2012 | Tsai [59] |
| "Cross-linking of Ordered Pluronic/Ionic Liquid Blends for Solid Polymer Electrolytes" | Abstract/Poster, *Bulletin of the American Physical Society* | accepted, March 2012 | Miranda [43] |
| "Incorporation of Functionalized Metal Oxides into PEO Based Solid Polymer Electrolytes for Li-Ion Batteries" | Abstract/Poster, *Bulletin of the American Physical Society* | accepted, March 2012 | Anderson [2] |
| "Anhydrous proton conductivities of squaric acid derivatives" | Communication, *Chemical Communications* | published, April 2012 | Basak [10] |
| "Tunable Networks from Thiol-ene Chemistry for Li-Ion Conduction" | Article, *ACS Macro Letters* | published, May 2012 | Walker [61] |
| "Enhanced anhydrous proton conduction in binary mixtures of ImH/123TzH based compounds" | Article, *Journal of Materials Chemistry* | published, Aug 2012 | Basak [9] |
| Informatics for high-throughput impedance spectroscopy | Manuscript | drafted | Versek |
| Proton conductivity and $1^{H}$ PFG NMR self-diffusion in molten mixtures of imidazole and 1,2,3-triazole | Experiment | completed | Versek |
| Impedance spectroscopy studies of electrode polarization in proton and ion conducting electrolytes | Experiment | halted | Versek |

(a) first generation EIS system

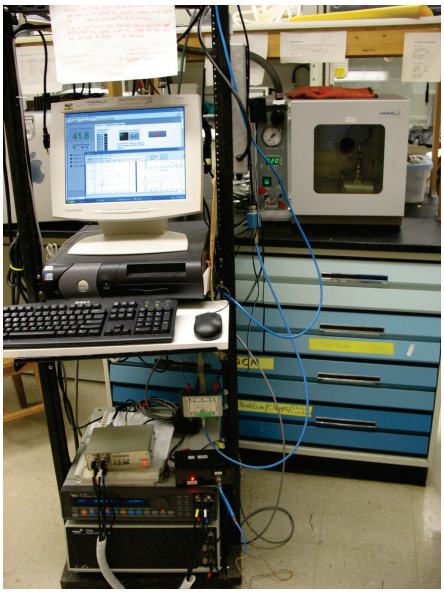

(b) second generation EIS system

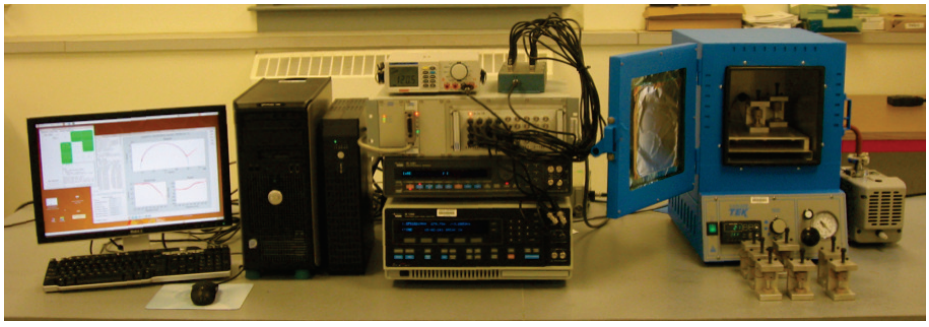

(c) third generation EIS system

**Figure 3.1.** First, second, and third generation Electrochemical Impedance Spectroscopy (EIS) systems for materials conductivity characterization. The hardware used in the first two generations was same: a Solartron 1255B Frequency Response Analyzer paired with a Solartron 1287 Electrochemical Interface and a modified Thelco vacuum oven. The second generation system was a rewrite of the LabVIEW automation code, featuring improved temperature control and data logging. The third generation system (see sections 2.3 and 2.4) was a complete overhaul with a new equipment configuration and custom software developed for the MassCREST Charge Transport Lab.

## 3.1 Polymers for PEM Fuel Cells

In a Proton Exchange Membrane (PEM) fuel cell hydrogen gas is fed to the anode where its electrons are separated with the aid of a catalyst, typically platinum. (See figure 3.2(a).) The electrons supply power to an external circuit while the protons migrate through the PEM and recombine with oxygen and electrons to form water at the cathode, which also typically has a platinum catalyst layer. Operation of a fuel cell of this type at higher temperatures increases reaction rates at the electrodes, allowing for the use of cheaper catalysts like nickel, and furthermore improves the heat management requirements for engineers. [36] Nafion – discovered at DuPont in the late 1960s [50] – is a family of tetrafluoroethylene (Teflon) based copolymers containing sulfonic acid groups (see figure 3.2(b)) which has long been a standard membrane material for PEM fuel cells; though it has high conductivity and chemical stability when it is humidified, Nafion's dependence on liquid water to assist in proton transport limits its application to below $\sim 80\,^{\circ}\mathrm{C}$. [42]

In order to address these problems, research into advanced materials which could efficiently conduct protons at high temperatures ($120 - 200\,^{\circ}\mathrm{C}$) and low humidities ($< 20\,\%\mathrm{RH}$) commenced at UMass Amherst as well as other institutions. Based on ideas popularized by Klaus D. Kreuer and colleagues [36] [37], a new class of anhydrous proton conducting membranes was designed by functionalizing substrates (usually polymers) with amphiprotic groups, such as imidazole [53], benzimidazole [54], and 1,2,3-triazole [66]. Theses amphiprotic functionalities (which can readily donate or accept labile protons) are thought to conduct charge through proton exchange along hydrogen bonded networks, followed by subsequent reorientation step that resets the pathways – a process known as the *Grotthuss mechanism*. (See section 4.2.)

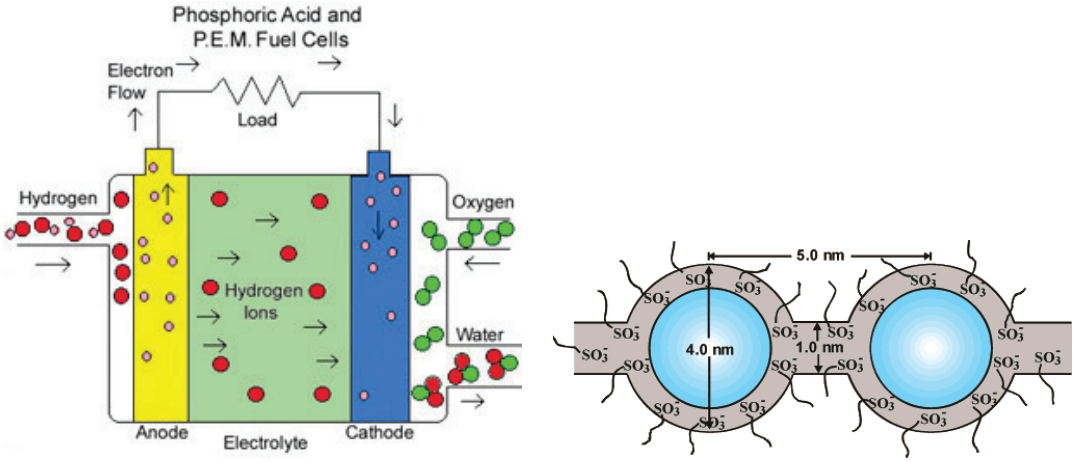


(a) PEM fuel cell

(b) morphology of Nafion

**Figure 3.2.** Operation of PEM fuel cell.
(a) In a Proton Exchange Membrane (PEM) fuel cell hydrogen gas is fed to the anode where its electrons are separated with the aid of a catalyst, typically platinum. The electrons supply power to an external circuit while the remaining protons migrate through the PEM and recombine with oxygen and electrons to form water at the cathode, which also typically has a platinum catalyst layer. Adapted from ref. [4].
(b) The "cluster-network" model of hydrated Nafion consists of spherical clusters of the hydrophilic sulfonic acid ions interconnected by narrow channels bearing water in the otherwise hydrophobic perfluorinated membrane. Adapted from ref. [42].

## 3.2 Early Work on Anhydrous Proton Conducting Polymers - First Generation EIS

A series of novel anhydrous polymer proton transport membranes were first synthesized by our collaborators from the Coughlin Group in the Polymer Science department at UMass Amherst. Several publications included conductivity characterization of materials such as benzimidazole functionalized acrylate homopolymers and copolymers with poly(ethylene glycol)methyl ether acrylate (PEGMEA) (e.g., B5A and B5A-PEGMEA 35 in figure 3.3) [62] [63], polysiloxanes with tethered 1,2,3-triazole moiety (e.g., T8Si and T2Si in figure 3.3) [28], random copolymer and terpolymers of 1,2,3-triazole-containing acrylates and PEGMEA [40] (see figure 3.4), and 1,2,3-triazole tethered polyphosphazene [31] (not shown).

Key findings of this work show that the proton conductivity performance of these membranes is sensitive to the length of the functionality's tether to the polymer backbone and to the glass transition temperature of the material. With too short a tether, the functionalities cannot easily contact and exchange protons; with an excessively long tether the density of functionalities is reduced, and they might tend to form more localized clusters. According to the Vogel-Fulcher-Tammann theory [25], well above the *glass transition temperature* polymer chains can move around in their locally accessible free volume; as temperature decreases, the effects of intermolecular forces take over while local viscosity rises continually until the material becomes rigid and glassy. Glassy proton conducting systems which rely on Grotthuss transport tend to have poor conductivity below the transition, because the necessary reorientations of the donor and accepter sites become frozen; however, as we will see in chapter 5 the local reorientations might actually decouple from the bulk viscosity effects and enable anomalously high conductivities well into this transition. The effect of the glass transition on polymers is seen in many plots of $log(\sigma)$ vs. $1/T$ as a non-Arrhenius (not log-linear in $1/T$) concave curve signifying this pseudo-second order phase transition.

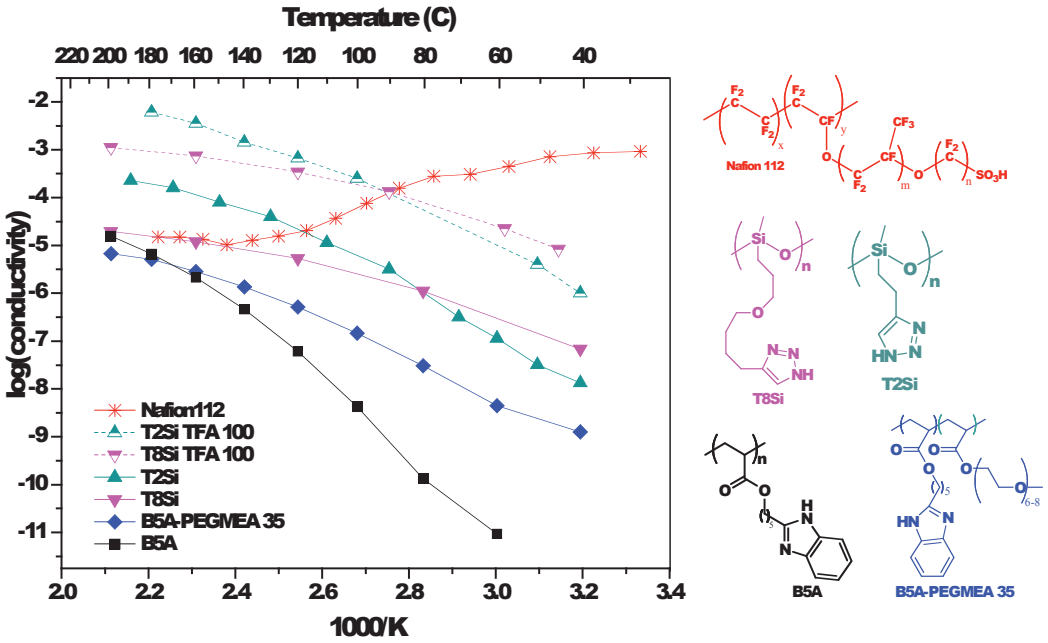


**Figure 3.3.** Anhydrous proton conducting polymers synthesized by Coughlin Group. Proton conducting polymers with benzimidazole (B) and 1,2,3-triazole (T) functionalities synthesized by Rich Woudenberg and Sergio Granados-Focil of Coughlin Group, Dept. of Polymer Science at UMass Amherst. The descriptor "TFA 100" means that the sample was doped with trifluoroacetic acid matching the triazole concentration at 100%. Nafion 112, a standard commercial fuel cell membrane is shown for comparison. The conductivities of these materials were characterized under anhydrous (vacuum) conditions with the first generation impedance spectroscopy system built by Ozgur Yavuzcetin of Tuominen Group, Dept. of Physics. Adapted from ref. [63].

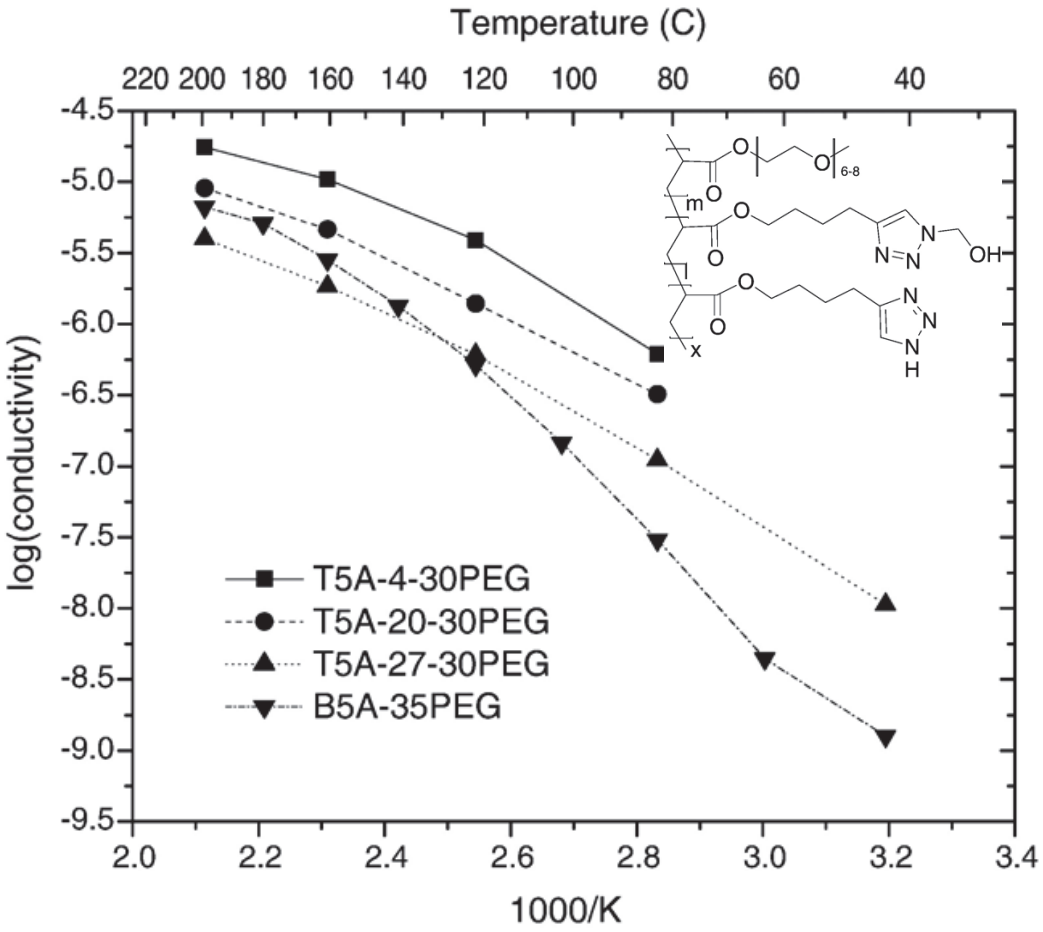


**Figure 3.4.** More anhydrous proton conducting polymers synthesized by Coughlin Group. Random copolymer and terpolymers of 1,2,3-triazole-containing acrylates and poly(ethylene glycol)methyl ether acrylate (PEGMEA), synthesized by Surangkhana Martwiset of Coughlin Group, Dept. of Polymer Science at UMass Amherst. The conductivities of these materials were characterized under anhydrous (vacuum) conditions with the first generation impedance spectroscopy system developed by Ozgur Yavuzcetin of Tuominen Group, Dept. of Physics. Adapted from ref. [63].

## 3.3 Continued Work on Anhydrous Proton Conduction in Polymers - Second Generation EIS

We supported our new collaborators in the "Center for Fueling the Future" from the Thayumanavan Group in the Department of Chemistry by assisting with proton conductivity measurements and the subsequent data analysis. In one study [19], we investigated novel anhydrous proton conducting comb polymers – a molecular design motif involving a polystyrene (PS) backbone with pendant amphiprotic functionalities (benzotriazole [BTz] and imidazole [Im]) with a tether several atoms long (8 or 10) and optionally a pendant decyl alkyl chain (C10). (See figures 3.5(a) and 3.5(b)) The addition of the alkyl chain, though an insulating material, increased the observed conductivity by 2 to 3 orders of magnitude over the analogous polymer lacking the chain. Small Angle X-ray Scattering (SAXS) data (not shown here) was used to determine the likely morphologies of these systems: PS8BTzC10 had lamellar domains; PS10ImC10 had cylindrical domains; and those lacking the decyl chain were amorphous. Though this increase in conductivity is in some sense an "enhancement", more conservatively, it shows the importance of obtaining percolating pathways for proton transport – a necessary but not sufficient condition for high conductivity.

The difference in proton conduction in polymethylmethacrylate (PMMA) functionalized with various pendant amphiprotic heterocycles is investigated in another study [45] with the Thayumanavan Group. (See figure 3.6.) Here pyrazole moieties are confirmed to yield poorly conducting materials, possibly because of alternating hydrogen bond network [6] is disruptive to long-range proton transfer. Both imidazole and 1,2,3-triazole moieties conduct with similar performance; however, triazole may be slightly better due to its ability to form more hydrogen bonding pathways.

---

[6] Perhaps a more realistic visualization of hydrogen bond network comes from the crystal structure of small molecule nitrogen heterocycles. (See figure 4.2.)

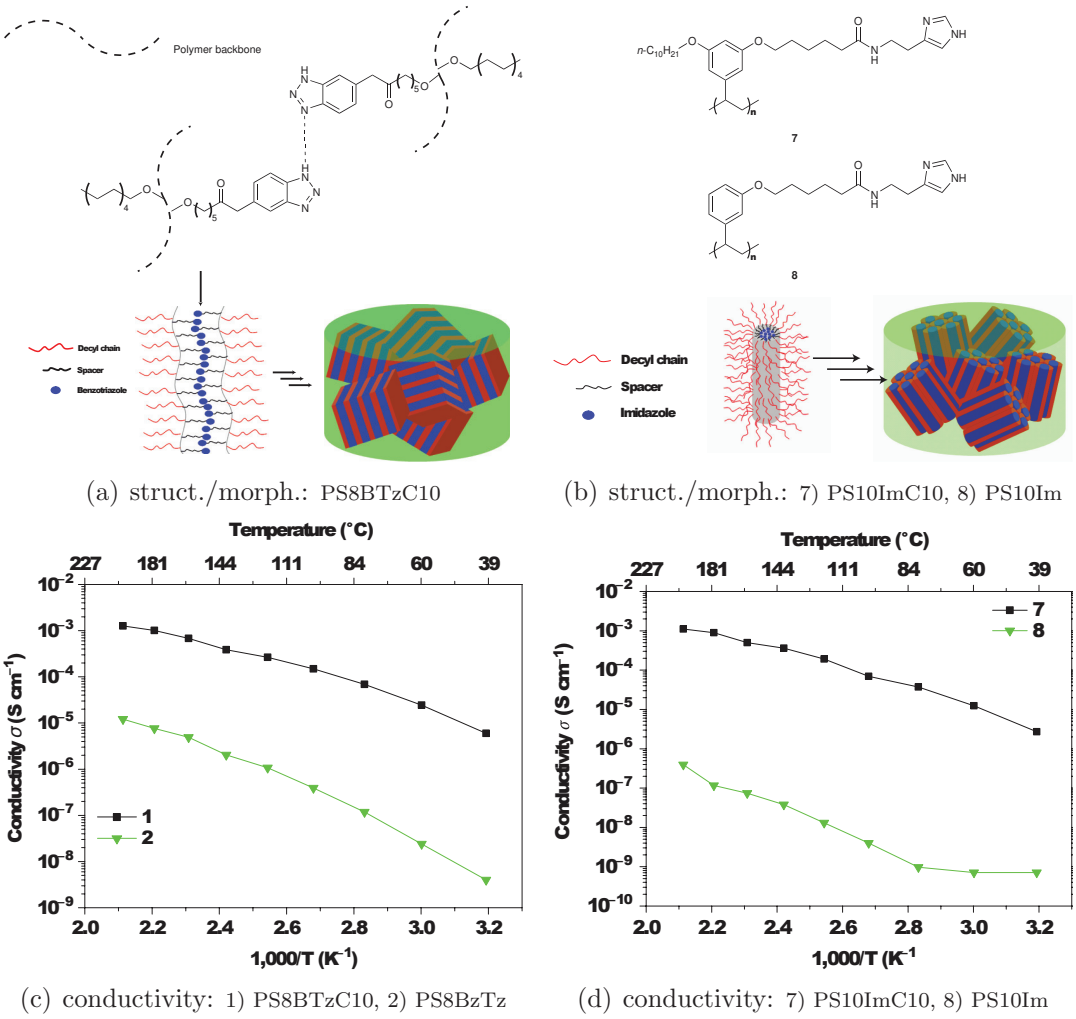


(a) struct./morph.: PS8BTzC10

(b) struct./morph.: 7) PS10ImC10, 8) PS10Im

(c) conductivity: 1) PS8BTzC10, 2) PS8BzTz

(d) conductivity: 7) PS10ImC10, 8) PS10Im

**Figure 3.5.** Anhydrous proton conducting comb polymers: structure, morphology, and conductivity. Yangbin Chen (Thayumanavan Group, Department of Chemistry UMass Amherst) synthesized these anhydrous proton conducting "comb" polymers having pendant amphiprotic functionalities, benzotriazole (BTz) or imidazole (Im) and a pendant decyl alkyl chain (C10). The structures and likely morphologies, determined from SAXS (not shown), are shown in the top two subfigures, while the conductivity is shown compared against a sample lacking the alkyl chain – which are judged to have poorly percolating mesoscale arrangements leading to their much lower conductivities. Adapted from ref. [19].

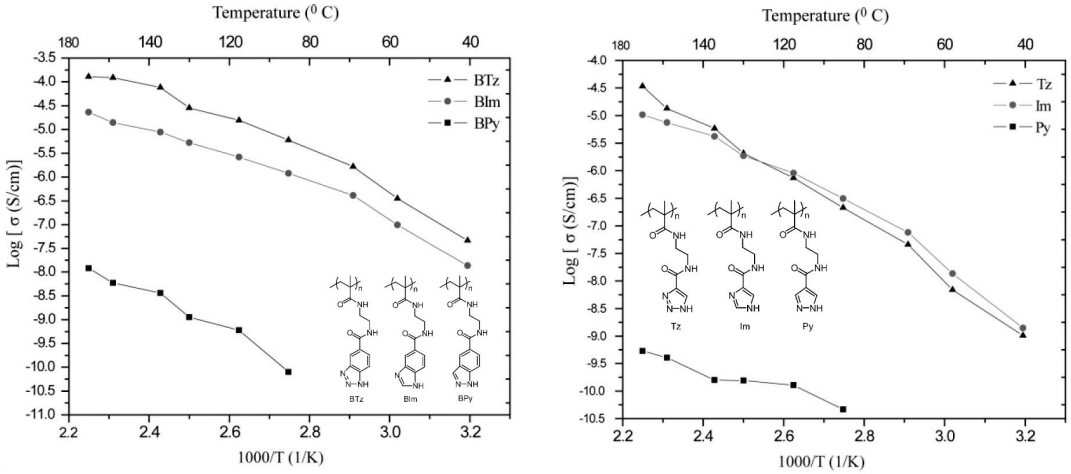


(a) conductivity of PMMA-benz-heterocycles (b) conductivity of PMMA-heterocycles

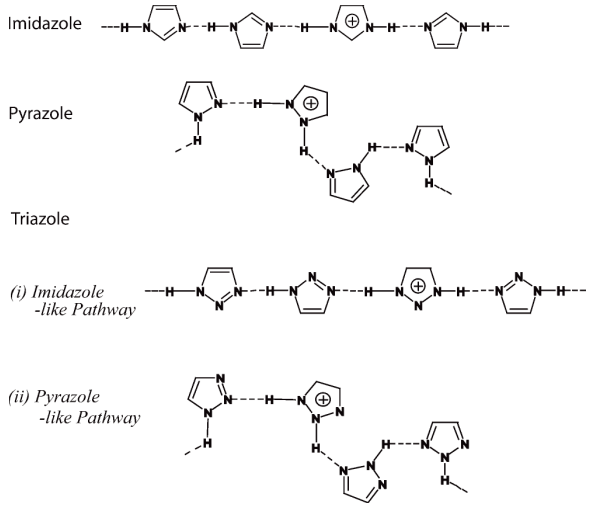


(c) schematic of proton exchange pathways

**Figure 3.6.** Anhydrous proton conducting heterocycle functionalized polymers. Chikkannagari Nagamani (Thayumanavan Group, Department of Chemistry UMass Amherst) synthesized these anhydrous proton conducting materials with a polymethylmethacrylate (PMMA) backbone that has been functionalized with pendant amphiprotic groups: benzotriazole (BTz), benzimidazole (BIm), benzopyrazole (BPy), 1,2,3-triazole (Tz), imidazole (Im), and pyrazole (Py). The benz-heterocycles performed slightly better than the simple heterocycles. The BPy and Py functionalities are shown to lead to poor conductivities, presumably related to their tortuous hydrogen bonding pathways; whereas, BIm and Im have a linear proton exchange pathway, leading to good conduction. The BTz and Tz moieties may bond either like imidazole or pyrazole and may outperform both. Adapted from ref. [45].

## 3.4 Investigations of Proton and Ion Conducting Systems - Third Generation EIS

The increase in productivity brought about by the new high-throughput EIS system allowed for continued and new collaborations. In chapter 4, we present a detailed description of two such collaborative studies led by Dipankar Basak (Venkataraman Group, Department of Chemistry) [8] [9], which looks at anhydrous proton conductivity in materials with mesogenic molecular design motifs. Another brief study [10] by this collaboration investigates squaric acid derivatives as potential proton exchange functionalities. The following subsections contain summaries of interdisciplinary research into anion conducting polymers for alkaline fuel cells (see section 3.4.1), novel 1,2,3-triazolium based ionic liquids (see section 3.4.2), and solid polymer lithium ion electrolytes for battery applications (see section 3.4.3).

### 3.4.1 Anion Conducting Polymers of Alkaline Fuel Cells

In order to pursue new work on novel anion conducting polymers, synthesized by Tsunghan Tsai (Coughlin Group, Department of Polymer Science), we extended the capabilities of the EIS system to include humidity control. New sample holders were fabricated to better resist corrosion in hot, humid conditions. These polymer materials, when bearing hydroxyl or carbonate ions, are being designed to operate in Alkaline Anion Exchange Membrane Fuel Cells (AAEMFCs). (See figure 3.7(c).) Further characterizations were performed by the Herring Group from the Department of Chemical and Biological Engineering at Colorado School of Mines. Two publications on block copolymers with non-conducting polystyrene (PS) structural component and anion transporting polyvinylbenzyl trimethylammonium (PVBTMA) component feature humidity and temperature characterization. [58] [59] (See figure 3.7.)

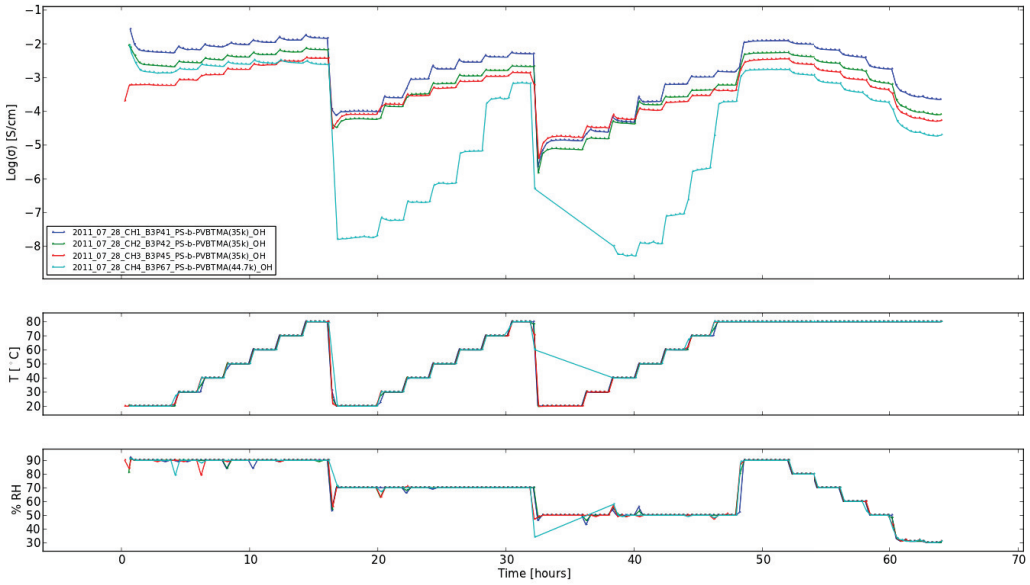


(a) full conductivity at temperature and humidity characterization experiment

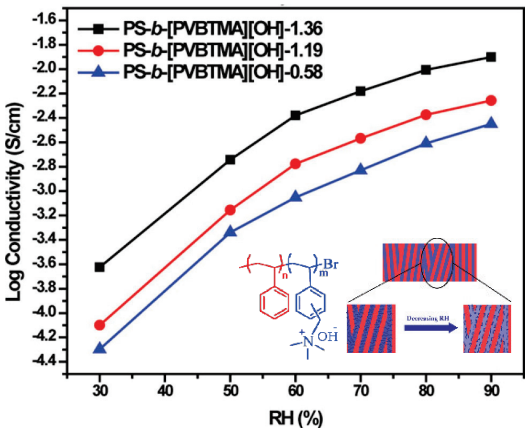


(b) cond. vs. humidity at constant temperature

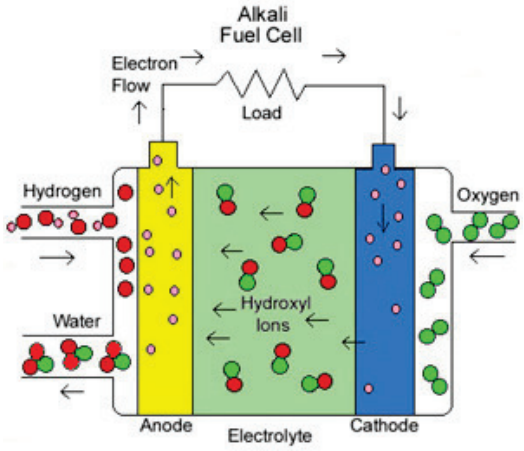


(c) alkaline fuel cell schematic

**Figure 3.7.** Humidity/temperature effects in hydroxide ion conducting polymer PS-b-PVBTMA for Alkaline Anion Exchange Membrane Fuel Cell (AAEMFC).
(a) Conductivity at temperature and humidity control points over time. Unpublished data set.
(b) Conductivity vs. humidity at constant temperature 80 °C. Adapted from ref. [58].
(c) In an AAEMFC, hydrogen is supplied to the anode, where it is catalytically split into protons and electrons, and oxygen is supplied to the cathode similarly to a PEMFC; however the membrane transports oxygen in the form of negative hydroxyl ions from cathode to anode, where it combines with one proton forming waste water while the electrons supply power to an external load. A main advantage is that cheaper nickel catalysts may be used with good efficiency, although long-term chemical stability is still an issue of research. Adapted from ref. [4].

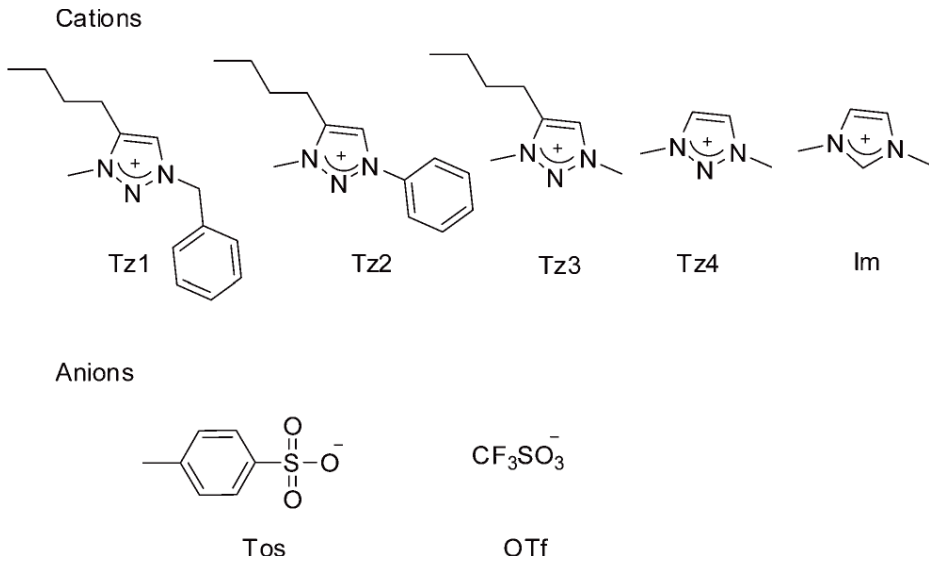


(a) chemical structures for cations and anions

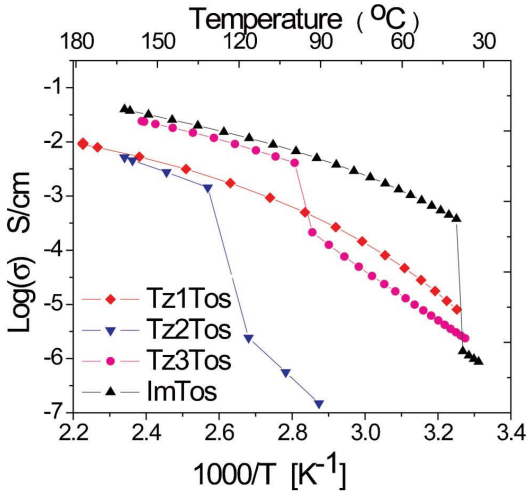


(b) conductivities of tosylate ionic liquids

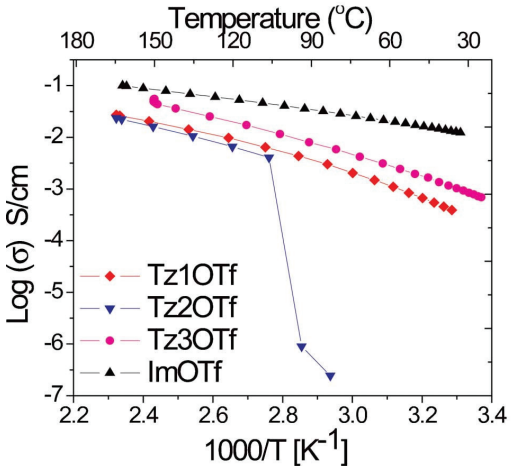


(c) conductivities of triflate ionic liquids

**Figure 3.8.** Conductivity of novel low melting point salts (ionic liquids) based on 1,2,3-triazolium derivative cations paired with tosylate (Tos) or triflate (OTf) anions. 1,3-dimethylimidazolium tosylate and triflate are shown for comparison. All measurements were performed under vacuum conditions; after baking for several hours at the highest temperature in order to remove trace solvent, the data was collected on cooling to ambient temperatures. The steeps drops in conductivity indicate (partial) crystallization. Adapted from ref. [51].

### 3.4.2 Novel Ion Liquids

Another collaborative study with the Coughlin Group measures the conductivity over temperature of novel ionic liquids made from cationic 1,2,3-triazolium derivatives paired with either the tosylate (Tos) or triflate (OTf) anions. (See figure 3.8.) The pairing of sterically hindered asymmetric ions with low cocrystallization energy leads to low melting point salts that form highly conductive viscous liquids in the molten state. Since ionic liquids are excellent solvents for polar compounds and do not give off vapors at moderate temperatures, they have been a subject of increasing interest for battery, chemical synthesis, and many other research communities.

### 3.4.3 Polymer Lithium Ion Electrolytes

A recently quite productive area that we have helped to explore is that of solid polymer electrolytes for lithium batteries. Well publicized lithium battery fires have turned attention to replacing the volatile flammable organic solvents that are common in many products. Because of safety concerns the lithium battery packaging is rather complicated and expensive, including features such as blow-out vents preventing explosions during "thermal runaway" events – which are uncontrolled exothermic reactions between lithium storage electrodes and solvent decomposition products. (See figure 3.9(a).) Furthermore many lithium ion electrolytes are hygroscopic and water will damage the cell by spontaneously decomposing at the high voltage levels ($\sim 3.5\,\mathrm{V}$), so processing must be done under rigorously dry conditions. Polymers that can transport lithium ions, such as polyethylene oxide (PEO), which are considered a safer alternative electrolyte, have been around since the 1970s; but they have suffered from low conductivities at room temperature due to effects like partial crystallization. [64] Transport occurs in these polymer salt complexes as ligand groups are exchanged by local polymer segment movements. (See figure 3.9(b).) An additional benefit of using polymers is the ability to use simpler layered battery architectures (see figure

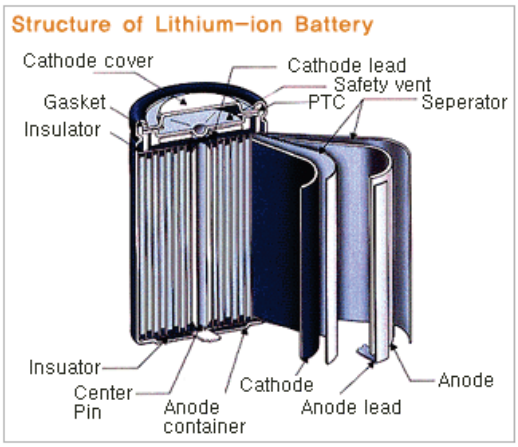


(a) lithium ion battery safety-can

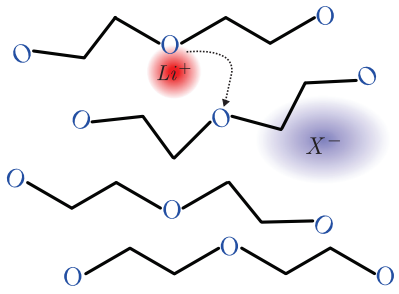


PEO / Lithium Salt Complex

$X = CF_3SO_3$ , TFSI, $PF_6$, $ClO_4$, ...

(b) lithium transport in PEO

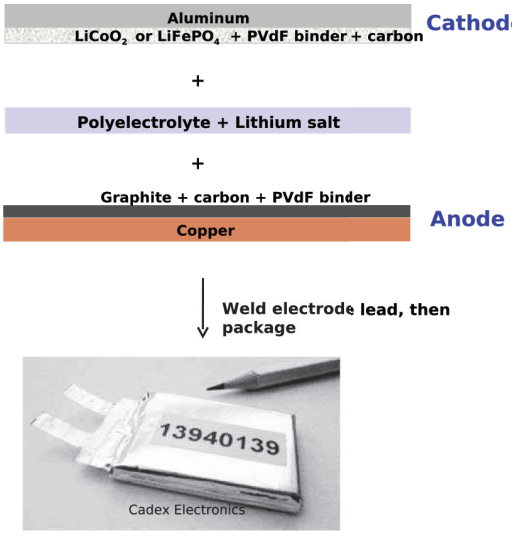


(c) layered polymer Li-ion battery

(d) roll-to-roll coater

**Figure 3.9.** Lithium ion battery fabrication.
(a) Safety concerns with Li-ion batteries requires complicated packaging such as blow-out vents to prevent explosion of the volatile organic solvent in the event of "thermal runaway". Adapted from ref. [21].
(b) Cartoon of lithium ion transport in polyethylene oxide PEO materials. Ions are complexed by ether oxygens and shuttled around as the polymer segments move, rearranging ligand positions.
(c) Construction of layered polymer lithium ion battery. Courtesy of Dr. YuYing Tang.
(d) UMass Center for Hierarchical Manufacturing's (CHM) Roll-to-Roll (R2R) Nano lab's Mini-Labo microgravure coating system. Courtesy of Dr. YuYing Tang.

3.9(c)) that can be fabricated at low cost via large scale roll-to-roll processes (see figure 3.9(d)).

In collaboration with Eric Anderson (Watkins and Gido Groups, Polymer Science), we have performed a high volume of measurements on polyethylene oxide (PEO) containing polymers with different proportions of lithium salts and additives to suppress crystallinity. Here we show a small cross-section of the more than 100 tested compositions. (See figure 3.10(a).) There was an APS abstract/poster [2] for related work on incorporating functionalized solid oxide additives into PEO lithium conducting electrolytes. All conductivity experiments for polymer lithium ion electrolytes were performed under our standard vacuum baking protocol (see section 2.5). Additional collaborative work (not shown) with Dan Miranda (Watkins and Russell Groups, Polymer Science) looks at the effects of chemically cross-linking in PEO copolymer/ionic liquid blends on their conductivity and mechanical properties; [43] the conclusion is that careful design of the cross-linked mesoscale morphology can increase mechanical strength without much of a corresponding decrease in conductivity – a trade off which is often seen in the literature. One last study [61] on lithium ion electrolytes with Catherine Walker (Tew Group, Polymer Science) investigated the conductivity of lithium ions intercalated into novel network polymers containing cross-linked polyethylene glycol (PEG, synonymous with PEO) and polydimethylsilicone (PDMS) segments. (See figures 3.10(b) and 3.10(c).) These solid electrolytes with tunable structure have good conductivities and mechanical properties; the network constraints confer a rubbery toughness and ensure that crystallinity is completely suppressed.

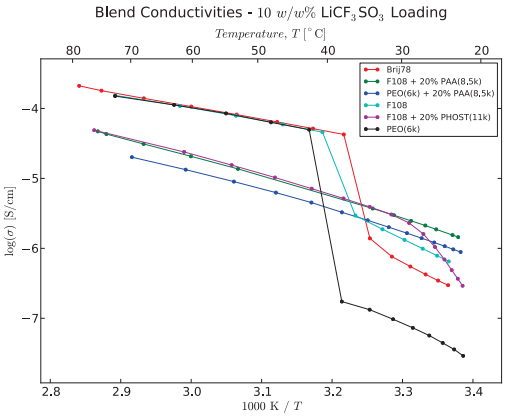


(a) ionic conductivity for PEO block copolymers loaded lithium triflate and homopolymer additives

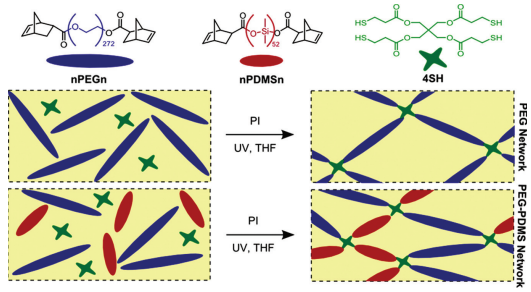


(b)

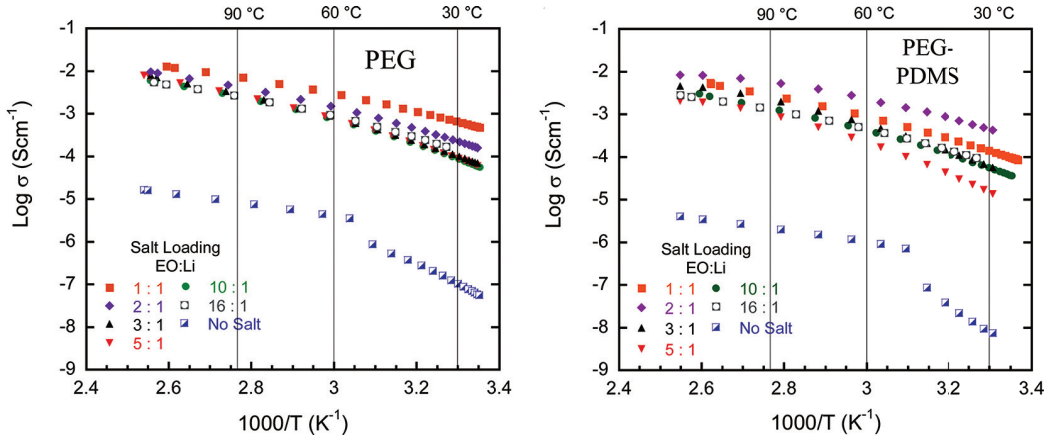


(c)

**Figure 3.10.** Research into solid polymer lithium ion electrolytes for battery applications.
(a) PEO containing block copolymers are blended with interacting homopolymer plasticizers polyacrylic acid (PAA) and polyhydroxystyrene (PHOST) to suppress crystallinity. Room temperature conductivity is somewhat enhanced, but high temperature performance is limited. However, non-crystallizing blends may take gel-like mechanical state at room temperature. Unpublished data.
(b) Scheme for tunable thiol-ene cross-linked polyethylene glycol (PEG) and polydimethylsilicone (PDMS) network polymers. After synthesis lithium triflate is introduced into the polymer with solvent, which is subsequently evaporated. Adapted from ref. [61]. (c) Conductivity for lithium triflate loaded network polymers. Adapted from ref. [61].

# CHAPTER 4

# PROTON CONDUCTIVITY IN AMPHIPROTIC COMPOUNDS

Protons are unique among ionic charge carriers, being essentially naked charges with no electronic screening having the lightest possible chemical mass. They exhibit strong interactions with lone pair electrons on other atoms and can be shuttled along structural reorganizations of extended hydrogen bonding networks within protic solvents – a process known as the *Grotthuss mechanism* [22], which is distinct from the hydrodynamic transport of solvated ions through liquid media. Additionally, *vehicle mechanisms* in which protons diffuse along with carrier molecules may also occur in many systems and can contribute significantly to the overall conductivity. The transfer of a proton from a donor to acceptor atom is characterized by Kreuer [36] as a hopping process from within a double-well potential formed by the asymmetric hydrogen bond. Shielded by the electron density of its host atom, the proton sits in one well, separated by an energy barrier, called the *activation energy*, of height $E_a \sim 1\,\mathrm{eV}$ from another well at the site of an acceptor atom at a distance of a few hundred picometers. (See figure 4.1.) Thermal activation can induce the proton to "hop" the barrier with a probability proportional to the Boltzmann factor $exp(-E_a/k_bT)$. As the interatomic distance decreases, the barrier shrinks, making hopping more probable. Within a solvent environment, ion-dipole interactions can further stabilize charged protonated complexes.

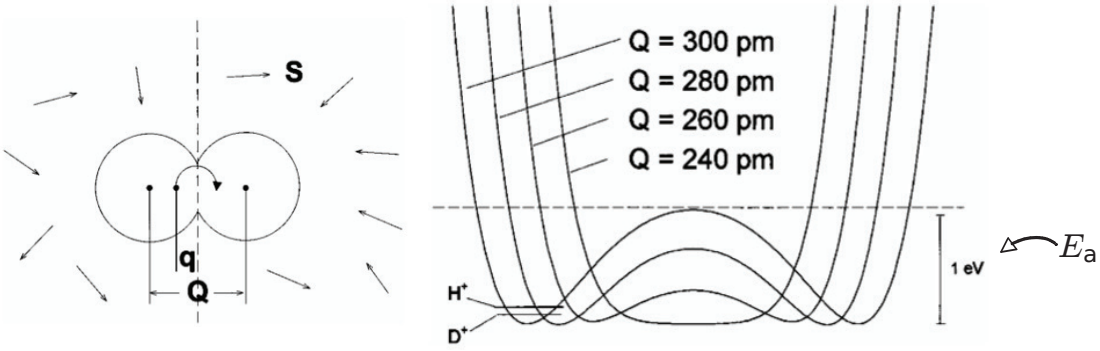


**Figure 4.1.** Schematic of the hydrogen bond potential. The left diagram shows the coordinates of the proton transfer reaction: **q** is the proton position from the center; **Q** is the separation of the donor and acceptor atoms; and **S** represents the set of solvent coordinates. In the plot on the right, the potential energy for proton transfer is shown for various donor/acceptor separations. $E_a \sim 1\,\text{eV}$ is the activation energy of the barrier. The ground state of the proton $^1H^+$ and deuteron $D^+ \equiv {}^2H^+$ are marked on the farthest potential.
Adapted from Kreuer [36].

## 4.1 Aqueous Solutions

Water is a particularly interesting medium for proton transport because of its perfectly *amphiprotic* character (can readily donate or accept excess protons) and its ability to form up to four simultaneous hydrogen bonds, two donating and two accepting. Excess protons in slightly acidified water show anomalously high mobilities ($\sim 3-4\times$), compared to salts in the dilute limit. [36] This anomalous proton diffusion is thought to be mediated through a highly dynamic restructuring of protonated complexes in the solvent through the formation and breaking of hydrogen bonds.[39]

Strong acid in water solutions, with a high density of mobile proton charge carriers, can have conductivities as high as about $1\,\text{S/cm}$. Pure water, on the other hand, has a low conductivity of about $5.5 \times 10^{-8}\,\text{S/cm}$ at room temperature, due to the small concentration dissociated water molecules. Given this assumption, the free charge carrier density of pure water at room temperature can be calculated to be $1.2 \times 10^{14}\,\text{cm}^{-3}$ using equilibrium equation for the *auto-ionization* reaction:

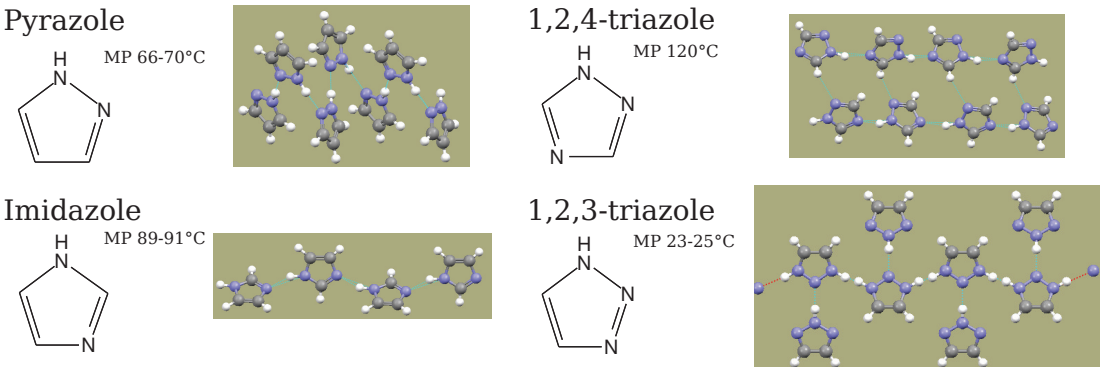


**Figure 4.2.** Structure and properties of select azole compounds, projection of crystal packing structure is shown with nitrogen (blue), carbon (gray), hydrogen (white) and hydrogen bonds (cyan lines).

$$2H_2O \rightleftharpoons H_3O^+ + OH^-, K_{eq} = \frac{[H_3O^+]\,[HO^-]}{[H_2O]^2} \tag{4.1}$$

## 4.2 Small Molecule Azole Compounds

Some aromatic nitrogen containing organic heterocycles, called *azoles*, such as pyrazole, imidazole, 1,2,3-triazole, 1,2,4-triazole and other similar compounds, have dissociable protons and amphiprotic amine nitrogen sites that can form extended hydrogen bonding networks much like water. (See figure 4.2.) These small molecule species (as well as mixtures) show appreciable ionic conductivities, in the range of $10^{-4}$ to $10^{-1} S/cm$ (see figure 4.3), when molten without the addition of dopant acids or other ions; hence, such pure materials are believed to conduct only intrinsically generated protonic charge (and possibly protonic vacancies) via Grotthuss mechanisms. Vehicle transport mechanisms may also be possible in these small molecule liquids. Furthermore, larger molecular scaffolds that have been functionalized with azole moieties, including oligomers [53], mesogens [8] [9], and polymers [54] [66] [52] [45], also show measurable ionic conductivities, but are not expected to support substantial vehicular transport – so this has been taken as an "existence proof" for Grotthuss transport. The higher conductivities of the pure heterocycles over that of pure water suggests higher degrees of auto-ionization, leading to higher free charge carrier

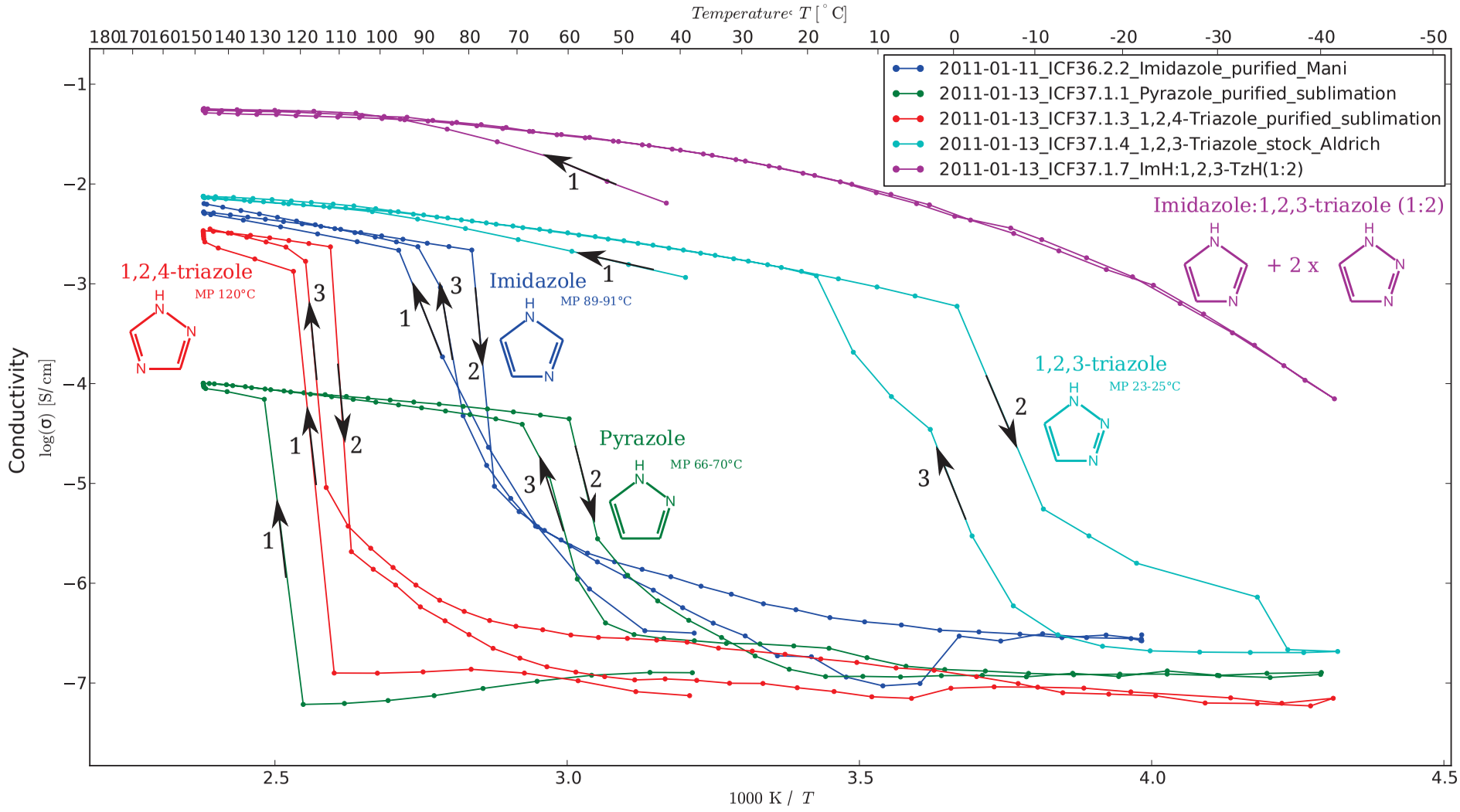


**Figure 4.3.** Arrhenius conductivity plot for azole compounds with initial heating (**1**), cooling (**2**), and reheating (**3**) phases.

densities at equilibrium. Solvent coordination effects and molecular asymmetries in azoles may stabilize proton dissociated complexes more than the highly symmetric pure water solvent environment.

We have shown that certain mixtures of amphiprotic compounds result in materials with enhanced conductivities in the molten state as well lower melting points. For example, binary mixtures of imidazole (Im) and 1,2,3-triazole (Tz) show compositional regions where the conductivity is an order of magnitude greater than either pure compound alone. (See figures 4.4 and 4.5.) An extended temperature range plot of one mixture (Im : Tz) = (1 : 2) in figure 4.3 shows a continuous decrease in conductivity upon cooling down to $-40°$C, indicative of increasing viscosity (glass formation), rather than a discontinuous drop that would be expected around a crystallization transition. It is reasonable that imidazole, which is slightly basic in aqueous solutions, and 1,2,3-triazole, which is slightly acidic, might co-ionize each other more efficiently, leading to higher degrees of charge dissociation and, thus, intrinsic charge generation.

Computational work from our collaborators Jibben Hillen and Jacob Harvey of the Auerbach Group in Chemistry [9] calculates the Gibbs free energies and relative $K_{\text{eq}}$ of the six possible auto- and cross-ionization reactions between imidazole and 1,2,3-triazole, referenced to imidazole autoionization (Reaction 1, see figure 4.6). The simulations were performed under ideal-gas phase conditions (isolated reactants) at standard temperature and pressure, which admittedly are not an entirely realistic model of the condensed liquid phase sample; however, the results are still expected to be qualitatively correct. The interesting conclusion of their study was that protonation of imidazole by 1,2,3-triazole (Reaction 3) is by far the most thermodynamically favored process. Further experiments to determine proton diffusivity using PFG NMR, which are detailed in chapter 5, contradict the alternative hypothesis that the enhanced conductivities might instead be explained by increased charge carrier

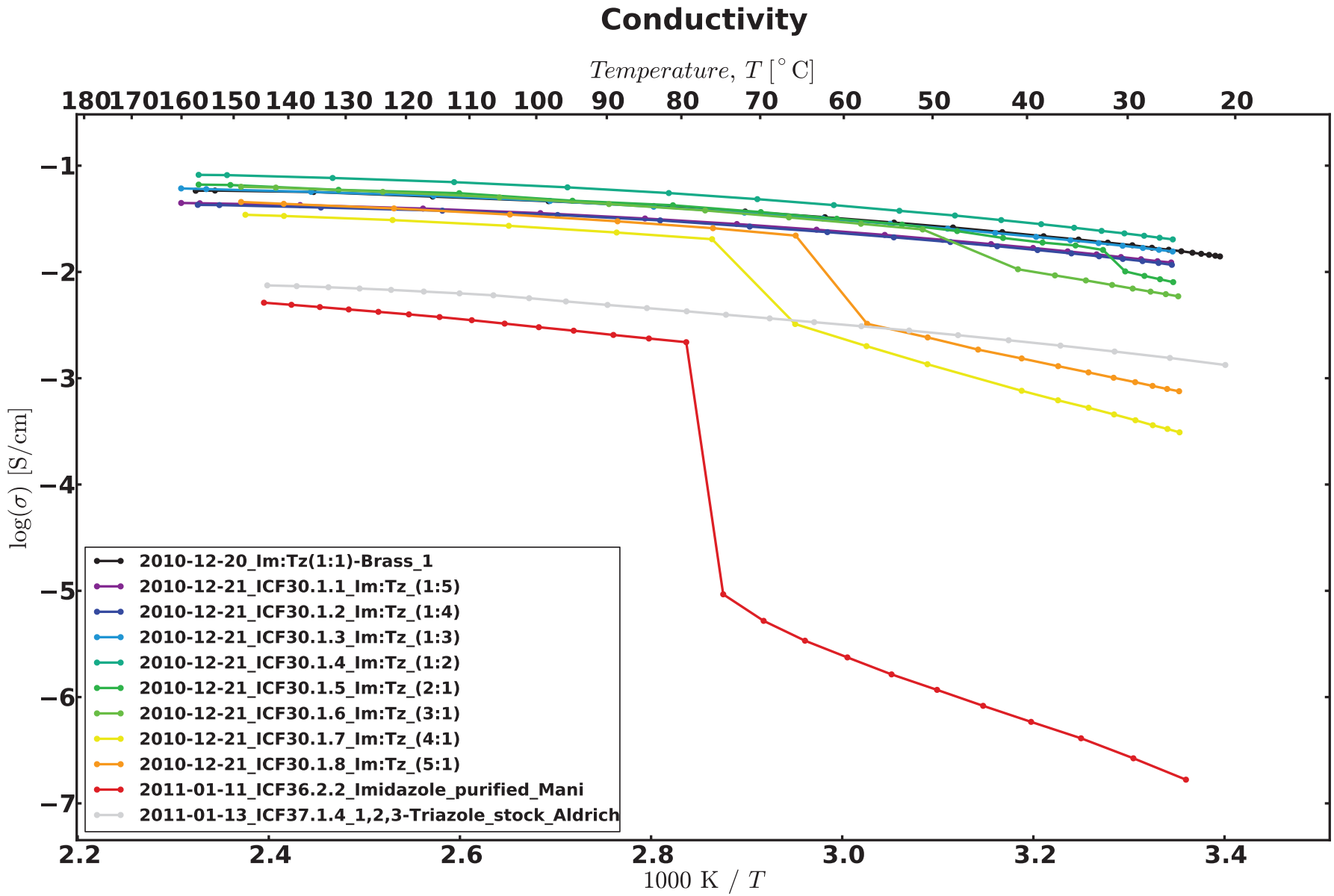


**Figure 4.4.** Arrhenius conductivity plot for imidazole and 1,2,3-triazole mixtures, shown on cooling phase.

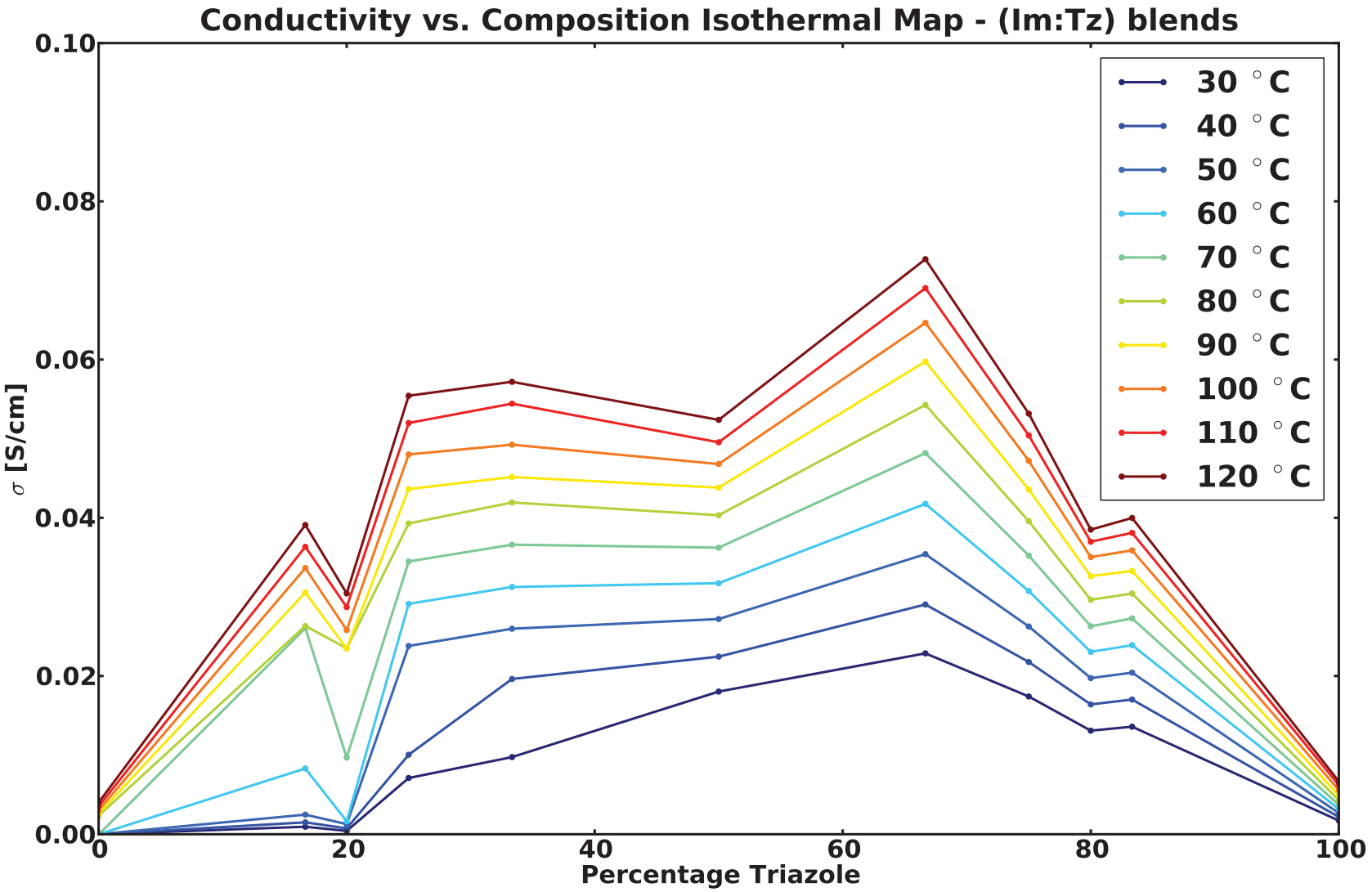


**Figure 4.5.** Conductivity versus composition isothermal plots for imidazole and 1,2,3-triazole mixtures, from interpolation of data shown in figure 4.4.

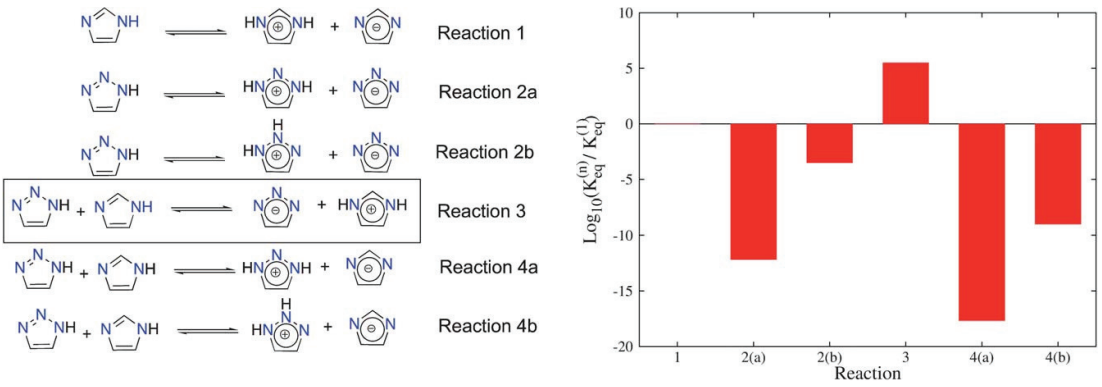


**Figure 4.6.** Relative ideal gas-phase $K_{\mathrm{eq}}$ at STP for auto- and co-ionization reactions between imidazole and 1,2,3-triazole. Adapted from reference [9].

*mobility* through a reduction of viscosity in the blend (rather than increased carrier density). There we show that pure 1,2,3-triazole has the highest proton diffusivity - a quantity which is correlated with mobility (through the Nernst-Einstein relation, eq. 5.3); whereas, in all tested mixtures, a higher proportion of imidazole correlates to lower diffusivities (although they all have higher conductivities than the pure state).

## 4.3 Discotic Mesogens

In previously published collaborative work with the Venkataraman Group in Chemistry and Hayward Group in Polymer Science [8], we investigated novel proton conducting discotic mesogens. The molecular design (see figure 4.7(a)) is based off of a triphenylene (Tp) core functionalized with six triazole (Tz) terminated alkyl-chains having lengths $n = 4, 8, 10$, here abbreviated TpC$n$Tz. Intermolecular $\pi - \pi$ forces which are expected to drive stacking of the aromatic carbon cores and hydrogen bonding between triazole moieties presumably leads to some hexagonal mesomorphic organization of the species (see figure 4.7(b)); additionally, the alkyl spacer chain should confer some flexibility to the triazole end groups, allowing for hydrogen bond reorganization which is critical to the Grotthuss proton transport mechanism. The $n = 10$ variant, TpC10Tz, has been demonstrated to exist in a liquid crystalline

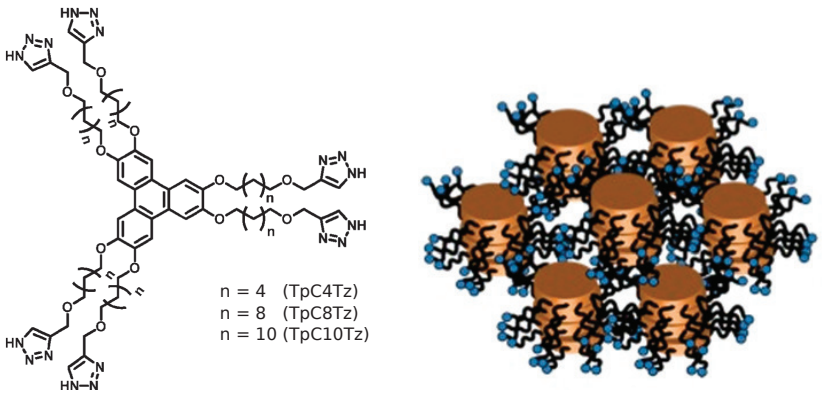


(a) molecular structures

(b) cartoon of mesomorphic organization among multiple mesogens

**Figure 4.7.** Structure of proton conducting discotic mesogens. Adapted from reference [8].

(LC) state above $\sim 70\,^{\circ}\mathrm{C}$ through polarized optical microscopy (not shown), differential scanning calorimetry (DSC) (see figure 4.8(a)), and wide angle X-ray scattering (WAXS) (see figure 4.8(b)). However, the other two variants TpC4Tz and TpC8Tz do not demonstrate a well-ordered LC phase.

Conductivity was characterized over temperatures of $25 - 140\,^{\circ}\mathrm{C}$ at a rate of $1\,^{\circ}\mathrm{C\,min^{-1}}$ (see figure 4.9) using the high-throughput impedance spectroscopy system with ESPEC SH-241 environmental control chamber. The TpC10Tz sample shows an interesting dependence that correlates to the LC phase transition: on heating, the slope of the Arrhenius plot discontinuously switches direction in the region of $68-78\,^{\circ}\mathrm{C}$ and then after proceeds at a lower rate; on cooling, the slope again switches direction in the same region, but then carries past at about the same slope as the LC regime, declining to meet its trend line. We attribute these features to a structural reorganization during melting and a recrystallization that is kinetically frustrated, leading to a supercooled state. Using the Arrhenius relation $\sigma \propto exp(-E_a/k_BT)$, the thermal activation energy barriers for proton conduction were calculated to be $46\,\mathrm{kJ\,mol^{-1}}$ in the crystalline phase and $11\,\mathrm{kJ\,mol^{-1}}$ in the LC phase. The other two samples which do not show LC phase behavior exhibit no discontinuity in ac-

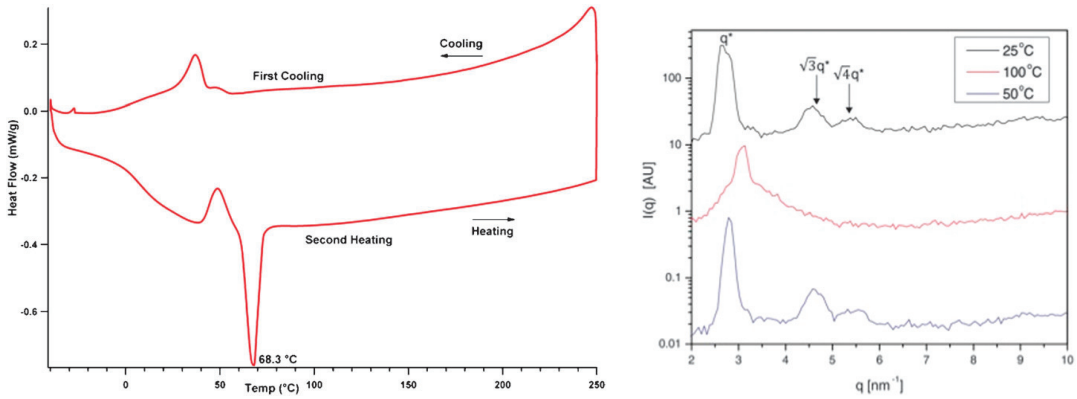


(a) DSC data for TpC10Tz (b) WAXS data for TpC10Tz

**Figure 4.8.** Thermal and X-ray scattering characterization of proton conducting discotic mesogens. The proton conducting mesogen TpC10Tz shows liquid crystal phase transition upon heating over $\sim 70\,^{\circ}\mathrm{C}$. Differential Scanning Calorimetry (DSC) was taken at rates $10\,^{\circ}\mathrm{C\,min^{-1}}$ for heating and $5\,^{\circ}\mathrm{C\,min^{-1}}$ for cooling. Wide Angle X-ray Scattering (WAXS) data shown for crystalline phase at $25\,^{\circ}\mathrm{C}$, liquid crystalline phase a $100\,^{\circ}\mathrm{C}$, and the recovery of crystallinity at $50\,^{\circ}\mathrm{C}$. Adapted from reference [8].

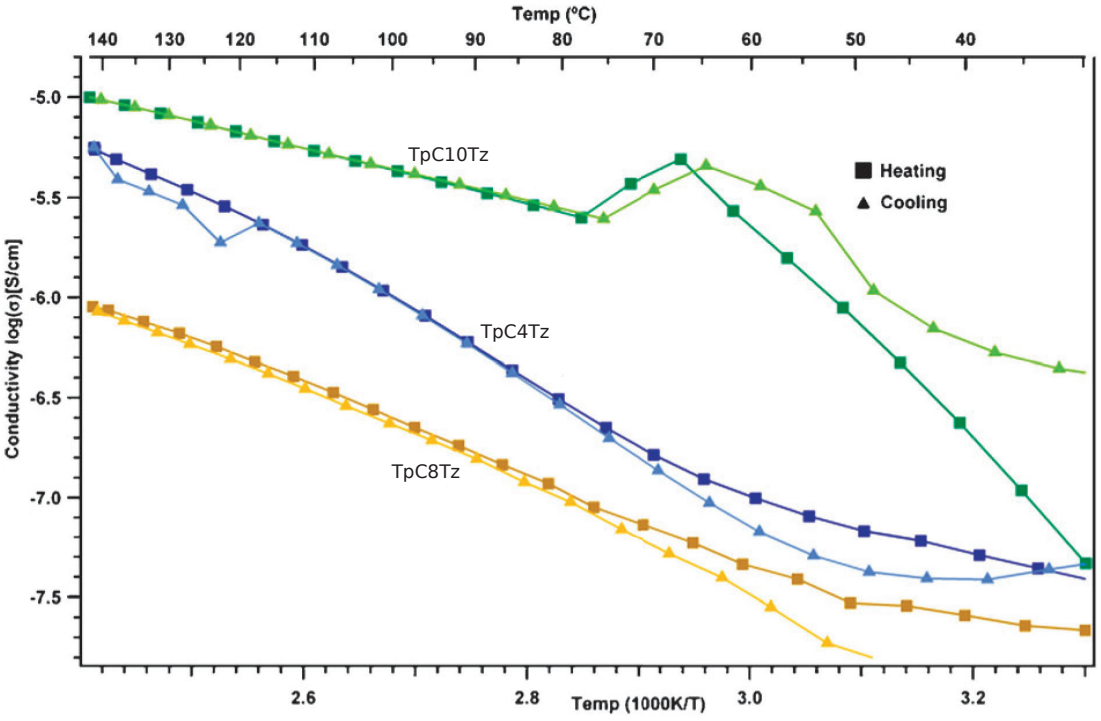


**Figure 4.9.** Arrhenius conductivity plot for proton conducting discotic mesogens. Data was taken with temperature ramp rate $1\,^{\circ}\mathrm{C\,min^{-1}}$. Adapted from reference [8].

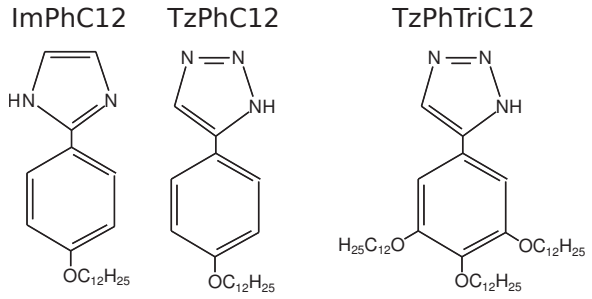


**Figure 4.10.** Structures for proton conducting linear mesogens.

tivation energies. It should be noted that the conductivity of the variant with the shortest alkyl-chain spacer, TpC4Tz, falls between that of the intermediate length spacer, TpC8Tz, at the lowest end, and that of the longest spacer, Tpc10Tz, at the highest. This study demonstrates the importance of considering mesoscale interactions in addition to molecular structure during the design of novel proton conducting materials.

## 4.4 Linear Mesogens

Another, recently published, collaborative study [9] with the Venkataraman Group in Chemistry investigates linear rod-like mesogen compounds functionalized with imidazole and 1,2,3-triazole moieties. Novel chemical structures (see figure 4.10.), abbreviated ImPhC12 and TzPhC12, were designed, having a heterocycle functionality imidazole (Im) or triazole (Tz), respectively, bonded to a phenyl (Ph) core with a twelve carbon alkyl chain (C12) bonded to an oxygen in the *para* position. The variant TzPhTriC12 has three twelve carbon chains in the 3,4,5 positions. Proton conductivity for these pure compounds and for mixtures of ImPhC12 with TzPhC12 was characterized upon cooling from 150 °C at a rate of 0.25 °C min$^{-1}$ (see figures 4.11 and 4.12), and the thermal phase transitions were investigated using differential scanning calorimetry (DSC) (see figures 4.13 and 4.14). The decision to test mixtures

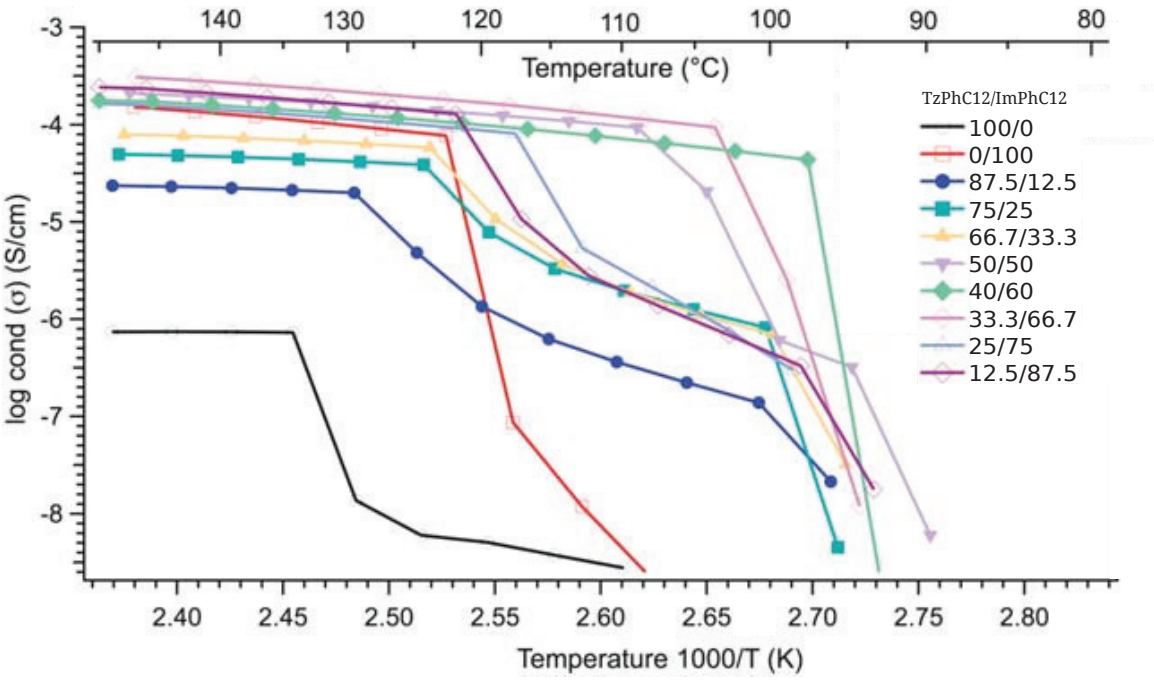


**Figure 4.11.** Conductivity for proton conducting linear mesogen mixtures. Data shown for cooling at $0.25\,^{\circ}\mathrm{C\,min^{-1}}$. Note that labels here show molar ratio as percentage (TzPhC12/ImPhC12). Adapted from reference [9].

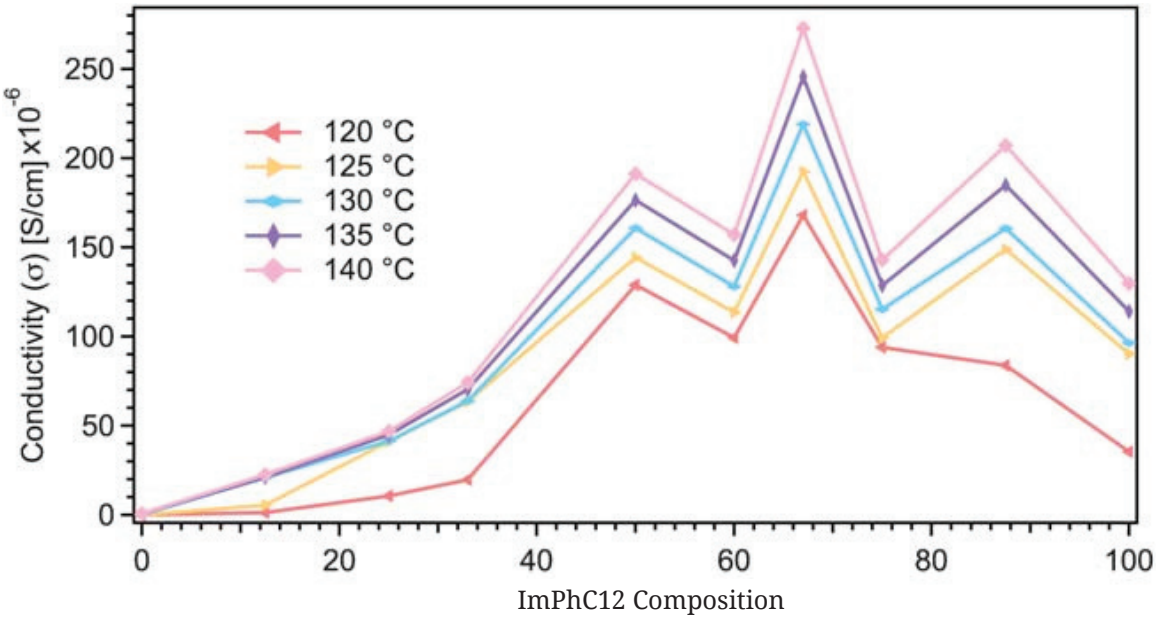


**Figure 4.12.** Conductivity versus composition isothermal plots for proton conducting linear mesogen mixtures, from interpolation of data shown in figure 4.11. Adapted from reference [9].

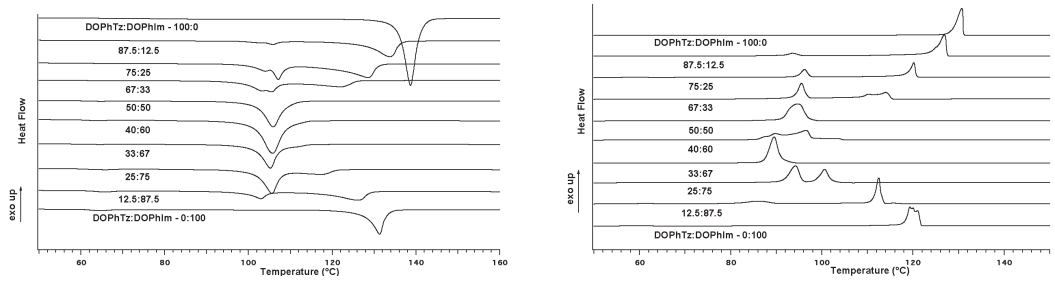


(a) DSC heating (b) DSC cooling

**Figure 4.13.** Differential scanning calorimetry (DSC) for proton conducting linear mesogens. Heating/cooling rate was $10\,^{\circ}\mathrm{C}\,\mathrm{min}^{-1}$.

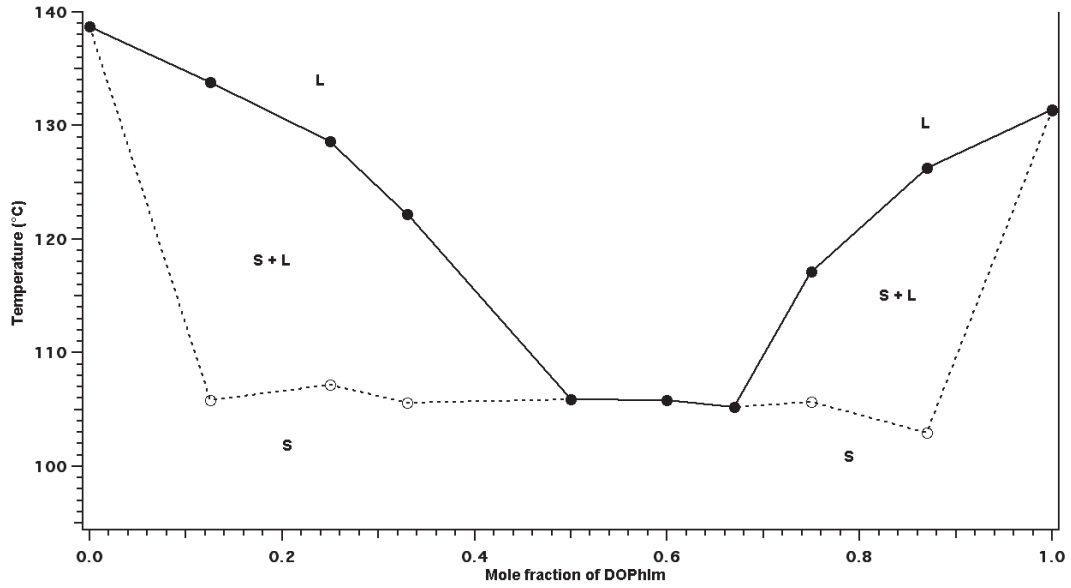


**Figure 4.14.** Thermal and compositional phase diagram for proton conducting linear mesogens mixtures. Data extracted from DSC cooling curves (see figure 4.13(b)), showing up to two exothermic transitions for some mixtures. The solid state is labeled **S**, the liquid state is labeled **L**, and the intermediate state is labeled **S + L**. Note that labels on the x-axis here show molar ratio (ImPhC12:TzPhC12).

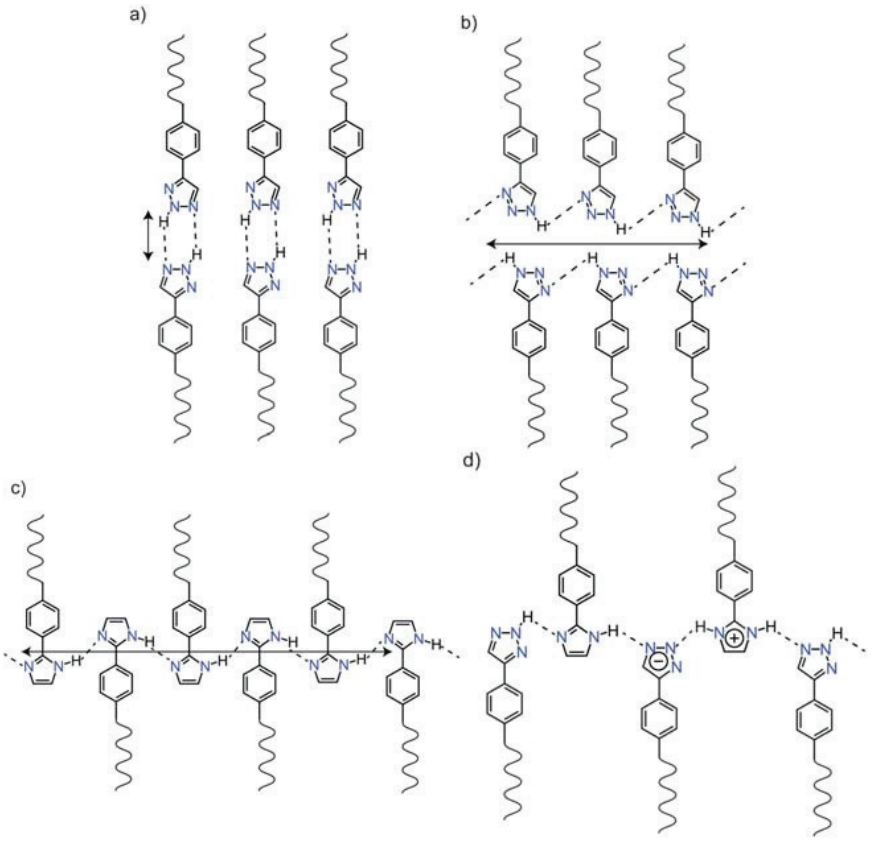


**Figure 4.15.** Hypothetical proton conduction pathways for TzPhC12 *pyrazole-like* (a) and *imidazole-like* (b); ImPhC12 (c); and the 50/50 composition. While extended hydrogen bonding occurs for ImPhC12 and the composite, the TzPhC12 species is expected to form clusters with low percolation, resulting in the low observed conductivity. Adapted from reference [9].

of these compounds was directly motivated by our results for mixtures of imidazole and 1,2,3-triazole (see section 4.2).

TzPhTriC12 showed no measurable conductivity – it was presumed that the mesoscale arrangement of these molecules was driven into a poorly conducting micellular structures with the sterically bulky, non-conducting, hydrocarbon tails outward. Pure ImPhC12 had a conductivity over two orders of magnitude greater than that of pure TzPhC12 in the molten state. The mixtures more rich in the ImPhC12 component seem to cluster around the pure state conductivity, showing only mini-

mal enhancement; however, the mixtures rich in the TzPhC12 component show large variation down to the minimum conductivity of the pure state.

Some of the mixtures show a well-defined intermediate temperature range of non-Arrhenius conductivity decrease (before the sharp drop-off associated with crystallization) that correlates to intermediate liquid-to-solid thermal phases detected in the DSC. In all the mixtures, the lower temperature transitions seem to occur at the same level; whereas, the higher temperature transitions diverge away from the melting points of the pure compounds. Interestingly, there is a central compositional range in which the intermediate phase does not exist. These phenomena suggest that there might be a co-existence of strongly and weakly interacting components which accords with our hypothesis that imidazole and triazole functionalities will preferentially interact through coionization (see figure 4.6) and hydrogen bonding (see case (d) of figure 4.15).

X-ray scattering experiments on these materials (data not shown here, see main text [9]) contributed by our collaborator Scott Christensen (Hayward Group,Polymer Science), along with molecular length simulations from Jacob Harvey (Auerbach Group, Chemistry) provides structural information about the likely packing arrangements of these mesogenic compounds (see figure 4.15). We surmise that the 1,2,3-triazole moiety of the TzPhC12 compound can exhibit two types of hydrogen bonding: localized bonds using two adjacent N atoms, the so-called *pyrazole-like pathway* [45] (see case (a) of figure 4.15) [1]; or extended linear bonds using the two side N atoms, the so called *imidazole-like pathway* [45]. On the other hand, the ImPhC12 is expected to exhibit only imidazole-like hydrogen bonding.

[1]It should be noted that the out-of-plane crystal packing of pyrazole (see figure 4.2) provides an alternative to the in-plane packing depicted in case (a). The approximately 2 order of magnitude lower conductivity of neat TzPhC12 versus ImPhC12 would then be consistent with the relative difference between molten pyrazole and the other heterocycles (see figure 4.3).

The low conductivity of neat TzPhC12 suggests that a predominance of pyrazole-like hydrogen bonding leads to a poorly percolating morphology – a result that initially was unexpected given the relatively high conductivity of liquid 1,2,3-triazole (see figure 4.3). Given the narrow range of existence for the unseparated mixture phase 50% TzPhC12/50% ImPhC12 to 33.3% TzPhC12/66.7% ImPhC12 there is likely a "sweet spot" for imidazole to triazole moiety interaction. Furthermore, note that composition of the conductivity maximum here at 33.3% TzPhC12/66.7% ImPhC12 is opposite to that of the small molecule analogs at 66.7% 1,2,3-triazole/33.3% imidazole and that the enhancement is relatively much weaker – about 1.6× versus 10× (comparing figure 4.12 to figure 4.5), which suggests that this mesoscale molecular ordering might interfere with what might a more optimal arrangement of proton conducting pathways. As we have demonstrated in our last study of proton conducting discotic mesogens (see section 4.3), the intuitional leap from disorganized liquids to more structured systems is highly non-trivial.

# CHAPTER 5

# PROTON DIFFUSIVITY STUDY OF LIQUID HETEROCYCLE SMALL MOLECULE MIXTURES

Nuclear Magnetic Resonance (NMR) spectroscopy is a highly selective yet versatile analytical technique that can yield detailed information about the chemical and physical environment of a target isotope, known as the *observation nucleus*. [1] To further investigate proton conducting mechanisms in specific blends of imidazole (ImH) and 1,2,3-triazole (1,2,3-TzH) we applied diffusion ordered spectroscopy (DOSY) observing the $^1$H nucleus – a style of 2-dimensional Pulsed Field Gradient (PFG) NMR experiment which can measure the self-diffusion coefficient of ensembles of protons, $D(H)$, within the chemical mixture. These measurements are compared amongst themselves along with conductivity data in order to ascertain relative charge carrier densities. Here the notion of the *Haven ratio*, $H = D_{tr}/D_{\sigma}$ the ratio of the tracer diffusivity to *conductivity-derived diffusivity* (see eq. 5.6 or 5.7) will be examined.

## 5.1 Diffusivity and Conductivity in Electrolytes

The random diffusion speed of a charged species within an electrolyte – in the absence of an external electric field – is related to its speed of migration in a uniform field. In section 1.1.2 we described the transport of charge quite generally in terms of the *fluxes* in response to gradients in *electrochemical potential* for each species $i$:

$$\mathbf{j}_i(\mathbf{r},t) = -c_i(\mathbf{r},t)u_i\boldsymbol{\nabla}\eta_i(\mathbf{r},t), \tag{5.1}$$

[1] For more complete information see the freely available HTML primer by Joseph P. Hornak [32]: `http://www.cis.rit.edu/htbooks/nmr/`

where $c_i(\mathbf{r}, t)$ is the local *molar concentration* and $u_i$ is the *mobility*. Net diffusion occurs in reaction to a concentration gradient in the *dilute solution approximation*; [2] we can express the electrochemical gradient (suppressing $\mathbf{r}$, $t$ dependence) as

$$\boldsymbol{\nabla}\eta_i = RT\boldsymbol{\nabla}c_i/c_i + z_iF\boldsymbol{\nabla}\Phi \tag{5.2}$$

where R is the ideal gas constant. The *Nernst-Einstein relation* allows us to express *diffusivity* in terms of *mobility*

$$D_i = RTu_i \tag{5.3}$$

Combining the above relations we arrive at the *Nernst-Planck equation* for mass transfer (in the absence of convection): [3]

$$\mathbf{j}_i(\mathbf{r}, t) = -D_i\boldsymbol{\nabla}c_i(\mathbf{r}, t) - \frac{z_iF}{RT}D_ic_i(\mathbf{r}, t)\boldsymbol{\nabla}\Phi(\mathbf{r}, t) \tag{5.4}$$

which shows that charges can be transported either through *diffusion* in response to a concentration gradient or through *migration* under the influence of an electric potential gradient (electric field). The Nernst-Einstein relation also enables us to express the bulk conductivity (eq. 1.10) in terms of component diffusivities

$$\sigma = \frac{F^2}{RT}\sum_i z_i^2c_iD_i \tag{5.5}$$

In the special case where there is *only one mobile charge species*, we can express diffusivity in terms of the conductivity and molar charge carrier concentration, $c$,

$$D_\sigma = \frac{RT}{z^2F^2}\frac{\sigma}{c} \tag{5.6}$$

---

[2] otherwise the formulation would need to consider more general solution *activities* [47]

[3] see section 1.4.1 of Bard & Faulkner [6]

or in terms of the charge carrier (number) density, $n$,

$$D_\sigma = \frac{k_B T}{e^2}\frac{\sigma}{n} \tag{5.7}$$

so that this quantity may be compared to other derived or measured quantities with the same dimensions – whether such a comparison is even relevant will have be considered for the system under question.

## 5.2 Ion Transport Correlations and the Haven Ratio

In their original study on the transport of sodium ions in sodium silicate glasses, Haven and Verkerk (1965) [30] find that the tracer diffusivity, $D_{tr}$ (measured using a radioactive tracer method), and conductivity deviate from the Nernst-Einstein relation (eq. 5.7) by a small factor of approximately $0.3 - 0.5$. This so-called "correlation factor", later dubbed the *Haven ratio* [4]

$$H_R = \frac{D_{tr}}{D_\sigma} = \frac{e^2 n}{k_B T}\frac{D_{tr}}{\sigma} \tag{5.8}$$

arises in situations for which the mechanisms of ion transport are distinctly different for diffusion and conduction processes. In the tracer diffusion experiment, the sample is doped on one side with an excess of a radioactive isotope of the mobile ion; after a suitable time interval, the concentration profile at some penetration depth is inferred through radiation count rate.

In a more updated picture of alkali glasses [33], the ion migration is thought to occur through the movement of oppositely charged (negative) "vacancies" at interstitial sites, which have a distribution of activation energies such that there are effectively a small number accessible jumps (i.e., low "coordination number") on average at each

[4] the authors originally used the symbol "$f$"

site. A vacancy movement can be viewed as a swap in its position with an ion in a previously occupied site. The limited jump possibilities increase the correlation of any individual ion's movement – it is more likely to jump back to a site that it just left vacant. Hence, the average diffusion length of actual ions is limited by these *backwards correlations* in a given time span, which clearly affects tracer based methods measuring $D_{tr}$. However, bulk conductivity measurements – from which $D_\sigma$ is derived – probe the long-range migration of vacancies which, lacking individuality, are not affected by correlations of this type. Thus, values of $H_R < 1$ are typical for these systems.

The Haven ratio has also been invoked in studies of solid, polymer, and liquid proton conducting materials to compare conductivity to proton self-diffusion coefficients, $D(^1\mathrm{H})$, measured with PFG NMR experiments; however, the interpretation of various ratios between measured and calculated diffusivities and conductivities is markedly different and typically more complicated – especially in multi-component systems – than in the original context (single mobile species, radiotracer diffusion). Therefore, it is critical to be explicit about the assumptions in the calculation and to demarcate different notions of $H_R$ in order to avoid confusion. In the $^1$H PFG NMR diffusion experiment (see section 5.4) an ensemble of proton spins is manipulated so that the attenuation of their stimulated echo response correlates with their diffusion in position referenced by a controlled magnetic field gradient. Depending on the resolution of the technique, "site-specific" diffusivities of the same nuclear species in different chemical bonding arrangements may be distinguished. With sufficient information one may be able to differentiate between mechanisms of diffusion such as vehicle or structure (Grotthuss) processes (see intro. of chapter 4).

In one study, Kreuer et. al. [37] examine proton self-diffusion for varying concentrations of molten imidazole or pyrazole which has been imbibed into a sulfonated polyetherketone membrane. The resolution of their PFG NMR technique can only

differentiate between protons attached to the intercalated heterocycle "solvents" and those affixed to the polymer matrix, but is not site-specific for the labile acid protons which are "transferred from the immobile $-SO_3H$ function to these [mobile solvent] molecules." Since this measurement corresponds to a "vehicle" mechanism of proton transport, we will qualify the diffusivity $D(^1H)^{\text{vehicle}}$ and derived quantities with this label. They calculate an inferred proton diffusivity $D_\sigma$ (eq. 5.6) from impedance-based conductivity measurements; though, it is not clear what value the authors used for charge carrier concentration – presumably it is taken to be equivalent to the sulfonate concentration of the membrane assuming complete acid dissociation. They go on to compute Haven ratios as $H_R^{\text{vehicle}} = D(^1H)^{\text{vehicle}}/D_\sigma$. For the imidazole in polymer samples $H_R^{\text{vehicle}} < 1$ and decreases with increased solvent concentrations – the lowest value in particular is 0.435 for the highest loading and the temperature variation is only slight for all samples. They explain the low Haven ratios as "indicating that intermolecular proton transfer reactions significantly contribute to the observed ionic conductivities" in these cases. However, for the pyrazole intercalated samples, the one with the lowest concentration (the only reported sample with both conductivity and diffusivity data) shows $H_R^{\text{vehicle}} \approx 2$; the authors explain this as "suggesting that the protonated pyrazole starts to be associated with the immobile counter charge [...] in accordance with [pyrazole's] weaker tendency for molecular [self] association by hydrogen bonding." So for these experiments $H_R^{\text{vehicle}} < 1$ is taken to provide indirect evidence of a proton-transfer, or "Grotthuss-type," mechanism; whereas $H_R^{\text{vehicle}} > 1$ is instead explained as the effect of bound ion pair formation. [5]

Another PFG NMR study, Schuster et. al. [55], investigates proton transport in water-free molten phosphonic (phosphorous) acid ($HPO(OH)_2$) and compares it to

[5]It is worthing pointing out that a similar mechanism of neutral ion-pair or complex transport – which contributes to diffusion but not conduction – has been used to explain values of $H_R > 1$ for ionic liquids with two or more mobile species of opposing charge, ref. [23]

phosphoric acid ($PO(OH)_3$). For phosphonic acid, their technique is site-specific for measuring the diffusivities of both the two labile acid protons, $D(\mathrm{H_{OH}})$, and the proton bound directly to the phosphorus atom, $D(\mathrm{H_{PH}})$. (In the case of phosphoric acid, a separate PFG NMR experiment observing $^{31}$P nuclei was performed.) The diffusion of the labile protons is significantly higher $D(\mathrm{H_{OH}})/D(\mathrm{H_{PH}}) \approx 2-3$ which suggests a "high degree of proton exchange". The authors claim that they can approximate "the conductivity contribution of structure diffusion (Grotthuss mechanism) [...] from the difference of the two self-diffusion coefficients"; their formula is reproduced here

$$\sigma_D^{\text{structure}} \approx \frac{F^2}{RT} c(\mathrm{H_{OH}}) \left( D(\mathrm{H_{OH}}) - D(\mathrm{H_{PH}}) \right) \tag{5.9}$$

where "$D(\mathrm{H_{OH}})$ is the average self-diffusion coefficient of all OH protons as obtained by PFG NMR and $c(\mathrm{H_{OH}})$ is the concentration of all OH protons." This diffusion derived conductivity is compared to the measured conductivity to yield Haven ratios $H_R^{\text{structure}} = \sigma_D^{\text{structure}}/\sigma$, which for phosphonic acid has values $2.5-3$, increasing slowly with temperature in the range 90 °C to 150 °C. A similar computation is done for phosphoric acid, yielding $H_R^{\text{structure}} \approx 1.5-1.7$. Their explanation for these greater than unity Haven ratios is postulated to be due to correlations in the dynamic formation and neutralization of charged "defect" pairs through proton exchange; such translocations may occur on transiently formed "closed trajectories" that contribute to net diffusion but not to conduction processes. [6] Furthermore, the authors give a formula to compute the corresponding part of conductivity due to the hydrodynamic transport of charged defects (vehicle mechanism)

$$\sigma_D^{\text{vehicle}} \approx \frac{F^2}{RT} 2\alpha c(\mathrm{H_{PH}}) D(\mathrm{H_{PH}}) \tag{5.10}$$

[6] Again there are similarities to the transport of neutral complexes in ionic liquids with $H_R > 1$ [23]; however, in this case the Grotthuss mechanism leads to diffusivities higher than expected for hydrodynamic transport (vehicle mechanism).

which requires knowledge of the fraction of self-dissociated molecules $\alpha$ and assumes that they have roughly the same diffusivity as the neutral molecule, $D(\mathrm{H_{PH}})$. Assuming that $\alpha \approx 7\%$ as is the case for phosphoric acid, their computed $\sigma_D^{\mathrm{vehicle}}$ is more than an order of magnitude below their measured value; so, they conclude that Grotthuss processes are responsible for about 90% of the observed conductivity in phosphonic acid compared to 98% in phosphoric acid. The comparison to phosphoric acid, which has higher proton conductivity but lower diffusivity thus lower Haven ratios, is believed to be primarily due to its high dielectric constant ($\epsilon \approx 60$), which lowers the electrostatic screening length allowing for increased charge dissociation.

## 5.3 Physical Basis of NMR

According to the nuclear shell model [57], nucleons occupy discrete quantum states consistent with the Pauli exclusion principle - somewhat similar to electron orbitals in atoms; however, the proton and neutron states are distinct and there is strong coupling between spin and orbital angular momenta. Nucleons of the same type seem to cancel spins pairwise, since it is observed that nuclei with even proton and neutron number have total nuclear spins equal to zero and, consequently, zero net magnetic moments. Conversely, nuclei with unpaired proton or neutron spins do have net magnetic moments. In contrast to atoms and molecules with unpaired electron spins, for which there are relatively few of these magnetic species, many elements have isotopes with odd proton or neutron numbers and thus nonzero nuclear spins.

The magnetic moments of nuclei can couple to an external magnetic field, $\vec{B} = B\hat{z}$, leading to a quantum energy level splitting

$$\Delta E = h\nu = h\frac{\gamma B}{2\pi} \tag{5.11}$$

where $h$ is Plank's constant, $\nu = \gamma B/2\pi$ is known as the *Larmor Frequency* and $\gamma$ is the *gyromagnetic ratio*, an empirical constant dependent on the particular nuclear

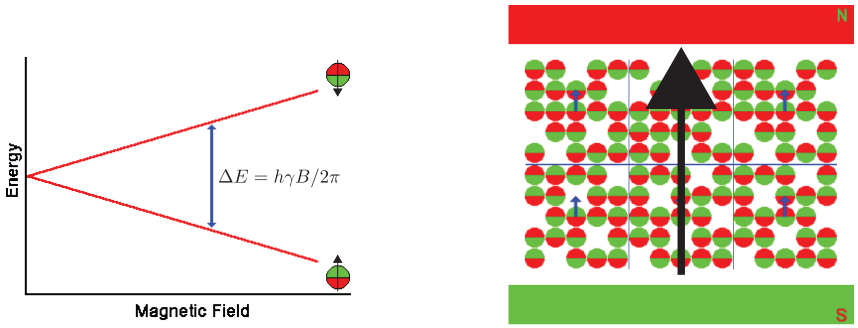


(a) energy level splitting (b) spin ensemble

**Figure 5.1.** Nuclear spins interact with an external magnetic field, splitting energy states with spacing $\Delta E = h\nu = h\gamma B$. The total macroscopic sample magnetization arises from these microscopic spin contributions. Adapted from Hornak [32] `http://www.cis.rit.edu/htbooks/nmr/chap-3/images/et-diag.gif` & `http://www.cis.rit.edu/htbooks/nmr/chap-3/c9-2.htm`

species. Here the ground state, called "spin up" ($\uparrow$) has a parallel alignment to the field direction ($\hat{z}$); whereas, the excited "spin down" ($\downarrow$) state is antiparallel ($-\hat{z}$). The exchange of energy quanta $h\nu$ can induce spins to transition state. At finite temperature, some population of spins exists in the excited spin down state, according to *Boltzmann statistics*:

$$N_\downarrow / N_\uparrow = e^{-\Delta E / k_B T} \tag{5.12}$$

We can treat the ensemble of nuclear spins classically as a magnetization vector $\vec{M}$ formed from many microscopic *spin packets*; at equilibrium

$$\vec{M} = M_0 \hat{z} \tag{5.13}$$

where $M_0 \propto (N_\uparrow - N_\downarrow)$. (See figure 5.1.)

Using electromagnetic radiation pulses at frequencies commensurate with the Larmor frequency, this macroscopic magnetization can be rotated away from the field direction and, thus, induced into a Larmor precession mode. The precessing magnetization then reradiates a portion of the absorbed energy at the Larmor frequency as dissipative spin interactions drive the system back to equilibrium, creating a decaying

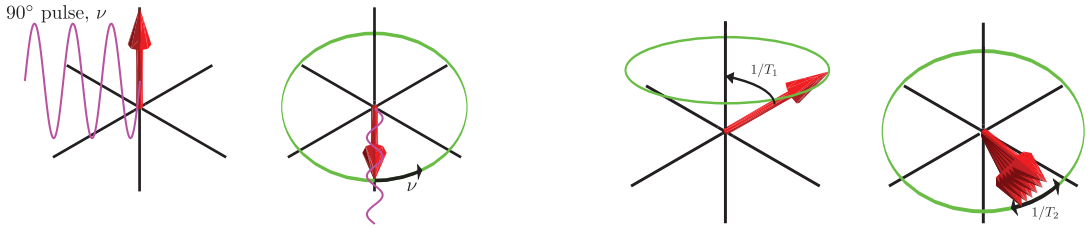


(a) 90° rotation pulse (b) relaxation processes

**Figure 5.2.** The total magnetization vector of an NMR sample can be excited by the resonant absorption of, typically radio-frequency, electromagnetic waves tuned near the Larmor frequency. It will precess at this frequency while the dissipative effects of spin-lattice (characteristic time $T_1$) and spin-spin (characteristic time $T_2$) relaxation drive the system back to equilibrium.

resonant response that can be picked-up by sensitively tuned receivers which are positioned mutually orthogonal to the applied field direction. There are two main types of decay processes that affect the response (chapter 3 of [32]): the *spin lattice relaxation time* $T_1$ describes the return of the field-parallel component of the magnetization to its equilibrium value, and the *spin-spin relaxation time* $T_2$ describes the return of the transverse magnetization to its net zero equilibrium value. The $T_2$ process can be thought of as a loss of phase coherence, or a *dephasing*, of the packet of precessing spins that contribute to the out-of-equilibrium transverse magnetization.

## 5.4 Experimental Background of PFG NMR Spectroscopy

Modern NMR spectrometers typically use superconducting magnets to generate high field strengths on the order of 10 Tesla and can transceive pulses of radio frequency on the order of hundreds of MHz. Observation nuclei within different chemical bonding arrangements have perturbations in their Larmor frequency on the order of several parts per million of the stimulus frequency, known as *chemical shifts*. (chapter 4 of [32]) Various pulse sequences can be issued, and the resulting time-domain response, known as the Free Induction Decay (FID), can be acquired in *quadrature* (i.e., with two detectors along axes mutually orthogonal to the applied field) using


**Figure 5.3.** UMass Amherst's NMR facility Bruker Avance400 Spectrometer with 400 MHz RF source, 9.4 T liquid helium cooled superconducting magnet, variable temperature control unit, and XYZ-gradient probe.

high-speed analog to digital conversion. The quadrature data is typically treated as a complex-valued array for computational convenience, where one detector axis is assigned to the real part and the other to the imaginary part. Typically, the FID is transformed to the frequency domain where the main signal components separate into spectral peaks (or "lines") with, ideally, Lorentzian shape. Given the high resolution of the technique, the spectral lines are sensitive to subtle inhomogeneities in the magnetic field and, in turn, the sample magnetization; so, a number of "shimming" coils are placed in the sample probe in order compensate for unwanted variations. Depending on the experiment, fine-tuning of the shim coil currents for each individual sample (and temperature point) may be critical for proper quantitative analysis.

Clever selection of different pulse timing programs and the imposition of magnetic field gradients can yield further information about the observation nuclei. [34] In the *spin echo* experiment (chapter 6 of [32]), the magnetization is rotated 90° away from the applied field axis, the spin packets will begin to dephase, then sometime later a 180° rotation pulse is applied; a portion of the spin packets will come back into phase

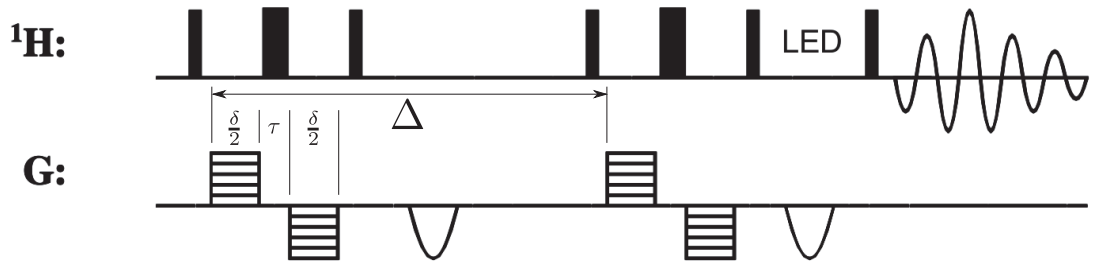


**Figure 5.4.** The "ledbpgp2s" pulse program, adapted from Bruker Topspin manual "DOSY and Diffusion by NMR" p. 31. [35].

coherence, resulting in an *echo* response. Variation in the timing of pulses can be used to measure the $T_2$ spin-spin relaxation time.

A modified version of the spin-echo experiment, known as Pulse Field Gradient (PFG) NMR uses a spatially varying field to "label" nuclear spins in space and time (chapter 11 of [32]): first a 90° rotation pulse is applied, storing the sample magnetization in the transverse direction; then the first gradient pulse ($\hat{z}$ direction) is applied, which rotates the spin packet phases forming a helical magnetization along its axis; some time later a 180° rotation is applied, which starts the rephasing of the packets; then the second gradient pulse is issued to "unwind" the helix before the echo occurs. Nuclear spins that diffuse away from their initial positions between each gradient pulse will fail to rephase and thus the echo response is attenuated. By varying the inter-pulse timing $\Delta$, pulse duration $\delta$, or gradient field strength $g$ over a series of experiments, diffusivities can be measured and matched to chemical shifts – a "2-dimensional" NMR technique known as Diffusion Ordered Spectroscopy (DOSY). DOSY is useful for discerning between components of a mixture that may diffuse at different rates; the Stejskal-Tanner formula gives the attenuation factor for the signal intensity in terms of the diffusivity $D$ and each choice of pulse parameters: [35]

$$A = A_0 e^{-D\gamma^2 g^2 \delta^2 (\Delta - \delta/3 - \tau/2)} \tag{5.14}$$

where $\gamma$ is the gyromagnetic ratio of the observation nucleus and $\tau$ is an inter-pulse delay for bipolar gradient experiments. To simplify analysis, the parameters are typically lumped into the value $Q = \gamma^2 g^2 \delta^2 (\Delta - \delta/3 - \tau/2)$ so that the variation with diffusivity is explicit in this so-called *Q-space* metric:

$$A = A_0 e^{-DQ} \tag{5.15}$$

In a DOSY set where the spectra have multiple well-separated spectral lines, this attenuation can be treated separately by fitting component amplitudes as functions of Q, which can be estimated from peak integrals or other statistical techniques (see section 5.4.2).

Further elaborations on the pulse sequence can be used to cancel out measurement artifacts due to inhomogeneities in the background field and stray eddy-currents induced by the field pulse. The Longitudinal Eddy-current Delay Bipolar Gradient Pulse (LEDBPGP) pulse program [65], which was used herein, is a state-of-the-art DOSY protocol (see figure 5.4). Unfortunately, most PFG NMR protocols are still quite sensitive to adventitious magnetization inhomogeneities which may be modified by changes in the sample's permeability; therefore, careful shim adjustments are needed in each temperature regime. Furthermore, it may also be necessary to adjust the pulse timing parameters in addition to gradient strength in order to obtain suitable ranges in which the response is analyzable.

### 5.4.1 Procedural Details

In this study, samples consisted of either neat 1,2,3-triazole (97% assay, Sigma Aldrich) or a molar mixture of 1:1, 1:2 or 2:1 with imidazole (Sigma Aldrich, purified via sublimation). Before measurement the sample was placed into a standard NMR glass tube and degassed for at least 1 hour under vacuum in a heated sonication bath at $\sim 50\,^{\circ}\mathrm{C}$, then sealed in an argon glovebox using the standard polymer cap wrapped

tightly with Teflon tape. $^1$H PFG NMR DOSY data was acquired at several temperatures in the range from $-10\,^\circ$C to $70\,^\circ$C on a Bruker Avance 400 MHz spectrometer, equipped with an XYZ gradient probe and variable temperature air-flow unit. Since the samples contained no internal reference, the chemical shifts measured are uncalibrated; however, absolute frequency estimation is not required in our analysis. At each temperature change of $5\,^\circ$C (or $10\,^\circ$C), reshimming was performed by manually adjusting the coil currents while attempting to maximize the $^1$H signal intensity and line symmetry; although, it was difficult to tell precisely when the shims were optimized, and it is therefore believed that residual field inhomogeneities are the largest source of systematic error in this experiment. The DOSY experiments were carried out using the manufacturer-supplied "`ledbpgp2s`" pulse program [35] by varying the gradient strength over 32 points in the range from 0.68 to 32.35 G/cm. The combination of the diffusion time $\Delta$ and gradient pulse length $\delta$ were adjusted stepwise as reckoned necessary to keep the signal attenuation in a range with sufficient sensitivity; table 5.1 provides approximate selections for these parameters, though for any given sample the actual range used at a particular temperature might be the previous or the following range. Post-processing of the NMR time-domain signal and computation of the diffusivity results was performed using custom Python programs (details are discussed in the following section 5.4.2).

### 5.4.2 Analysis of NMR Spectra

Traditional NMR analysis proceeds in the frequency domain after discrete Fourier transformation of the complex FID – the two components of data are mixed together to phase correct the resulting spectrum; typically, only the phase-corrected real part of the spectrum, known as the *absorption spectrum* is used for the subsequent analysis. In order to compare NMR frequency domain data between different instruments the spectra are often plotted on a *chemical shift* axis, where the response frequency

**Table 5.1.** Table of PFG NMR timing parameters. $\Delta$ is the inter-pulse "diffusion" time, $\delta$ is the pulse duration, $\tau = 200\,\mu$s is the inter-bipolar pulse time, and $Q = \gamma^2 g^2 \delta^2 (\Delta - \delta/3 - \tau/2)$ evaluated at the field strength minimum $g = 0.0068\,\mathrm{T/m}$ and maximum $g = 0.3235\,\mathrm{T/m}$.

| **Temp. Points** [°C] | $\Delta$ [s] | $\delta$ [$\mu$s] | $Q$ **Range** [s/m$^2$] |
|---|---|---|---|
| $-10$ | 1.600 | 8000 | $3.38 \times 10^8 - 7.66 \times 10^{11}$ |
| $-5$ | 1.600 | 4000 | $8.46 \times 10^7 - 1.92 \times 10^{11}$ |
| $0, 5$ | 1.600 | 2000 | $2.12 \times 10^7 - 4.79 \times 10^{10}$ |
| $10, 15$ | 0.800 | 2000 | $1.06 \times 10^7 - 2.39 \times 10^{10}$ |
| 20 | 0.400 | 2000 | $5.28 \times 10^6 - 1.20 \times 10^{10}$ |
| $25, 30, 35$ | 0.200 | 2000 | $2.64 \times 10^6 - 5.97 \times 10^9$ |
| $40, 45$ | 0.100 | 2000 | $1.31 \times 10^6 - 2.97 \times 10^9$ |
| $50, 55, 60$ | 0.050 | 2000 | $6.52 \times 10^5 - 1.48 \times 10^9$ |
| $65, 70$ | 0.025 | 2000 | $3.21 \times 10^5 - 7.26 \times 10^8$ |

is scaled in parts per million (ppm) of the base spectrometer frequency. Peaks in the frequency domain, which may be split into multiplets (from spin-spin coupling), correspond to the Larmor resonance response of the observation nuclei in different chemical bonding arrangements. Integrals under these peaks give an estimate of the proportions of nuclei at each chemical shift, and thus give detailed information about the chemical structure of analyte compounds.

A preliminary analysis of the $^1$H NMR absorption spectra for two samples, neat 1,2,3-triazole (abbreviated TzH, see figure 5.5) and a mixture of imidazole and 1,2,3-triazole in equimolar proportions (abbreviated ImH+TzH(1:1), see figure 5.6) is shown here for example; the field shimmings were not painstakingly tuned for this experiment, leading to asymmetric peaks with poor, but sufficient resolution. TzH shows two peaks: the (s)inglet at lower chemical shift ($\sim 7.0$ ppm) is assigned to the 2 carbon bound (CH) protons at the 4,5 positions of the ring, hence the label (s, 2H, 4,5-CH); the other singlet peak at high chemical shift ($\sim 14.8$ ppm) is assigned to the labile proton (NH) which is either associated with the nitrogen at ring position 1 (equiv. 3) for the $1H$ tautomer or at the 2 position (with double bond rearrangement in the ring) for the $2H$ tautomer, hence the label (s, 1H, NH); the integral of the

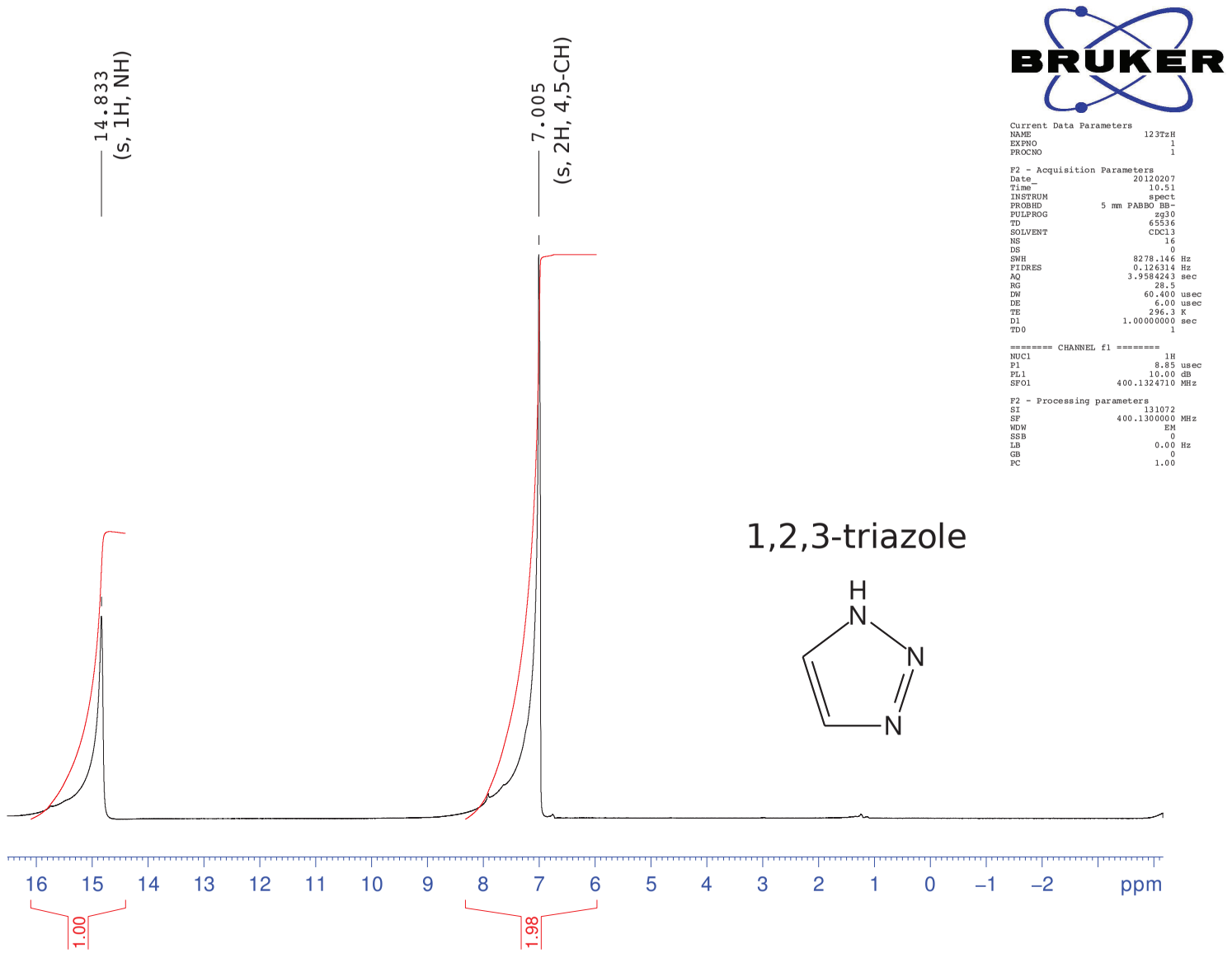


**Figure 5.5.** $^{1}$H NMR absorption spectrum for 1,2,3-triazole at room temperature, no solvent.

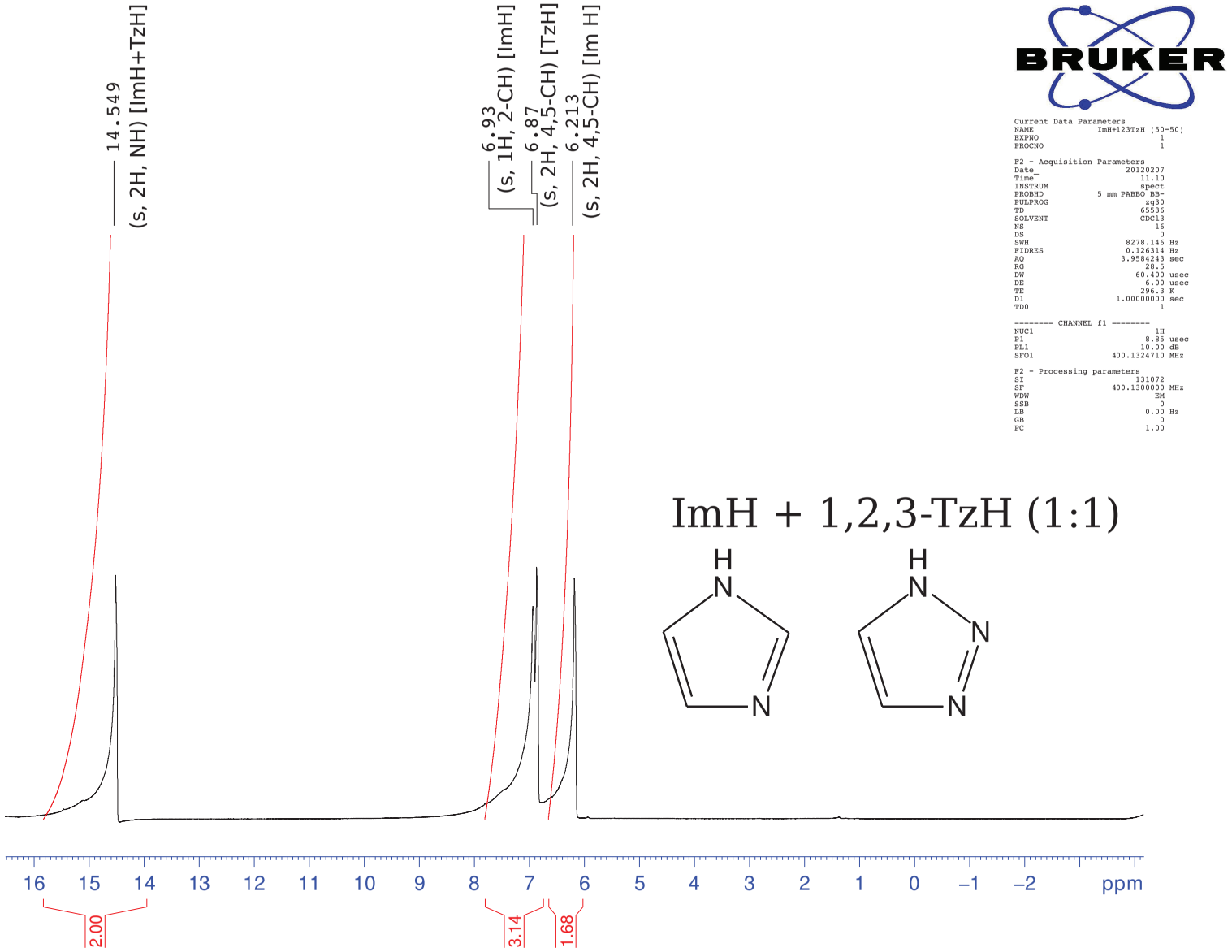


**Figure 5.6.** $^{1}$H NMR absorption spectrum for imidazole + 1,2,3-triazole (1:1) mixture at room temperature, no solvent.

CH peak is roughly twice that of the NH peak, which is expected on the basis of relative concentration. In the case of the mixture ImH+TzH(1:1) the spectrum is slightly more complicated: again the high chemical shift peak ($\sim$ 14.5 ppm) is assigned to NH labile bonds, but this proton could have come from either the ImH or from TzH – they cannot be distinguished at this resolution, hence the label (s, 2H, NH)[ImH+TzH]; the next highest shift singlet at 6.93 ppm rests on the left shoulder of another but is sufficiently distinct, it the has been assigned to the 2 position on imidazole with the label (s, 1H, 2-CH)[ImH]; the following peak at 6.87 ppm is assigned the label (s, 2H, 4,5-CH) [TzH]; and lastly the peak at 6.2 ppm is assigned as (s, 2H, 4,5-CH) [ImH]; this ordering of spectral lines remains the same for all tested mixtures Im+TzH (1:1), (1:2) and (2:1) with peak integrals roughly proportional to the expected concentrations.

G. Larry Bretthorst has applied Bayesian statistics to the analysis of NMR data. [14] [15] [16] [17] [18] By applying Bayes' theorem to a broad class of model functions for time domain signals, he derives a general procedure for parameter estimation which can accommodate prior information about the signal and marginalize out nuisance parameters. (See appendix A for formulas.) He argues that the Fourier *power spectrum* (i.e., the squared magnitude, *not* the absorption spectrum) is the optimal estimator for the frequencies of an FID composed of multiple sinusoidal responses; in this case the power spectrum is the logarithm of the marginal likelihood for the frequency parameters. The analysis of a model involving a single exponentially decaying sinusoid, yields a "proper statistic" that is the Fourier power spectrum of the FID when it is first multiplied by an appropriate exponential function, which sheds light on the traditional data processing step of *apodization* (i.e., "windowing" the data before transformation to the frequency domain). Finally, he applies these techniques to derive estimators for amplitudes of well-separated sinusoidal signals.

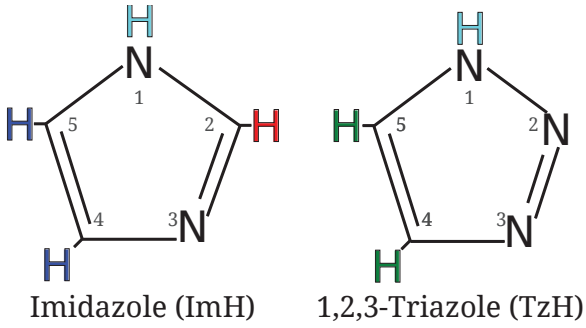


**Figure 5.7.** Color convention for $^1$H NMR peak assignment.

In this study all $^1$H NMR spectra which were components of a DOSY run were batch processed using custom Python programs with techniques derived from Bretthorst's Bayesian analysis papers. The analysis requires the estimation of an amplitude $A$ for each frequency component (spectral peak) as the $Q$-space parameter is varied (see eq. 5.15) over a set of spectra, for which we use a modification of the Bayesian technique described in appendix A: this amounts to first estimating the decay constant $\alpha_{\text{est}}$ of the signal component; then apodizing the signal with the function $\exp(-\alpha_{\text{est}}t)$; then computing the apodized Fourier power spectrum $|F(\omega, \alpha = \alpha_{\text{est}})|^2$ and evaluating its peak value at $\omega = \hat{\omega}$ which gets plugged into the amplitude estimation formula eq. A.21 along with the estimated decay constant. This method's advantage over a traditional absorption spectrum peak integral estimate is that it provides an error estimate and also avoids the need for complicated phase correction or integration range parameters.

In ideal situations, one could have computed the apodized Fourier power spectrum by treating $\alpha$ as a nuisance parameter and marginalizing it out by averaging over a suitable range, which works because $|F(\omega, \alpha)|^2$ would be sharply peaked around the true decay parameter $\hat{\alpha}$. However, this marginalization procedure was problematic for our data, likely due to distortions in the attenuated echo response aggravated by imperfect shimming. Instead, we directly computed $\alpha_{\text{est}}$ for each spectral peak according to the following procedure: first, the unapodized Fourier spectrum was

partitioned into frequency channels around each peak; then, by channel, the inverse Fourier transform was taken to recover the isolated time domain signal of one frequency component; finally, the decay constant was estimated by fitting a line to the logarithm of the envelope of the channel time domain signal – a restricted time interval was selected in order to avoid artifacts of the echo response. (For example, see top plot in figure 5.8.) Instead of using a separate set $\{\alpha_{\text{est}}\}$ for each spectrum in the DOSY series, we applied the values from the first set (lowest $Q$, least attenuation) to all subsequent processing steps; this choice tended to make the analysis more robust since the data acquired under the highest attenuation typically had the most distorted envelope. Additionally, the $\{\alpha_{\text{est}}\}$ *should* be independent of the $Q$ parameter in ideal situations; however, when the actual variation is significant this may create a biased estimate, especially in the high $Q$ limit.

For example, we show the amplitude estimation process for the sample ImH+TzH(1:1) at 25 °C in figure 5.8. The computation of the set of amplitude estimates indexed by peak number $\{A[n] \,|\, n = 0..3\}$ for each $Q$ can be represented by scaling the apodized Fourier spectrum magnitude according to eq. A.21, where the values are those of the peaks and the range of each peak (by color) shows the channel partitioning. (See second plot. Note that the "frequency shift" axis is backwards and offset from the chemical shift scale.) The absolute amplitude $A[n]$ and the relative amplitude $2A[n]/A[0]$ by peak index are plotted against $Q$ in the third and fourth plots, respectively. In order to estimate the set of diffusivities $\{D[n]\}$ for each peak, first $A[n]$ is normalized by fitting it to a function of the form $A[n] = A_0[n] \exp(-D[n]Q)$ (eq. 5.15) and then dividing through so $A[n] \leftarrow A[n]/A_0[n]$; then the normalized amplitudes are refit to an equation $A[n] = \exp(-D[n]Q)$ with one less degree of freedom $k = |A[n]| - 2$ (i.e., two less than the number of points fit).

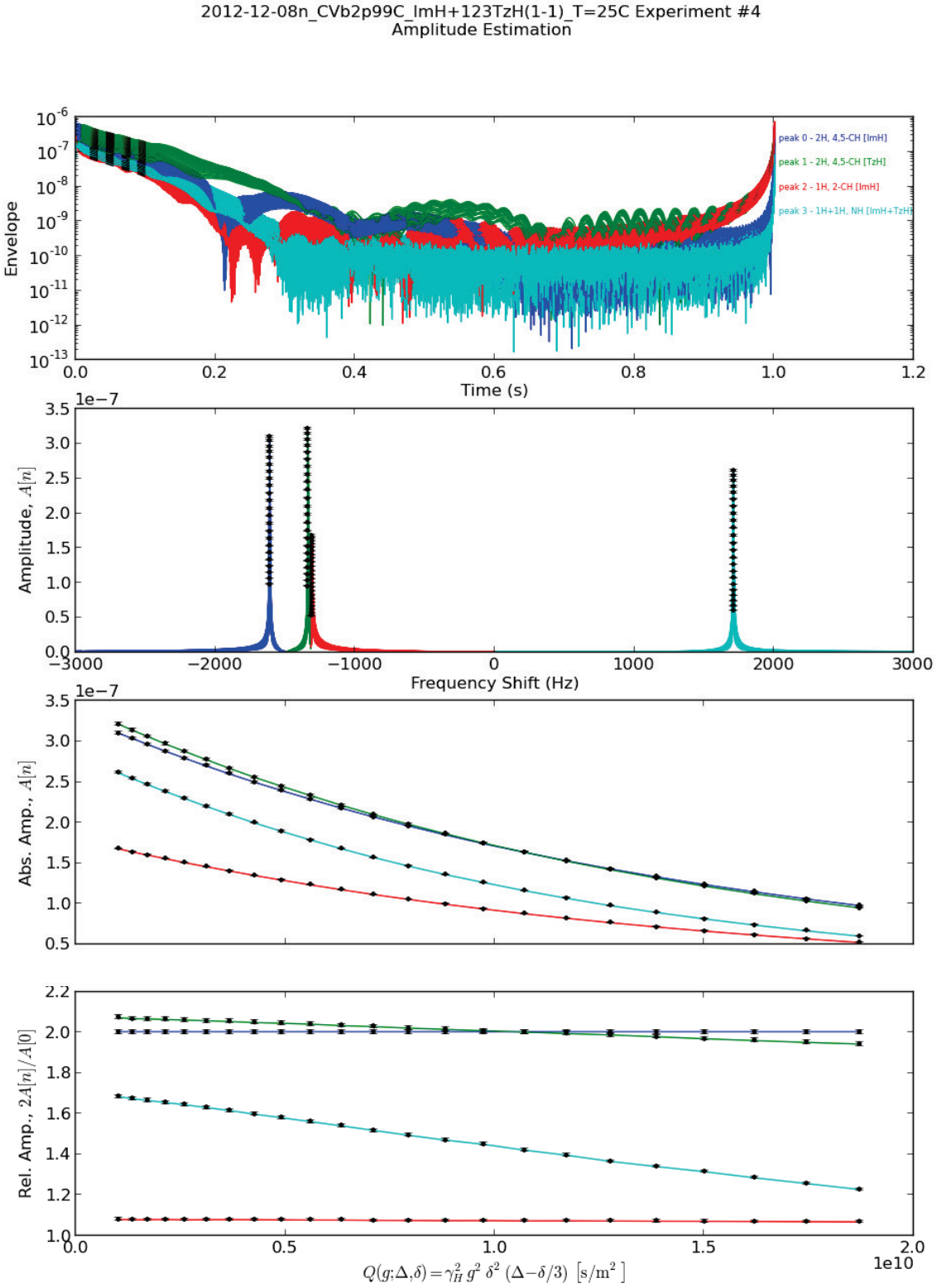


**Figure 5.8.** Example DOSY amplitude estimation.

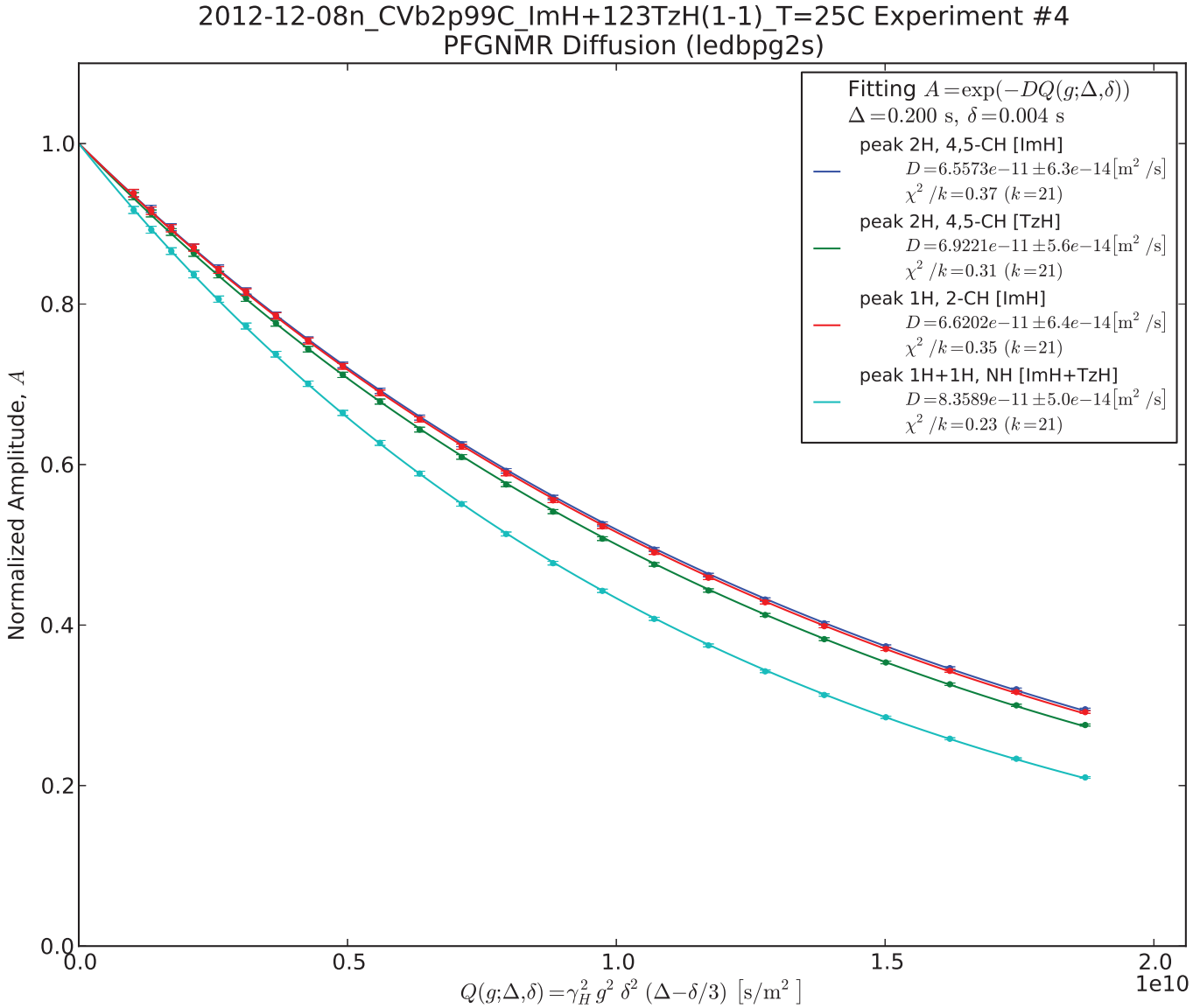


**Figure 5.9.** Example DOSY Q-space fit. Diffusivities $D$ are estimated from an exponential fit for each spectral component.

## 5.5 Experimental Results

PFG NMR studies were performed to acquire proton diffusivity data as a function of temperature in the (largest) range of $-10\,^{\circ}\mathrm{C}$ to $70\,^{\circ}\mathrm{C}$ for four samples: neat 1,2,3-triazole (TzH) and three mixtures with imidazole (ImH) having molar proportions, ImH+TzH(1:1), ImH+TzH(1:2), and ImH+TzH(2:1). The data is shown for each sample separately on Arrhenius plots of $log_{10}$ of the diffusivities [$\mathrm{cm}^2/\mathrm{s}$] versus $1000K\,/T$; the colored interpolating lines are shown only to guide the eye, no fits were performed over the full range of data. (See figures 5.10, 5.11, 5.12, and 5.13.) For the sample TzH there are only two spectral lines: the carbon-bound 2 protons (2H, 4,5-CH) in *green*; and the labile proton (1H, NH) in *cyan*. The mixture samples ImH+TzH(x:y) have four spectral lines: the imidazole-bound protons at ring positions 4,5 (2xH, 4,5-CH [ImH]) in *blue*; the triazole-bound protons at ring positions 4,5 (2yH, 4,5-CH [TzH]) in *green*; the imidazole-bound protons at ring positions 2 (xH, 2-CH [ImH]) in *red*; and the labile protons from each heterocycle (xH+yH, NH [ImH+TzH]) in *cyan*. (See figure 5.7 for color convention.) Note that some of the trends show jagged transitions between certain data points – this systematic error is likely due to problems in obtaining the optimal magnetization shimming with changes with temperature. Another problem might be that the (2-CH [ImH], *red*) and (4,5-CH [TzH], *green*) spectral lines are so close in frequency that their attenuations (and thus measured diffusivities) are correlated by spin interactions. At this point one should not read too much into the point-to-point variation of the data until a better collection procedure is devised.

In light of the aforementioned problems, we shall restrict each data set into the largest region where it varies smoothly in the hopes that further analysis can reveal meaningful trends here without too much distraction. (See figure 5.14.) We have plotted 5 points each of the labile proton diffusivities, here labeled $D(\mathrm{H_{NH}})$, and that of the other molecule-bound protons, here computed as the average of the (4,5-

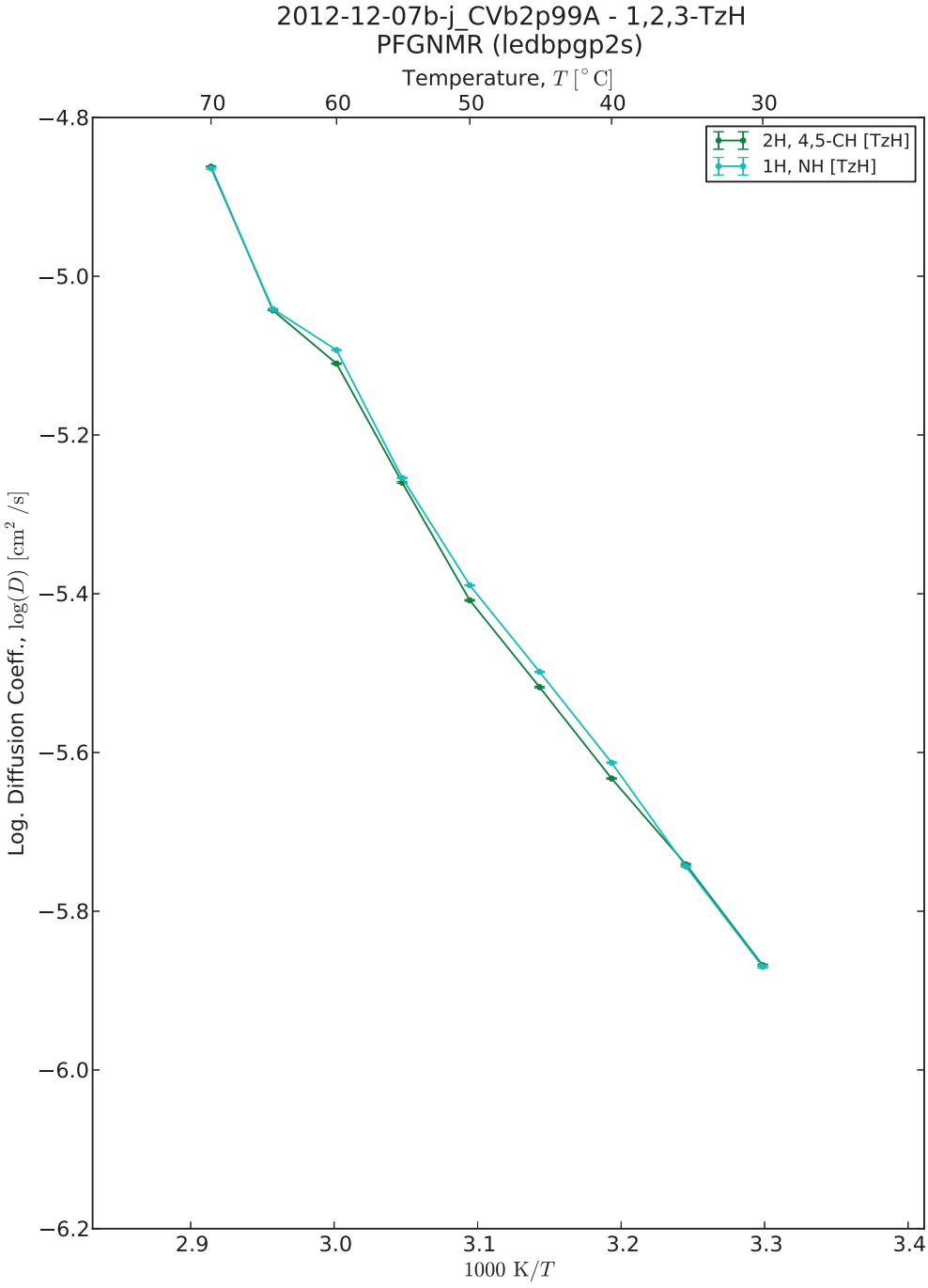


**Figure 5.10.** Arrhenius plot of $^1$H diffusivities (self-diffusion coefficients) in solvent-free 1,2,3-triazole, acquired on heating from 30 °C to 70 °C.

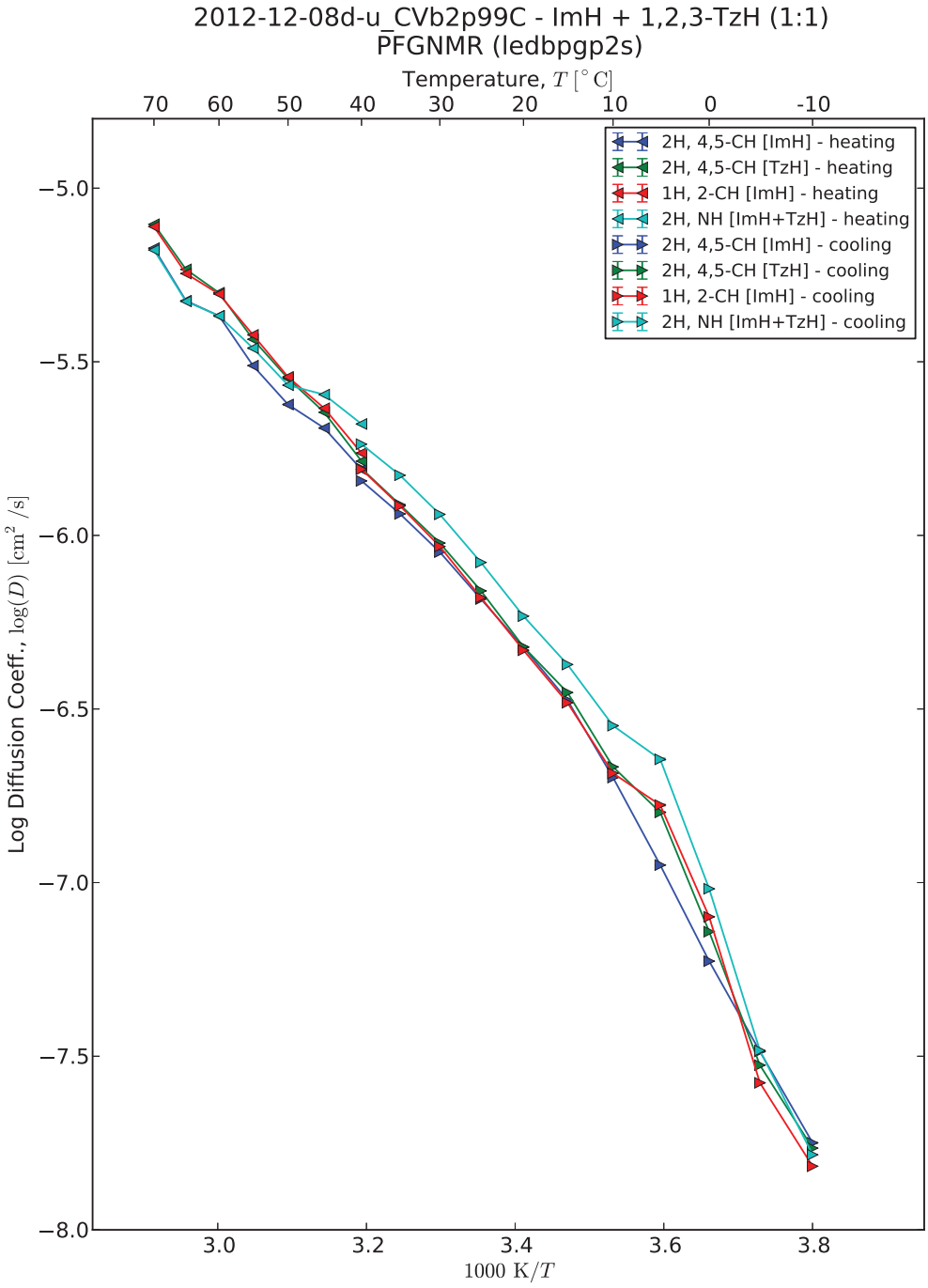


**Figure 5.11.** Arrhenius plot of $^1$H diffusivities (self-diffusion coefficients) in solvent-free mixture of imidazole + 1,2,3-triazole (1:1). The first leg from 40 °C to 70 °C was acquired upon heating; whereas, the second leg was acquired on cooling from 40 °C down to −10 °C.

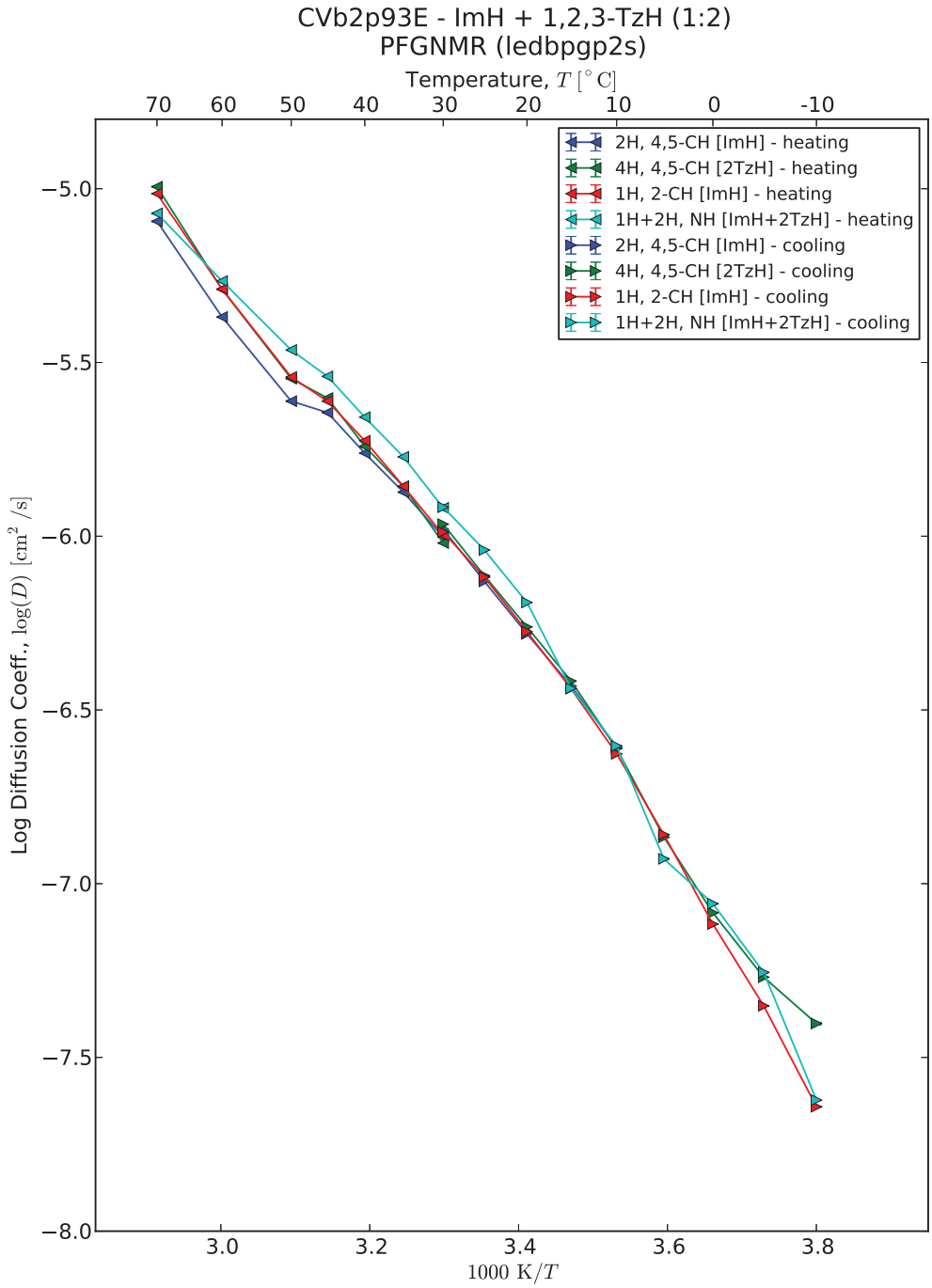


**Figure 5.12.** Arrhenius plot of $^1$H diffusivities (self-diffusion coefficients) in solvent-free mixture of imidazole + 1,2,3-triazole (1:2). The first leg from 30 °C to 70 °C was acquired upon heating; whereas, the second leg was acquired on cooling from 30 °C down to −10 °C. Note, the coldest 4 points for the (2H, 4,5-CH [ImH]) *blue* line were removed because the DOSY data was too distorted to properly fit.

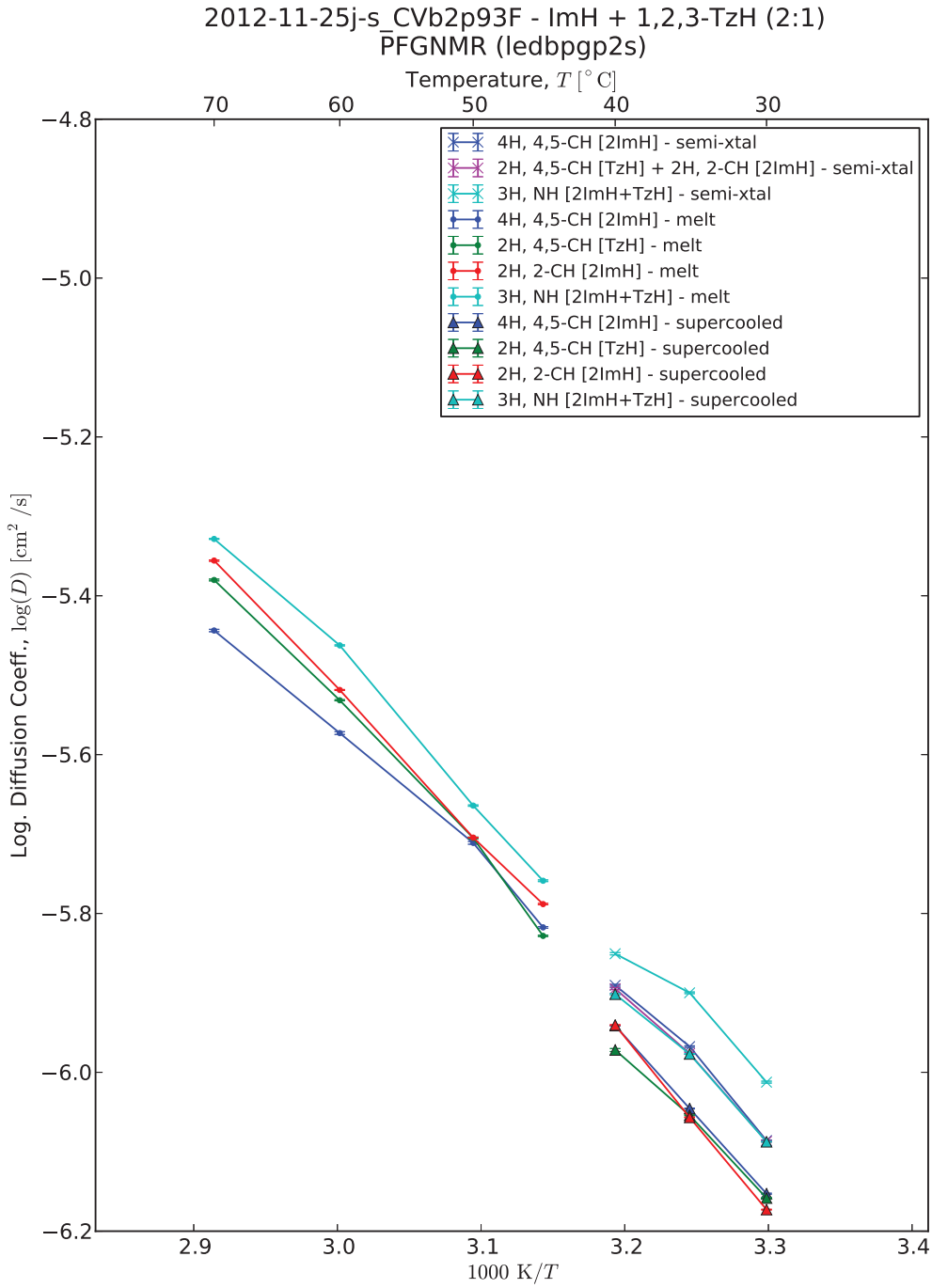


**Figure 5.13.** Arrhenius plot of $^1$H diffusivities (self-diffusion coefficients) in solvent-free mixture of imidazole + 1,2,3-triazole (2:1). The acquisition starts at 30 °C where the sample is semi-crystalline – here spectral resolution is much lower as the sample is semi-solid, so the (2-CH [ImH], *red*) and (4,5-CH [TzH], *green*) lines are indistinguishable and thus lumped into one line (*magenta*). Above 40 °C the sample is molten. Data up to 70 °C is acquired on heating. Then upon cooling the system enters a supercooled state where it is measured again from 40 °C to 30 °C.

CH [ImH], *blue*), (4,5-CH [TzH], *green*) and (2-CH [ImH], *red*) lines and labeled $D(\mathrm{H_{CH}})_{\mathrm{avg}}$. The solid and dashed lines are best fit interpolations using a Vogel-Fulcher-Tammann (VFT) style equation [25] of the form

$$y = p_0 \exp\{-p_1 x/(1 - p_2 x)\} \tag{5.16}$$

where $x = 1000/T$ and $y = D$ – with this 3 parameter function there are only $k = 2$ degrees of freedom remaining for each 5 point set – so we are not very confident of extrapolations outside this curve. [7] This interpolation serves two purposes: the first is to enable recalibration of the errors for the data points, where a scaling has been applied to each set in order to approximately normalize the goodness of fit parameter $\chi^2/k$; the other reason is to smooth the calculation of $\sigma^{\mathrm{structure}}$ (see eq. 5.9), which in our case depends on the difference $D(\mathrm{H_{NH}}) - D(\mathrm{H_{CH}})_{\mathrm{avg}}$, a rather noisy comparison (see the next section 5.6).

For comparison to the self-diffusion data (in the restricted range), proton conductivity data was also acquired for these samples – shown here separately in the full temperature range from 70 °C down to −40 °C cooling stepwise by 5 °C every hour – using the high-throughput impedance system describe in chapter 2. (See figure 5.15.) The conductivity of the mixtures including both triazole and imidazole are more than an order of magnitude higher than that of the neat 1,2,3-triazole. On the other hand, neat 1,2,3-triazole has the highest proton diffusivity - a quantity which is correlated with mobility (through the Nernst-Einstein relation, eq. 5.3); whereas, in all tested mixtures, a higher proportion of imidazole correlates to lower diffusivities. These data support the hypothesis that the mechanism for the enhancement of conductivity in these mixtures is a large increase of the charge carrier density over

[7] VFT models are typically used to model viscosity over temperature in glasses, which is similar to the dependence of self-diffusion in these liquids that become appreciably viscous at lower temperatures.

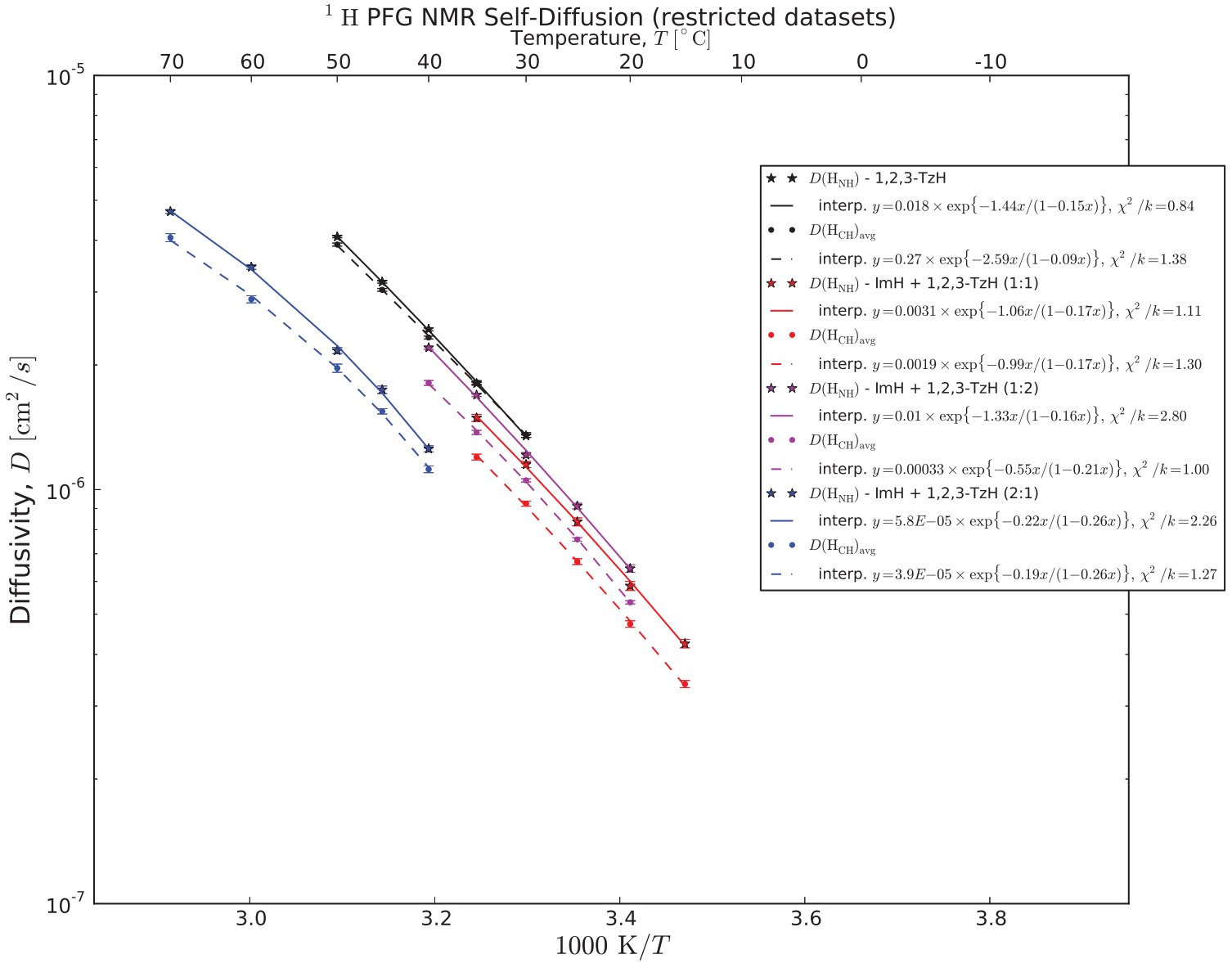


**Figure 5.14.** Arrhenius plot of $^1$H diffusivities (restricted dataset) for labile protons, $D(\mathrm{H_{NH}})$ (*stars*), and for molecule-bound protons, $D(\mathrm{H_{CH}})_{\mathrm{avg}}$. The solid and dashed lines are best fit interpolations using a Vogel-Fulcher-Tammann (VFT) style equation [25].

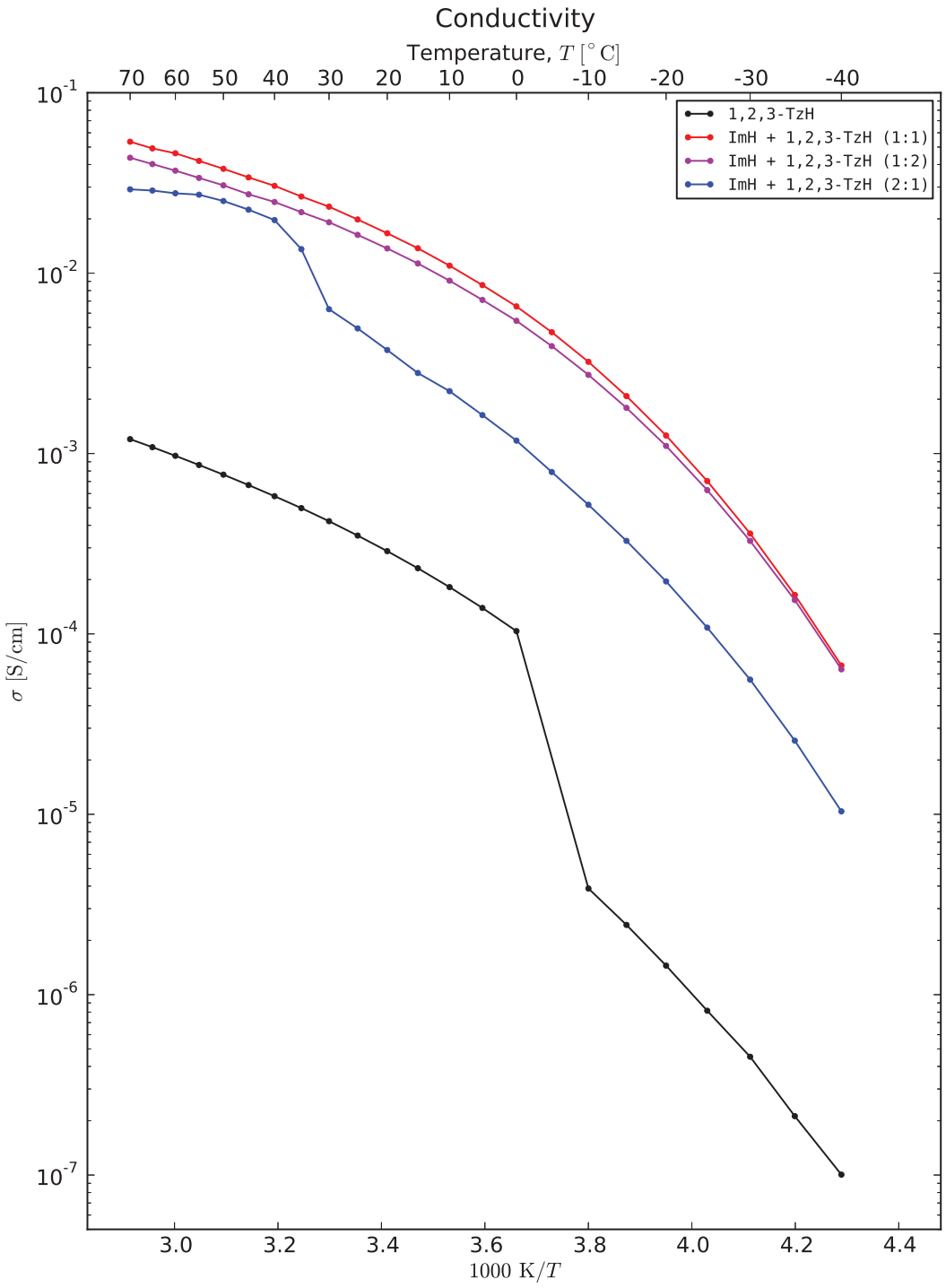


**Figure 5.15.** Arrhenius plot of conductivity for imidazole and 1,2,3-triazole mixtures upon cooling stepwise by 5 °C every hour – the last point taken for each step.

the pure materials, despite the assumed small decrease in charge mobility over the pure triazole liquid. This hypothesis also accords with the theoretical evidence for thermodynamically favored co-ionization reaction between imidazole and triazole in a model ideal gas system which was discussed in 4.2 (see also [9]).

## 5.6 Analysis of Derived Charge Transport Parameters

This subsequent analysis will attempt to provide parallels to various derived charge transport parameters found in the literature; a sincere effort is made to note where important assumptions must be made in order to proceed with some calculation. Following Schuster's prescription [55] we compute

$$\sigma_D^{\text{structure}} \approx \frac{e^2}{k_B T} n(\mathrm{H_{NH}}) \left( D(\mathrm{H_{NH}}) - D(\mathrm{H_{CH}}) \right) \tag{5.17}$$

where we approximate the number density of labile protons in all samples as the number density for 1,2,3-triazole

$$n(\mathrm{H_{NH}}) \approx n(\mathrm{TzH}) = N_A \frac{\rho}{m} = 6.022 \times 10^{23}\,\mathrm{mol}^{-1} \frac{1.23\,\mathrm{g/cm}^3}{68.077\,\mathrm{g/mol}} = 1.09 \times 10^{22}\,\mathrm{cm}^{-3} \tag{5.18}$$

and compare this to the measured conductivity $\sigma$. (See figure 5.16) (Note that the data used here for the diffusivities was not directly measured but taken from the interpolated curve in figure 5.14) Accordingly, the ratio of these two conductivities is denoted as the Haven ratio for the structural diffusion (Grotthuss) mechanism $H_R^{\text{structure}} = \sigma_D^{\text{structure}}/\sigma$. For all the mixtures $H_R^{\text{structure}} < 1$ in the investigated range, excepting Im+TzH(2:1), with the possibility of turning over at higher temperatures; whereas, for the neat TzH sample $H_R^{\text{structure}} > 1$ even reaching $\sim 10$.

Another complementary way to look at the data is to compute a diffusivity from the measured conductivity, $D_\sigma = k_B T \sigma / e^2 n$ (eq. 5.7), and compare that to the overall measured $^1$H PFG NMR diffusivity to derive a Haven ratio for the vehicle mechanism

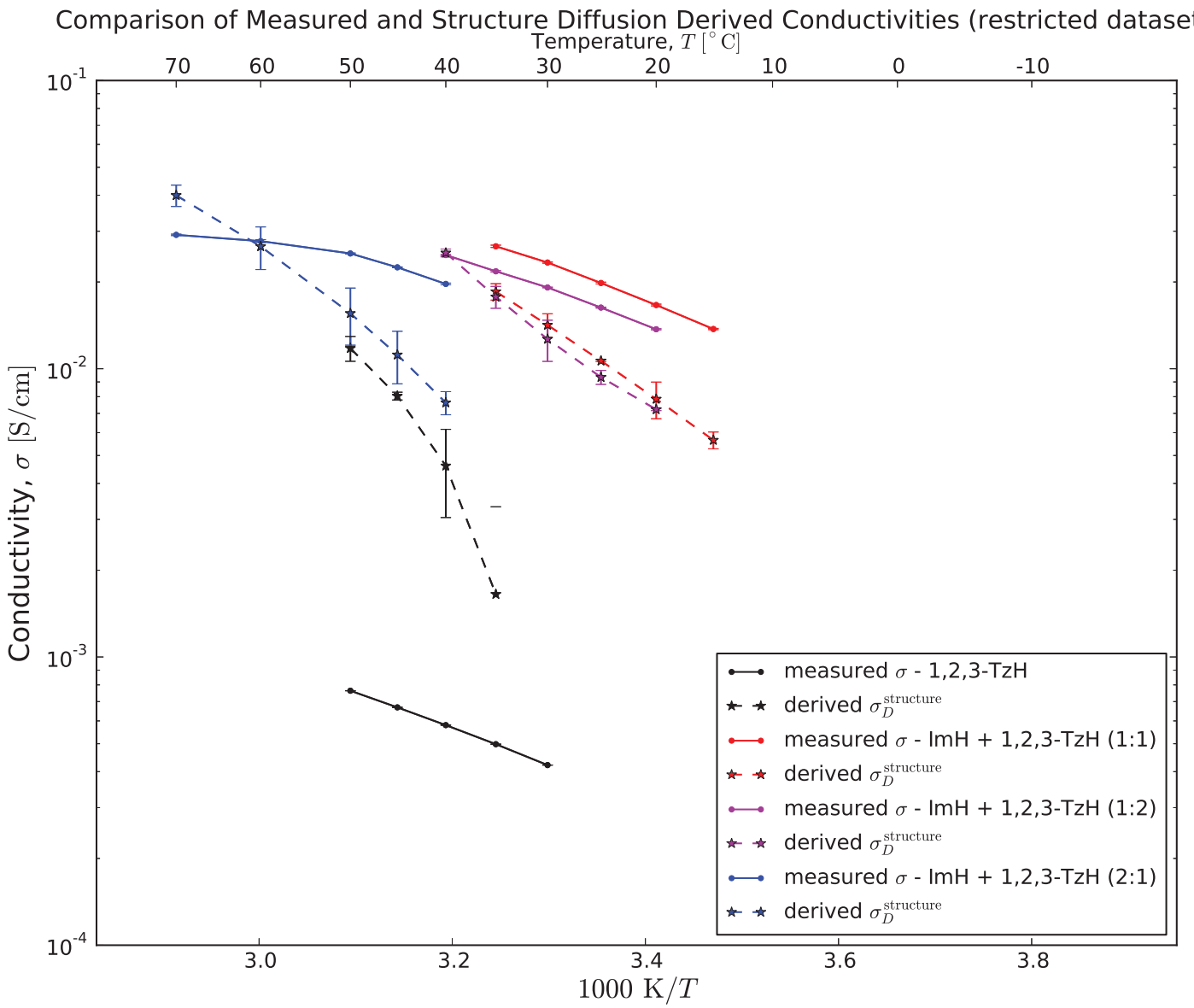


**Figure 5.16.** Arrhenius plot of measured and $^1$H PFG NMR diffusivity derived conductivity for imidazole and 1,2,3-triazole mixtures. The quantity $\sigma_D^{\text{structure}}$ is computed from the interpolated diffusivity curves in figure 5.14 in order to reduce noise, which has been transformed into the error-bars.

$H_R^{\text{vehicle}} = D(\text{H}_{\text{CH}})_{\text{avg}}/D_\sigma$; however, this requires an assumption to be made about the charge carrier density $n$ of which we know very little. Instead, we feel that a more intuitive way to handle this uncertainty is first to assume that the Nernst-Einstein relation holds, i.e. $H_R^{\text{vehicle}} \equiv 1$; then, compute an effective charge carrier number density based on these assumptions

$$\tilde{n}^{\text{vehicle}} = \frac{k_b T}{e^2} \frac{\sigma}{D(\text{H}_{\text{CH}})_{\text{avg}}} \tag{5.19}$$

which has dimensions that we can reason about. (See figure 5.17.) It would be reasonable to put an upper bound on the real charge carrier density as twice that of the molecular density of 1,2,3-triazole, assuming complete dissociation into opposite charged pairs. Note the trend of $\tilde{n}^{\text{vehicle}}$, higher at lower temperatures, is opposite from what would normally be expected, which is that dissociation is activated by thermal energy – this further justifies the need for an additional factor to explain the failure of the initial assumptions, which, of course, is the purpose of a Haven ratio. Surprisingly, the trend seems to fit an (inverse) Arrhenius dependence ($\tilde{n}^{\text{vehicle}} \propto \exp(p/T)$, for constant $p$) quite well. But we can't know $H_R^{\text{vehicle}}$ independently of the true $n$ which likely has its own temperature dependence; so we will settle for computing an "effective" dimensionless factor which accounts for these discrepancies, called the *effective Haven ratio*

$$\tilde{H}_R^{\text{vehicle}} \propto 1/\tilde{n}^{\text{vehicle}} \tag{5.20}$$

where we stipulate that this quantity approaches unity at high temperatures [8]

[8]This constraint implicitly assumes that all of the measured conductivity can be explained by a vehicle mechanism and the Nernst-Einstein relation in the limit of temperature going to infinity, which seems reasonable for a viscous liquid model; and, furthermore, it is consistent with divergence of $H_R^{\text{structure}}$ at high temperatures, which is believed to be due to the relative diminishment of the enhancement that structural diffusion contributes to conductivity.

$$\lim_{T\to\infty} \tilde{H}_R^{\text{vehicle}}(T) = 1 \tag{5.21}$$

so that

$$\tilde{H}_R^{\text{vehicle}} = \frac{\lim_{T\to\infty} \tilde{n}^{\text{vehicle}}(T)}{\tilde{n}^{\text{vehicle}}} \tag{5.22}$$

Using eq. 5.22, we extrapolate the data trends to infinite temperature using a best fit function of the form

$$y = p_0 \exp(p_1 x) \tag{5.23}$$

where $x = 1000/T$ and $y = \tilde{n}^{\text{vehicle}}$, such that $p_0 \approx \lim_{T\to\infty} \tilde{n}^{\text{vehicle}}(T)$. Finally, we compute $\tilde{H}_R^{\text{vehicle}}$ and refit it with an Arrhenius function

$$y = p_0 \exp(-p_1 x) \tag{5.24}$$

where for each sample $p_0 \approx 1.00 \pm 25\%$ and we can compute *activation energies*, $E_a = 1000 k_B p_1$. (See figure 5.18 and data in table 5.2.) These *activation energies* determine the relative rates at which derived proton transport assuming only a vehicle mechanism diverges from the observed charge transport; an effect which depends both on thermal activation of charged defects and of charge carrier mobility through a reduction of viscosity. In the case of charged defect creation, the activation energy includes the enthaply of formation of the products as well a barrier term for the formation of an unstable intermediate "activated complex" form (or multiple complexes) through which the coionization reaction must proceed. For mobility, an activation of the Vogel-Fulcher-Tammann (VFT) type [25] is expected since these hydrogen-bonded viscous liquids take on glassy dynamics at lower temperatures. That the activation energies for the mixtures Im+TzH are much higher than neat TzH is thought to be associated primarily with an order of magnitude higher charge carrier density and its associated increase in observed conductivity. (See figure 5.15.)

The secondary ordering among the mixtures might be driven by an increase in viscosity with the higher proportion of ImH, which is evidenced in the ordering of the overall proton self-diffusivities. (See figure 5.14.)

**Table 5.2.** Table of Arrhenius fits of form $y = p_0 \exp(-p_1 x)$ of *effective Haven ratio* for the vehicle mechanism. Data comes from figure 5.18. $E_a = 1000 k_B p_1$ is the relative *activation energy* which describes the relative rate at which tracer particle diffusion fails to account for the observed conductivity.

| **Sample** | $p_0$ | $p_1$[K] | $E_a$ [meV] |
|---|---|---|---|
| 1,2,3-TzH | $1.00 \pm 0.22$ | $1.9525 \pm 0.0683$ | $168 \pm 6$ |
| ImH + 1,2,3-TzH (1:1) | $1.00 \pm 0.22$ | $2.4344 \pm 0.0652$ | $210 \pm 6$ |
| ImH + 1,2,3-TzH (1:2) | $1.00 \pm 0.23$ | $2.5850 \pm 0.0684$ | $223 \pm 6$ |
| ImH + 1,2,3-TzH (2:1) | $1.01 \pm 0.26$ | $2.8065 \pm 0.0823$ | $243 \pm 7$ |

## 5.7 Conclusions

Though conductivity itself is an intensive (bulk) material property, its measurement using impedance spectroscopy relies on a ratio of extensive quantities (see section 1.2.4) which are typically macroscopic; therefore, these measurements are believed to be probing long-range and long-time scales with respect to the relative spacing of free charge carriers. Indeed, the conductivity of these materials is frequency independent from well below the characteristic dielectric relaxation time scale $\tau = \epsilon/\sigma$ [9] down to the time scale associated with electrode polarization (cell geometry dependent, could be arbitrarily long). On the other hand, the diffusivity measurements by PFG NMR are sometimes claimed to be probing much shorter length and time-scale effects, which are related by the equation

$$x = \sqrt{Dt} \tag{5.25}$$

[9] $\tau \approx 0.1 - 100 \times 10^{-12}$ s is a rough estimate assuming $\epsilon_r = 1$ and $T = 70\,^{\circ}\mathrm{C}$

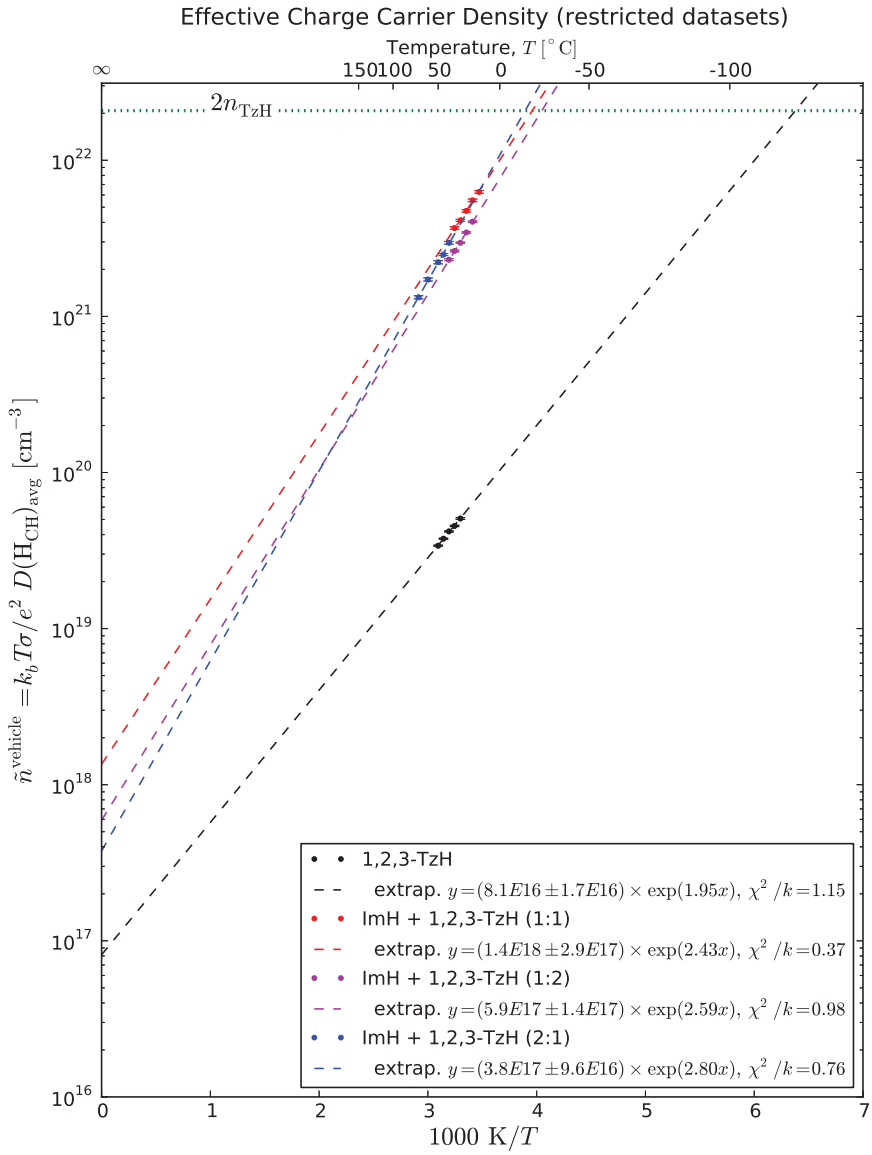


**Figure 5.17.** Arrhenius plot of *effective charge carrier density*, based on the (erroneous) assumption that the Nernst-Einstein relation holds, i.e. $H_R \equiv 1$, and all conductivity is explained by a vehicle mechanism. The line at $2n_{\mathrm{TzH}} = 2.18 \times 10^{22}\,\mathrm{cm}^{-3}$ is an estimated upper-bound on any realistic charge carrier density; it is based on the room-temperature density for 1,2,3-triazole. That this plot shows positive slopes which would be unphysical for a reasonable estimate of an actual charge carrier density is why we must strongly caution against that interpretation (see the text for details).

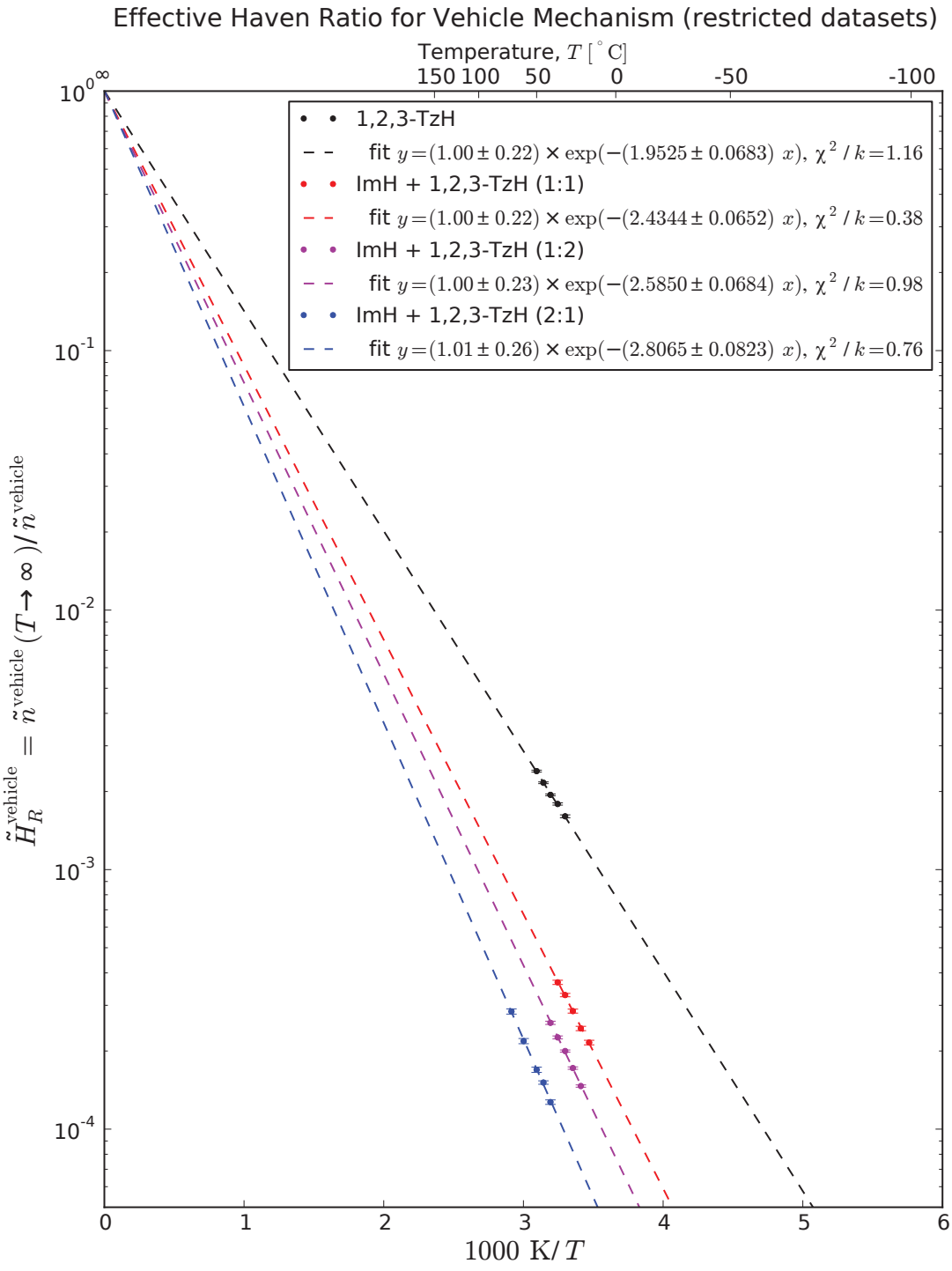


**Figure 5.18.** Arrhenius plot of *effective Haven ratio* for the vehicle mechanism. Fits of form $y = p_0 \exp(-p_1 x)$ have been applied.

where $x$ and $t$ are the diffusion length and time, respectively. The DOSY parameter $\Delta$ is a good estimate of the diffusion time, assuming for our samples a typical diffusivity $D \approx 1 \times 10^{-10}\,[m^2/s]$ and the smallest time scale used was $\Delta = 0.025\,\mathrm{s}$, so $x \approx 1 \times 10^{-6}\,\mathrm{m}$ – contrast this figure to the intermolecular length scale estimated as $n_{\mathrm{TzH}}^{-1/3} \approx 1 \times 10^{-8}\,\mathrm{m}$.

Despite the limited quality of the data, we are tempted to conclude that a transition occurs in these amphiprotic viscous liquid systems such that at high temperatures correlations in proton exchange favor short-range diffusion mechanisms but at lower temperatures there is a cross-over where long-range conduction of charge is prevalent despite the very low proton self-diffusivity. One possible explanation of this effect is the onset of a conduction mechanism that is akin to *vacancy diffusion* in alkali glasses – the original context of the Haven ratio. (See beginning of section 5.2.) Note that the ImH+TzH mixtures likely have significantly higher degrees of charge separation than the neat TzH because of enhanced probability of coionization (see last paragraph in section 4.2); this effect would give rise to a higher population of locally excess protonic charges (as well as proton vacancies) but also might contribute to faster proton exchange if there is significant hydrogen bonding interactions at these defect sites. Furthermore, note the decreasing trend in *overall* proton self-diffusivity (and viscosity by extension) with increasing ImH content. These two factors would tend to drive the transition to higher temperatures which is consistent with the observed trends. As the medium's viscosity increases with lowering temperatures, the movement of the molecules will become increasingly more constrained; and, though translations may become improbable, rotations might remain. If charged defects transfer to other molecules via hopping, then molecular reorientation is still necessary for continued conduction of net charge over long distances – a fact well known in the literature about proton transfer via Grotthuss mechanisms. [36] [29]

Future work could be done to characterize the viscosity of these liquid mixtures over temperature and relate that to conductivity. The *Stokes-Einstein* relation models the diffusivity of a given ion (with effective radius $r_i$) in terms of a hydrodynamic drag effect

$$D_i = \frac{k_B T}{6\pi\eta r_i} \tag{5.26}$$

where $\eta$ is the viscosity of the medium – note that this is just a type of vehicle-mechanism. Using the familiar *Nernst-Einstein* relation, here restated in terms of a partial equivalent conductivity

$$\lambda_i = \sigma_i / c_i = \frac{z_i^2 D_i}{k_B T} \tag{5.27}$$

the *Walden rule* predicts a dependence between the total equivalent conductivity $\Lambda = \sum_i \lambda_i$ and the viscosity of an electrolyte, namely

$$\Lambda\eta = const. \tag{5.28}$$

[3] A convenient visualization of this dependence is the *Walden plot*, $log(\Lambda(T))$ vs. $log(\eta^{-1}(T))$, where systems that obey this rule fall on the line of slope 1 (e.g., many dilute salts in solvents). Other systems characterized by plots falling above this line on the Walden plot are known as "superionic" liquids or glasses, depending on the magnitude of the viscosity. We believe, consistent with the diffusivity-conductivity comparison, that the heterocycle mixture liquids would fall in this superionic zone. In other words, the Stokes-Einstein model would fail to explain the excess conductivity at lower temperatures, ruling out this form of vehicle mechanism.

# CHAPTER 6

# IMPEDANCE SPECTROSCOPY STUDY OF ELECTRODE POLARIZATION IN VARIOUS ELECTROLYTES

After examining the bulk conductivity of many proton and other ion conducting samples using impedance spectroscopy (which amounts to extracting one simple spectral feature), little is known about the ever-present, yet highly varied, electrode polarization response seen in the low-frequency limit, which accounts for the majority of interesting spectral variation. The data thus far has been complicated by the lack of control of the electrode surfaces used in our typical conductivity studies. It is therefore a natural extension of previous work to try to understand these interfacial phenomena and to build empirical models guided by theory and simulation, by careful preparation and variation of the conditions that give rise to these elaborate impedance spectra. A more complete understanding of the full impedance spectrum at model interfaces might reveal more information about the charge transport mechanisms of the particular electrolyte.

## 6.1 Electrode Polarization

Electrochemical potential differences between electrode surfaces and the electrolyte bulk may exist at equilibrium (with no net faradaic current passing in the cell), leading to excess concentrations and gradients of charged species at these interfaces. An *ideal polarizable electrode* allows no transfer of charge across the interface, blocking faradaic currents; such an interface can be experimentally realized to various degrees of approximation by using relatively inert electrode materials within a limited

applied voltage range avoiding electrochemical reactions in the cell. In contrast, an electrode that is *ideally non-polarizable* will allow the passage of faradaic current without changing its potential; such electrodes are well approximated by electrochemically reversible reactions taking place within an environment containing stable concentrations of reactants and products, like those found in standard reference electrodes. The study of ionic charge gradients and oriented dipoles, known as the *electrical double layer*, at polarized electrode interfaces has been termed "electrocapillarity" due to its connection with the surface tension between metals and inert salt solutions. [27]

Electrode polarization effects give rise to the low frequency impedance response seen in charge blocking electrode cells for measuring electrolyte conductivity. Although the behavior of the electrical double-layer can create complicated responses that depend on physical and specific chemical interactions between electrode surfaces and species in the electrolyte, the study and careful control of parameters that affect this system may help to reveal additional charge transport properties of electrolytes beyond simply bulk conductivity and dielectric constant.

## 6.2 Thermodynamics of Charge Adsorption at Ideal Polarizable Electrode

The thermodynamics governing surface charge adsorption at an ideal polarizable electrode/electrolyte interface at constant temperature can be derived from Gibbs adsorption isotherm formalized by Grahame in 1947 [27]; adapting the more modern notation of Bard and Faulkner [6]:

$$-d\gamma = \sigma_M(dV - dV_{\text{ref}}) + \sum_i \Gamma_i d\mu_i \tag{6.1}$$

where $\gamma$ is the surface tension between the immiscible phases, $\sigma_M$ is the surface charge density of the electrode phase, $V$ is an applied electric potential, $V_{\text{ref}}$ is the potential

drop between a far removed second reference electrode and the electrolyte bulk, $\Gamma_i$ is a surface excess for a species, and $\mu_i$ is the chemical potential for a species. A plot of $\gamma$ as a function of $V$ is referred to as the *electrocapillary curve*. At constant composition where each $\mu_i$ is a constant and the reference potential is assumed stable, $dV_{\text{ref}} = 0$, the negative slope of the electrocapillary curve is the surface charge density

$$\sigma_M = -\left(\frac{d\gamma}{dV}\right)_\mu \tag{6.2}$$

and the curvature is related to the *differential capacitance*

$$C_{\text{d}} = -\left(\frac{d^2\gamma}{dV^2}\right)_\mu = \left(\frac{d\sigma_M}{dV}\right)_\mu \tag{6.3}$$

A maximum in the electrocapillary curve occurs when the net surface charge $\sigma_M = 0$ at a special potential known as the *point of zero charge* (PZC). This simplified thermodynamic model predicts that the ideal polarizable interface will exhibit a capacitance that can vary as a function of applied voltage.

## 6.3 Double-Layer Structure

The term "double-layer" is rather a misnomer, as the phenomenology of the electrode/electrolyte interface is more generally described by a surface charge at the electrode and up to three charge layers in solution [27] (for simplicity a planar electrode geometry with one dimensional distance $x$ is considered): neutral or charged species may adsorb to the electrode surface at the *inner Helmholtz plane* (IHP) at position $x_1$; solvated ions can approach within several angstroms of surface, forming a compact planar charged surface, called the *outer Helmholtz plane* (OHP) at position $x_2$; and a *diffuse layer* of excess charge gradients extends from the OHP into the bulk. The two compact charge layers can have potentials, $\phi_1 = \phi(x_1)$ for the IHP

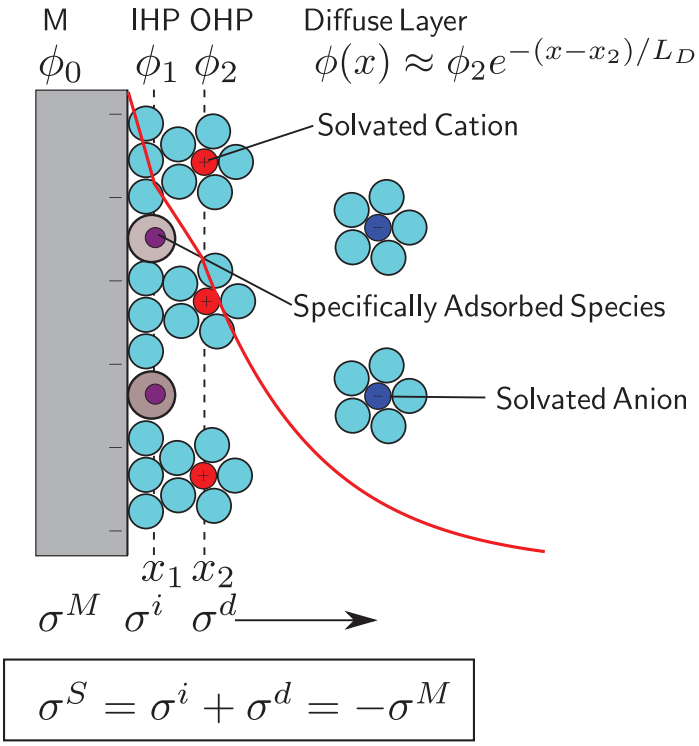


$$\sigma^S = \sigma^i + \sigma^d = -\sigma^M$$

**Figure 6.1.** Schematic of double-layer structure for symmetric electrolyte with possible specific adsorption phenomena. The hypothetical normalized variation in electrical potential, $\phi/\phi_0$, is depicted as a red curve with boundary conditions $\phi_0$ for the metal surface $M$ at $x = 0$, $\phi_1$ at the inner Helmholtz plane (IHP) at $x = x_1$, and $\phi_2$ at the outer Helmholtz plane (OHP) at $x = x_2$. Potential varies linearly in the compact layers ($0 < x < x_2$) and will have a discontinuity in slope if charge $\sigma_i$ resides at the IHP. After the OHP, in the diffuse layer, the potential has an approximate exponential dependence of characteristic Debye length $L_\mathrm{D}$ (see equation 6.9) which holds for $ze\phi_2 \ll 4k_BT$.

and $\phi_2 = \phi(x_2)$ that are shifted positive or negative of the applied electrode potential $\phi_0 = \phi(0)$.

The *Gouy-Chapman* model assumes the distribution of charges in the diffuse layer follows Boltzmann statistics for the concentration $n_i$ of charged species in a planar lamina at position $x$ based on only the electrical potential $\phi$ at that location:

$$n_i(x) = n_i^0 \exp\left(\frac{-z_i e\phi(x)}{k_B T}\right) \tag{6.4}$$

where $n_i^0$ is the bulk concentration and $z_i$ is the valance. Applying electrostatics to this charge distribution for all ionic species yields the *Poisson-Boltzmann* equation:

$$\frac{d^2\phi}{dx^2} = -\frac{e}{\epsilon}\sum_i n_i^0 z_i \exp\left(\frac{-z_i e\phi(x)}{k_B T}\right) \tag{6.5}$$

The Stern modification of this model, which accounts for the effect of the compact charge layers, amounts to cutting off the diffuse layer at the OHP (where $x = x_2$) and applying the potential $\phi_2$ at that boundary.

Analytical solution of the Gouy-Chapman-Stern model is possible for the case of a symmetric electrolyte ($n_1^0 = n_2^0 \equiv n^0$, $z_1 = z_2 \equiv z$). Around the point of zero charge ($\phi_0 = \phi_{\mathrm{Z}}$), the effects of the IHP can be neglected. Assuming a planar electrode with area $A$, the model predicts a differential capacitance $C_{\mathrm{d}}$ that can be treated as a series combination of a voltage independent *Helmholtz capacitance* $C_{\mathrm{H}}$ for the compact layer and a voltage dependent *diffuse layer capacitance* $C_{\mathrm{D}}$:

$$C_{\mathrm{d}} = \frac{1}{1/C_{\mathrm{H}} + 1/C_{\mathrm{D}}} \tag{6.6}$$

$$C_{\mathrm{H}} = \frac{\epsilon A}{x_2} \tag{6.7}$$

$$C_{\mathrm{D}} = \frac{\epsilon A}{L_{\mathrm{D}}}\cosh\left(\frac{ez\phi_2}{2k_B T}\right) \tag{6.8}$$

with the effective *Debye length* of the solution defined as

$$L_{\mathrm{D}} = \sqrt{\frac{\epsilon k_B T}{2n^0 e^2 z^2}} \tag{6.9}$$

For aqueous electrolytes, the OHP is spaced out to approximately the length of two water monolayers, $x_2 \approx 0.3\,\mathrm{nm}$; thus the Helmholtz capacitance is around $C_{\mathrm{H}} \approx 236\,\mu\mathrm{F/cm^2}$. Around the PZC, the diffuse layer capacitance for an aqueous electrolyte at room temperature is approximately $C_{\mathrm{D}} \approx 228 z C^{*1/2}\,\mu\mathrm{F/cm^2}$, where $C^*$ is the concentration in mol/L.

## 6.4 Experimental Considerations

Conventionally, many double-layer studies have been performed primarily using a dropping mercury electrode (DME) cell with reversible aqueous reference electrodes, since this fresh droplet of liquid metal provides an atomically smooth, clean, surface with uniform surface tension, enabling a close comparison to simple models. The interfacial capacitance of a carefully prepared DME cell has been shown have little to no frequency dispersion with high salt concentration electrolytes.

However, the DME apparatus is cumbersome and would be extremely difficult, if not impossible, to apply to small quantities of viscous liquid or solid samples. Furthermore, the application of standard impedance spectroscopy sweeps would not be feasible on the changing droplet surface. The use of inert metal solid electrodes, though experimentally convenient, greatly complicates the interpretation of the interfacial impedance; frequency dispersion is typically seen and has been modelled with various circuits including the use of CPE elements – although not without considerable controversy [49]. Reproducibility of these results depends heavily on the surface preparation and elimination of confounding contaminants, such as oxygen and adventitious organic compounds.

We plan to model the electrode polarization response in the low frequency regime of impedance spectra using carefully prepared electrolytes in sealed Swagelok-type cells with various standard voltammetry working electrodes, gold, platinum, glassy carbon, and palladium. The electrolyte materials investigated will consist of low melting point small molecule proton conducting species and mixtures, as well as standard aqueous and nonaqueous salt solutions that will be used for calibration. Possibly, these studies might be carried over to solid polymer proton conductors, albeit with a different cell geometry. Proton charge is blocked by gold, platinum, and glassy carbon; thus no faradaic current is expected within a limited voltage range that avoids the reduction or oxidation of electrolyte species. The specific adsorption of protons onto these different electrode material is expected to vary. For example, platinum shows strong catalytic action for the hydrogen oxidation reaction and its reverse, proton reduction; whereas the kinetics of this reaction is inhibited at mercury surfaces – another reason that this metal has broad use in aqueous electrocapillary studies. [6] Palladium, on the other hand, is known to intercalate large quantities of hydrogen into its lattice, forming a conductive metal hydride; consequently, palladium hydride electrodes should show reversible proton selective boundary conditions [44]. The study of this proton transmitting interfacial impedance response might provide an interesting contrast to the blocking cells, as well as having significance to protonic devices constructed with these electrode materials. We will also investigate the feasibility of using chemically modified electrodes, such as alkane-thiol monolayers on gold [13], which may help to eliminate confounding effects like specific adsorption, better approximating an ideal polarizable electrode.

In order to find correlations between parameters of fit models and theory, we will vary the conditions of applied voltage, temperature, and electrolyte composition. The electrodes materials will be used in symmetric or mixed two probe configurations

as well as three-probe arrangements with a platinum wire pseudoreference (to be calibrated with an internal standard electroactive species, such as ferrocene [24]).

## 6.5 Example Voltage Biased Impedance Spectroscopy Data

Preliminary voltage dependent impedance data has been recorded for an aqueous test solution of 0.001 M lithium triflate at room temperature within a 3-probe cell using a 3 mm diam. gold working electrode, platinum counter electrode, and a platinum wire pseudoreference (uncalibrated) over the range of $-0.4\,\mathrm{V}$ to $0.4\,\mathrm{V}$. The voltage bias was stepped in units of 25 mV, equilibrated for 2 minutes, and an impedance spectrum was recorded while maintaining the bias. Cycle 1 starts at 0 V and goes to $0.4\,\mathrm{V}$, cycle 2 goes from $0.4\,\mathrm{V}$ down to $-0.4\,\mathrm{V}$, and cycle 3 goes from $-0.4\,\mathrm{V}$ up to $0.4\,\mathrm{V}$.

The same equivalent circuit model (see figures 6.2 and 6.3) was applied to each spectrum and each variable parameter was plotted against the voltage bias (see figure 6.4). Note that there is no unique circuit model for most spectra, and many variants will give a "good fit". It is perhaps too easy to read too much into the meaning of model parameters at this preliminary stage, but the following description is more of an educated guess. As usual, the model contains a solution resistance $R_0$ in series with a complicated electrode polarization response $Z_{\mathrm{EP}}$; the semicircular arc due to bulk polarization is distorted from parasitic effects so is excluded from the fit. We have chosen a particular model for $Z_{\mathrm{EP}}$, with two branches (1,2) of a CPE ($\alpha = 0.5$) in series with a capacitor C that are both in parallel to resistor $R_1$, based on its fit accuracy and simple physical interpretation of the parameters. $R_1$ leaks current in the low frequency limit; hence, the data might not represent an ideally blocking scenario, which may be due to faradaic effects like electrochemical changes or very slow non-faradaic effects. Very likely, contaminating oxygen is reduced at the electrodes leading to some faradaic charge transfer since no particular steps were taken to deaerate the

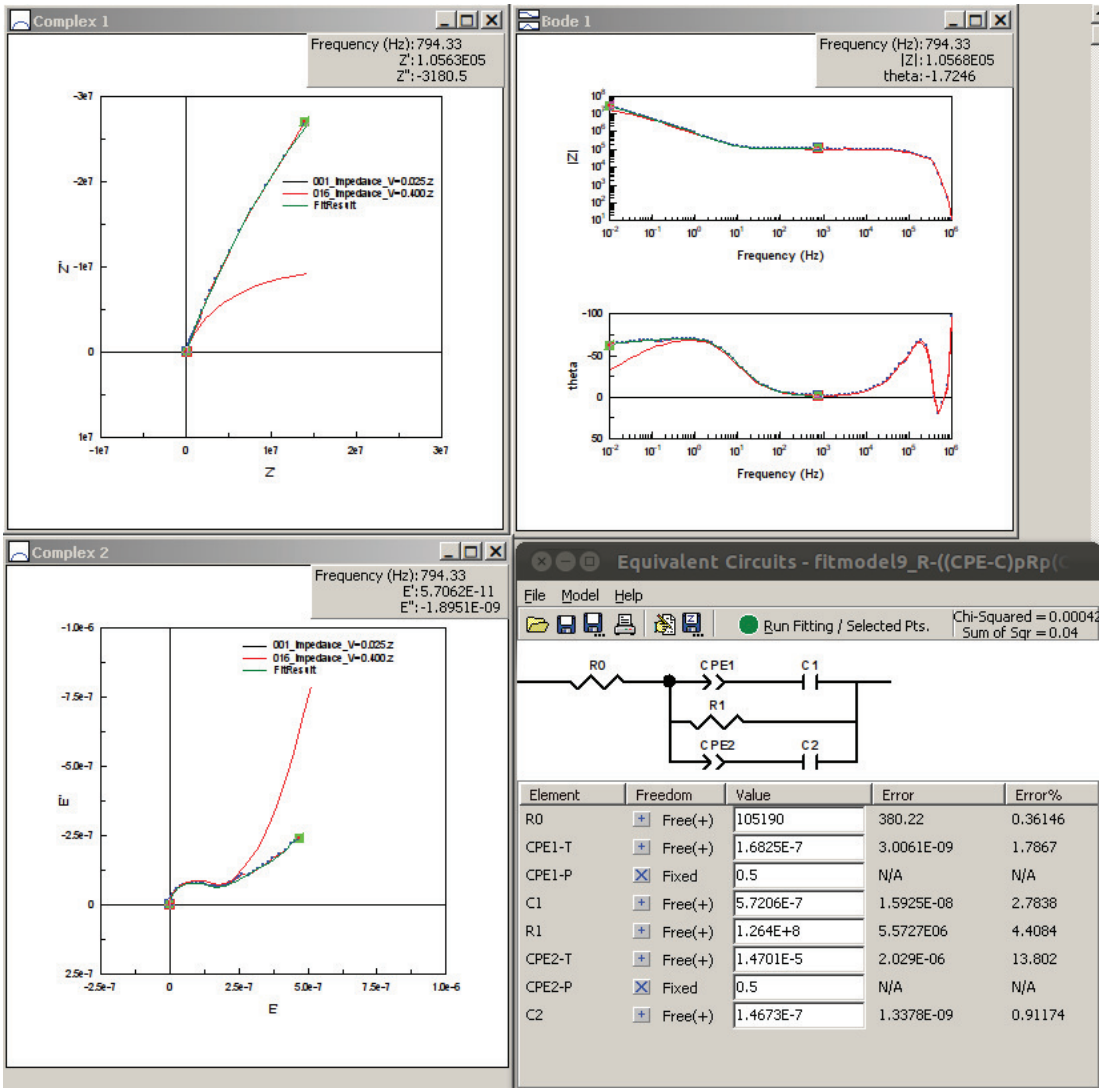


**Figure 6.2.** Example 1 of impedance spectrum fit to electrode polarization model. Fitted data (sequence #001) was taken at 0.025 V bias on first cycle, shown alongside another spectrum (sequence #016) taken at 0.400 V bias on first cycle. From top, left to right: Nyquist impedance plot, Bode impedance plot, Cole-Cole plot (complex capacitance), circuit model with fit.

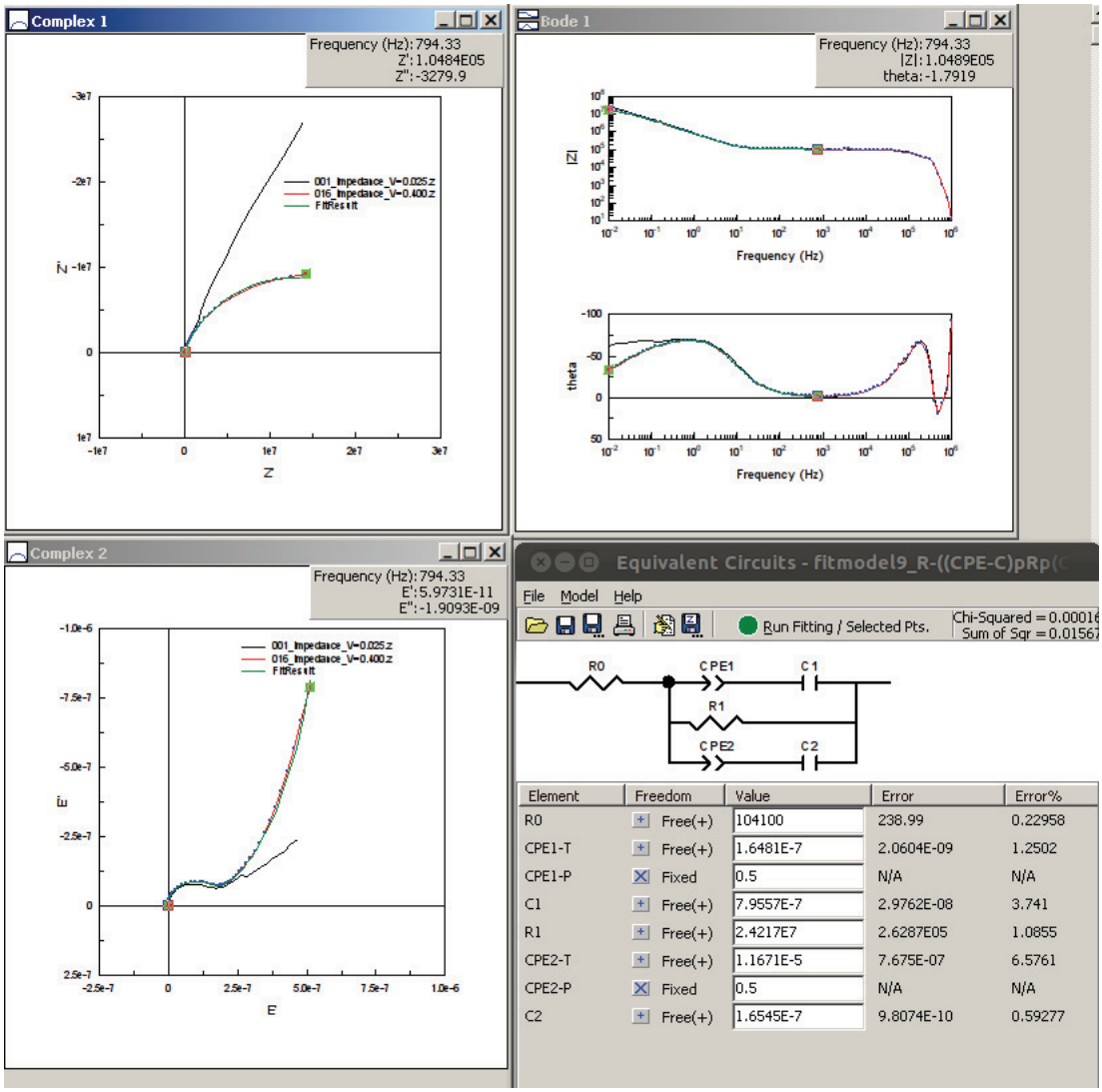


**Figure 6.3.** Example 2 of impedance spectrum fit to electrode polarization model. Fitted data (sequence #016) was taken at 0.400 V bias on first cycle, shown alongside another spectrum (sequence #001) taken at 0.025 V bias on first cycle. From top, left to right: Nyquist impedance plot, Bode impedance plot, Cole-Cole plot (complex capacitance), circuit model with fit.

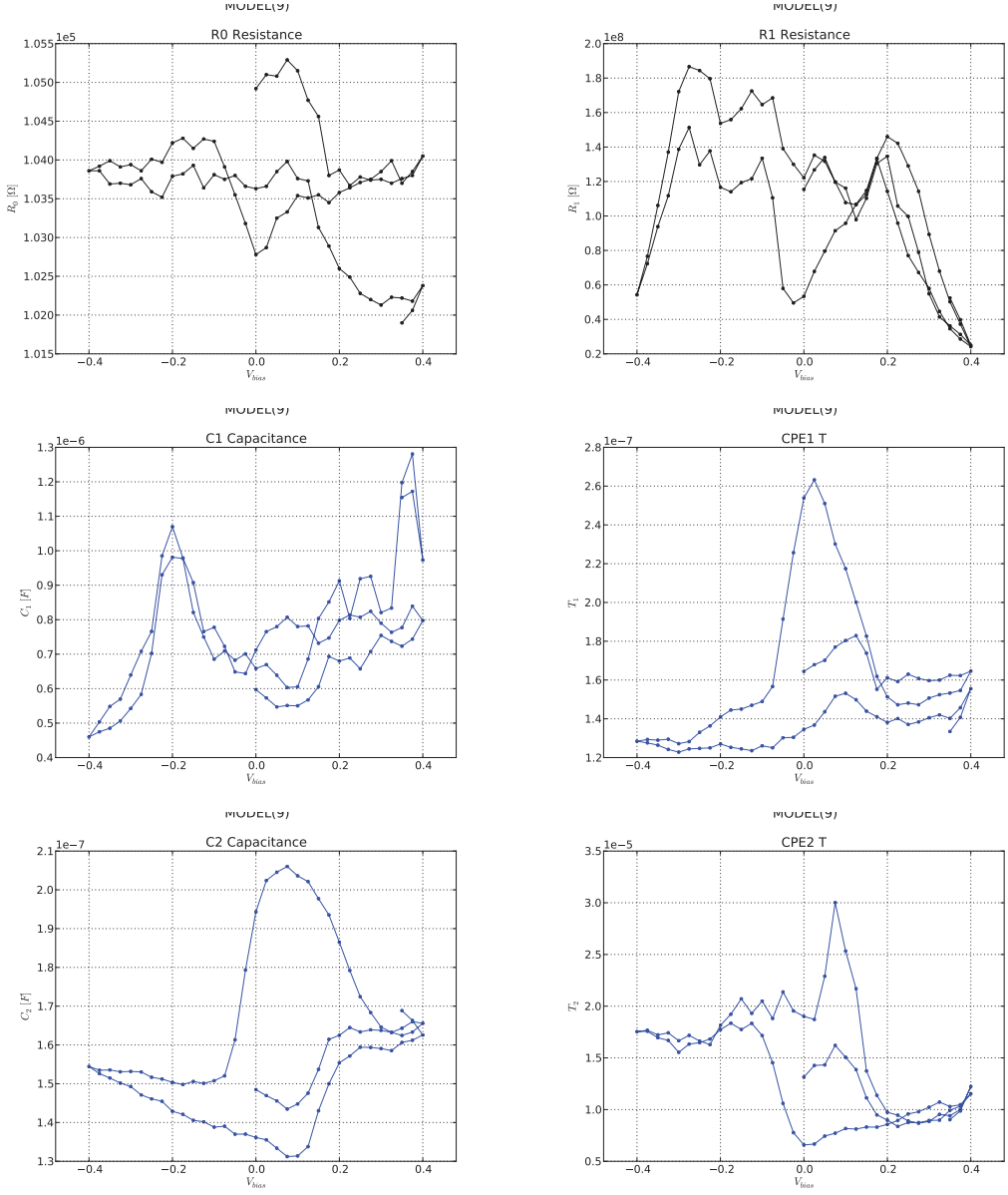


**Figure 6.4.** Fit model parameters as function of voltage bias (see model in figures 6.2 and 6.3) for 0.001 M aqueous lithium triflate at room temperature, using 3-probe cell with 3 mm diam. gold working electrode, platinum counter electrode, and platinum wire pseudoreference

solution. The two capacitance branches (1,2) are supposed to represent the double-layer charging response of either the cations or anions, respectively, which have very different physical and chemical properties – lithium is a small alkali metal cation with strong solvent complexation, whereas triflate is a large fluorinated organic anion with less tendency to form complexes. The $\alpha = 0.5$ constrained CPEs can be interpreted physically as Warburg diffusion elements with $T = 1/A_{\mathrm{W}}$ (see equation 1.24) that explain the dynamic response of charges in the diffuse layer for low concentration electrolytes. [7] An examination of the fit data over the subsequent voltage bias steps shows a complicated history dependent behavior; one possible explanation is the semi-reversible alteration of adsorbed ions and other contaminants with exposure to different potentials along with changes in the electrolyte composition at the electrode surface due to electrochemical reactions. Much work will have to be done to control and systematically vary the interfacial response if we are to arrive at a meaningful interpretation of these and similar experiments.

# APPENDIX

# BAYESIAN ANALYSIS OF NMR DATA

G. Larry Bretthorst has applied Bayesian statistics to the analysis of NMR data in a series of five papers entitled "Bayesian Analysis I-V". [14] [15] [16] [17] [18] In paper I [14], he lays out the mathematical formalism of the problem and derives a quite general solution. Many FID quadrature signals of interest can be treated with a general *phase-coherent* model, which is a sum of exponentially decaying sinusoids of different frequencies:

$$f_R(t) = \sum_{j=1}^{m} B_j \sin(\omega_j t + \theta) e^{-\alpha_j t} \tag{A.1}$$

$$f_I(t) = \sum_{j=1}^{m} B_j \cos(\omega_j t + \theta) e^{-\alpha_j t}, \tag{A.2}$$

where the $\mathbf{B} \equiv \{B_1, ..., B_m\}$ are linear amplitude parameters and $\Theta \equiv \{\omega_1, ..., \omega_n, \alpha_1, ..., \alpha_n, \theta\}$ are the nonlinear parameters. The model of the data points $i = 1..N$

$$d_R(t_i) = f_R(t_i) + e(t_i) \tag{A.3}$$

$$d_I(t_i) = f_I(t_i) + e(t_i), \tag{A.4}$$

includes channel independent *Gaussian additive noise* $e$. Bayes' theorem gives the *posterior probability* of the parameters

$$P(\Theta, \mathbf{B}|D, I) = \frac{P(\Theta, \mathbf{B}|I) P(D|\Theta, \mathbf{B}, I)}{P(D|I)}, \tag{A.5}$$

where $I$ is the set of *prior information* about the problem, $P(\Theta, \mathbf{B}|I)$ is identified as the *prior probability* of the parameters, $P(D|\Theta, \mathbf{B}, I)$ is the *direct probability* of the data, and $P(D|I)$ is the *marginal probability* of the data given only the prior information. The task of frequency estimation is to compute the *marginal probability* of the frequencies and decay rates *independent of the amplitudes*, which is

$$P(\Theta|D, I) \propto \int d\mathbf{B} P(D|\Theta, \mathbf{B}, I), \tag{A.6}$$

ignoring normalization constants. The *maximum entropy principle* assigns a Gaussian probability to the noise with finite, unknown power:

$$P(\mathbf{e}|\sigma, I) = (2\pi\sigma^2)^{-N/2} \exp\left\{-\sum_{i=1}^{N} \frac{e(t_i)^2}{2\sigma^2}\right\} \tag{A.7}$$

where $\sigma^2$ is the variance of the noise. Since the noise is equal to the data minus the model, we can derive an express for the direct probability of the data

$$P(D|\Theta, \mathbf{B}, I) = (2\pi\sigma^2)^{-N} \exp\left\{\frac{Q}{2\sigma^2}\right\}, \tag{A.8}$$

where

$$Q = d_R \cdot d_R + d_I \cdot d_I - 2\sum_{j=1}^{m} B_j[d_R \cdot U_j + d_I \cdot V_j] + \sum_{j=1}^{m}\sum_{k=1}^{m} B_j B_k[U_j \cdot U_k + V_j \cdot V_k], \tag{A.9}$$

$$U_j = \sin(\omega_j + \theta)e^{-\alpha_j t} \tag{A.10}$$

$$V_j = \cos(\omega_j + \theta)e^{-\alpha_j t} \tag{A.11}$$

and $(\cdot)$ means sum over discrete time samples. A change of function basis for the amplitude parameters

$$R_k = \sum_{j=1}^{m} \frac{U_j e_{kj}}{\sqrt{\lambda_k}} \tag{A.12}$$

$$I_k = \sum_{j=1}^{m} \frac{V_j e_{kj}}{\sqrt{\lambda_k}} \tag{A.13}$$

can diagonalize the interaction matrix into its eigenvectors $e_{kj}$ with eigenvalues $\sqrt{\lambda_k}$ (not shown here) so that each can be integrated out (marginalized). The posterior probability of the nonlinear parameters when the noise variance $\sigma$ is known becomes

$$P(\Theta|\sigma, D, I) \propto \lambda_1^{-1/2} ... \lambda_m^{-1/2} \exp\left\{\frac{m\bar{h^2}}{\sigma^2}\right\} \tag{A.14}$$

The *sufficient statistic*

$$\bar{h^2} \equiv \frac{1}{m}\sum_{j=1}^{m}(d_R \cdot R_j + d_I \cdot I_j)^2 \tag{A.15}$$

is interpreted as the *mean square projection of the data onto the model.*

If the frequency components of the model are well-separated the interaction terms in $Q$ can be neglected and the computation of the solution is drastically simplified since it reduces to a sum of solutions for single frequency components. In paper IV [17], the $\bar{h^2}$ sufficient statistic for the single decaying exponential case is shown to be proportional the *discrete Fourier power spectrum* when the data is first multiplied by an exponential function with the same decay constant (apodization):

$$\bar{h^2} = \frac{R(\omega,\alpha)^2 + I(\omega,\alpha)^2}{C(0,2\alpha)} \tag{A.16}$$

$$= \frac{1}{C(0,2\alpha)} \sum_{i=1}^{N} \left| \left\{ d_R(t_i) e^{-\alpha t_i} + i d_I(t_i) e^{-\alpha t_i} \right\} e^{i\omega t_i} \right|^2 \tag{A.17}$$

where $C(0,2\alpha) = \sum_{i=1}^{N} e^{-2\alpha t_i}$.

The determination of an optimal estimator for the amplitude $A$ of a single exponentially decaying sinusoid is worked out in paper V [18] – for the sake of brevity only the most important results are mentioned here. In the case when the the noise variance is not known independently

$$P(A|D,I) \propto \left[1 + \frac{\bar{h^2}}{2N\bar{d^2}}\right]^{(3-2N)/2}\Bigg|_{\hat{\omega},\hat{\alpha}} \tag{A.18}$$

where

$$\bar{d^2} = \frac{1}{2N}\sum_{i=1}^{N} d_R(t_i)^2 + d_I(t_i)^2 \tag{A.19}$$

is the average of the time domain data points squared and the sufficient statistic is now

$$\bar{h^2} = A^2 C(0,2\alpha) - 2A\sqrt{R(\omega,\alpha)^2 + I(\omega,\alpha)^2} \tag{A.20}$$

such that the parameters are evaluated at their maxima $\omega = \hat{\omega}$, $\alpha = \hat{\alpha}$ in the apodized Fourier power spectrum given by $R(\omega,\alpha)^2 + I(\omega,\alpha)^2$. An estimate for the amplitude with error can be derived by maximizing this probability

$$(A)_{\text{est}} = \frac{\sqrt{R(\hat{\omega},\hat{\alpha})^2 + I(\hat{\omega},\hat{\alpha})^2}}{C(0,2\hat{\alpha})} \pm \sqrt{\frac{N\bar{d^2} - [R(\hat{\omega},\hat{\alpha})^2 + I(\hat{\omega},\hat{\alpha})^2]/2C(0,2\alpha)}{C(0,2\hat{\alpha})[N-2]}} \tag{A.21}$$

# BIBLIOGRAPHY


[1] National instruments labview. `http://www.ni.com/labview`. [Online; accessed 19-February-2013].

[2] Anderson, E., Tang, Y.Y., Versek, C., Tuominen, M., Gido, S., and Watkins, J. Incorporation of functionalized metal oxides into poly (ethylene oxide) based solid polymer electrolytes for lithium-ion batteries. *Bulletin of the American Physical Society 57* (2012).

[3] Angell, C. A., Xu, W., Yoshizawa, M., Hayashi, A., Belieres, J.P., Lucas, P., and Videa, M. Chapter 2: Physical chemistry of ionic liquids, inorganic and organic, protic and aprotic. In *Electrochemical aspects of ionic liquids*, Hiroyuki Ohno, Ed., 1st ed. John Wiley and Sons, Inc., Hoboken, New Jersey, 2011, pp. 5–23.

[4] Anonymous. A basic overview of fuel cell technology. `http://americanhistory.si.edu/fuelcells/basics.htm`, 2008. Smithsonian Institution. [Online; accessed 18-February-2013].

[5] Anonymous. Why every programmer should learn python or ruby. `http://reliscore.com/blog/why-every-programmer-should-learn-python-or-ruby`, 2011. [Online blog posting *Advice Programming Programming-Languages Python Ruby Tech-Trends*; accessed 19-February-2013].

[6] Bard, Allen J., and Faulkner, Larry R. *Electrochemical methods: fundamentals and applications*, 2nd ed. John Wiley & Sons, Inc., 2001.

[7] Barker, G. C. The equivalent circuit for the electrical double-layer. *Journal of Electroanalytical Chemistry 12*, 5–6 (1966), 495–503.

[8] Basak, D., Christensen, S., Surampudi, S.K., Versek, C., Toscano, D.T., Tuominen, M.T., Hayward, R.C., and Venkataraman, D. Proton conduction in discotic mesogens. *Chem. Commun.* (2011).

[9] Basak, D., Versek, C., Harvey, J.A., Christensen, S., Hillen, J., Auerbach, S.M., Tuominen, M.T., and Venkataraman, D. Enhanced anhydrous proton conduction in binary mixtures of 1h-imidazole/1h-1, 2, 3-triazole based compounds. *Journal of Materials Chemistry 22*, 38 (2012), 20410–20417.

[10] Basak, D., Versek, C., Toscano, D.T., Christensen, S., Tuominen, M.T., and Venkataraman, D. Anhydrous proton conductivities of squaric acid derivatives. *Chemical Communications*, 48 (2012), 5922–5924.

[11] Beazley, D. M. Scientific computing with python. In *Astronomical Data Analysis Software and Systems IX*, N. Manset, C. Veillet, and D. Crabtree, Eds., vol. 216. ASP, San Fransisco, 2000, p. 49.

[12] BetaCommunityContent. Eis system using solartron 1287, fra 1255 and thelco oven. `https://decibel.ni.com/content/docs/DOC-1261`, Mar. 2007. [Online; accessed 18-February-2013].

[13] Boubour, Emmanuelle, and Lennox, R. Bruce. Insulating properties of self-assembled monolayers monitored by impedance spectroscopy. *Langmuir 16*, 9 (2000), 4222–4228.

[14] Bretthorst, G.Larry. Bayesian analysis. I. Parameter estimation using quadrature nmr models. *Journal of Magnetic Resonance (1969) 88*, 3 (1990), 533 – 551.

[15] Bretthorst, G.Larry. Bayesian analysis. II. Signal detection and model selection. *Journal of Magnetic Resonance (1969) 88*, 3 (1990), 552 – 570.

[16] Bretthorst, G.Larry. Bayesian analysis. III. Applications to nmr signal detection, model selection, and parameter estimation. *Journal of Magnetic Resonance (1969) 88*, 3 (1990), 571 – 595.

[17] Bretthorst, G.Larry. Bayesian analysis. IV. Noise and computing time considerations. *Journal of Magnetic Resonance (1969) 93*, 2 (1991), 369 – 394.

[18] Bretthorst, G.Larry. Bayesian analysis. V. Amplitude estimation for multiple well-separated sinusoids. *Journal of Magnetic Resonance (1969) 98*, 3 (1992), 501 – 523.

[19] Chen, Y., Thorn, M., Christensen, S., Versek, C., Poe, A., Hayward, R.C., Tuominen, M.T., and Thayumanavan, S. Enhancement of anhydrous proton transport by supramolecular nanochannels in comb polymers. *Nature Chemistry 2*, 6 (2010), 503–508.

[20] Christensen, S., Chen, Y., Thorn, M., Versek, C., Poe, A., Tuominen, M., Thayumanavan, S., and Hayward, R. Morphological effects on proton transport in self-assembled anhydrous polymers. *Bulletin of the American Physical Society 55* (2010).

[21] Cook, Sam. How to get the most from your lithium ion batteries. `http://www.tested.com/tech/1366-how-to-get-the-most-from-your-lithium-ion-batteries`, 2010. [Online; accessed 20-February-2013].

[22] Cukierman, Samuel. Et tu, grotthuss! and other unfinished stories: Proton transfer reactions in biological systems. *Biochimica et Biophysica Acta (BBA) - Bioenergetics 1757*, 8 (2006), 876 – 885.

[23] Frömling, T., Kunze, M., Schönhoff, M., Sundermeyer, J., and Roling, B. Enhanced lithium transference numbers in ionic liquid electrolytes. *The Journal of Physical Chemistry B 112*, 41 (2008), 12985–12990. PMID: 18800824.

[24] Gagne, Robert R., Koval, Carl A., and Lisensky, George C. Ferrocene as an internal standard for electrochemical measurements. *Inorganic Chemistry 19*, 9 (1980), 2854–2855.

[25] Garca-Coln, L. S., del Castillo, L. F., and Goldstein, Patricia. Theoretical basis for the vogel-fulcher-tammann equation. *Phys. Rev. B 40* (Oct 1989), 7040–7044.

[26] Gift, Noah. Practical threaded programming with python. `http://www.ibm.com/developerworks/aix/library/au-threadingpython`, June 2008. [Online; accessed 3-January-2013].

[27] Grahame, David C. The electrical double layer and the theory of electrocapillarity. *Chemical Reviews 41*, 3 (1947), 441–501. PMID: 18895519.

[28] Granados-Focil, Sergio, Woudenberg, Richard C., Yavuzcetin, Ozgur, Tuominen, Mark T., and Coughlin, E. Bryan. Water-free proton-conducting polysiloxanes: a study on the effect of heterocycle structure. *Macromolecules 40*, 24 (2007), 8708–8713.

[29] Harvey, Jacob A., Basak, Dipankar, Venkataraman, D., and Auerbach, Scott M. Simulating hydrogen-bond clustering and phase behaviour of imidazole oligomers. *Molecular Physics 110*, 9-10 (2012), 957–966.

[30] Haven, Y., and Verkerk, B. Diffusion and electrical conductivity of sodium ions in sodium silicate glasses. *Phys. Chem. Glasses 6* (1965), 38–45.

[31] Higami, M., Woudenberg, R. C., Granados-Focil, S., Yavuzcetin, O., Tuominen, M. T., and Coughlin, E. B. Synthesis and characterization of triazole tethered polyphosphazene for fuel cell application. *PMSE Preprints 97* (2007), 551–552.

[32] Hornak, Joseph P. The basics of nmr. `http://www.cis.rit.edu/htbooks/nmr`. [Online; accessed 22-January-2013].

[33] Isard, J.O. The haven ratio in glasses. *Journal of Non-Crystalline Solids 246*, 12 (1999), 16 – 26.

[34] Johnson, C.S. Diffusion ordered nuclear magnetic resonance spectroscopy: principles and applications. *Progress in Nuclear Magnetic Resonance Spectroscopy 34* (1999), 203 – 256.

[35] Kerssebaum, Rainer, and Salnikov, Georgy. *DOSY and Diffusion by NMR: A Tutorial for TopSpin 2.0*. Bruker BioSpin GmbH, Rheinstetten, Germany, 2006. Version 2.0.0.

[36] Kreuer, Klaus-Dieter. Proton conductivity: materials and applications. *Chemistry of Materials 8*, 3 (1996), 610–641.

[37] Kreuer, Klaus-dieter, Fuchs, A., Ise, M., Spaeth, M., and Maier, J. Imidazole and pyrazole-based proton conducting polymers and liquids. *Electrochimica Acta 43*, 10-11 (1998), 1281–1288.

[38] Macdonald, J. Ross, and Johnson, William B. Chapter 1: Fundamentals of impedance spectroscopy. In *Impedance Spectroscopy: Theory, Experiment, and Applications*, Evgenij Barsoukov and J. Ross Macdonald, Eds., 2nd ed. John Wiley and Sons, Inc., Hoboken, New Jersey, 2005, pp. 1–26.

[39] Markovitch, Omer, Chen, Hanning, Izvekov, Sergei, Paesani, Francesco, Voth, Gregory A., and Agmon, Noam. Special pair dance and partner selection: Elementary steps in proton transport in liquid water. *The Journal of Physical Chemistry B 112*, 31 (2008), 9456–9466.

[40] Martwiset, S., Woudenberg, R. C., Granados-Focil, S., Yavuzcetin, O., Tuominen, M. T., and Coughlin, E. B. Intrinsically conducting polymers and copolymers containing triazole moieties. *Solid State Ionics 178*, 23 (2007), 13981403.

[41] Martwiset, Surangkhana, Yavuzcetin, Ozgur, Thorn, Michael, Versek, Craig, Tuominen, Mark, and Coughlin, E. Bryan. Proton conducting polymers containing 1h-1,2,3-triazole moieties. *Journal of Polymer Science Part A: Polymer Chemistry 47*, 1 (2009), 188–196.

[42] Mauritz, Kenneth A., and Moore, Robert B. State of understanding of nafion. *Chemical Reviews 104*, 10 (2004), 4535–4586.

[43] Miranda, D., Versek, C., Tuominen, M., Thayumanavan, S., Watkins, J., and T., Russell. Cross-linking of ordered pluronic/ionic liquid blends for solid polymer electrolytes. *Bulletin of the American Physical Society 57* (2012).

[44] Morgan, H., Pethig, R., and Stevens, G. T. A proton-injecting technique for the measurement of hydration-dependent protonic conductivity. *Journal of Physics E: Scientific Instruments 19*, 1 (1986), 80.

[45] Nagamani, C., Versek, C., Thorn, M., Tuominen, M.T., and Thayumanavan, S. Proton conduction in 1h-1,2,3-triazole polymers: Imidazole-like or pyrazole-like? *Journal of Polymer Science Part A: Polymer Chemistry 48*, 9 (2010), 1851–1858.

[46] Nagamani, C., Viswanathan, U., Versek, C., Tuominen, M.T., Auerbach, S.M., and Thayumanavan, S. Importance of dynamic hydrogen bonds and reorientation barriers in proton transport. *Chemical Communications* (2011).

[47] Raistrick, Ian D., Franceschetti, Donald R., and Macdonald, J. Ross. Chapter 2: Theory. In *Impedance Spectroscopy: Theory, Experiment, and Applications*, Evgenij Barsoukov and J. Ross Macdonald, Eds., 2nd ed. John Wiley and Sons, Inc., Hoboken, New Jersey, 2005, pp. 1–26.

[48] Royce, John R. Industry insights: Examining the risks, benefits and trade-offs of todays lims. *Scientific Computing* (2010). [Online; accessed 2-January-2013].

[49] Sadkowski, A. On the ideal polarisability of electrodes displaying cpe-type capacitance dispersion. *Journal of Electroanalytical Chemistry 481*, 2 (2000), 222 – 226.

[50] Sahu, A.K., Pitchumani, S., Sridhar, P., and Shukla, A.K. Nafion and modified-nafion membranes for polymer electrolyte fuel cells: An overview. *Bulletin of Materials Science 32* (2009), 285–294.

[51] Sanghi, S., Willett, E., Versek, C., Tuominen, M., and Coughlin, E.B. Physicochemical properties of 1,2,3-triazolium ionic liquids. *RSC Advances 2*, 3 (2012), 848–853.

[52] Scharfenberger, G., Meyer, W. H., Wegner, G., Schuster, M., Kreuer, K. D., and Maier, J. Anhydrous polymeric proton conductors based on imidazole functionalized polysiloxane. *Fuel Cells 6*, 3-4 (2006), 237250.

[53] Schuster, M, Meyer, W.H, Wegner, G, Herz, H.G, Ise, M, Schuster, M, Kreuer, K.D, and Maier, J. Proton mobility in oligomer-bound proton solvents: imidazole immobilization via flexible spacers. *Solid State Ionics 145*, 14 (2001), 85 – 92. Proceedings of the 10th International Conference on Solid State Protonic Conductors.

[54] Schuster, Martin F.H., and Meyer, Wolfgang H. Anhydrous proton-conducting polymers. *Annual Review of Materials Research 33*, 1 (Aug. 2003), 233–261.

[55] Schuster, Michael, Kreuer, Klaus-Dieter, Steininger, Hanna, and Maier, Joachim. Proton conductivity and diffusion study of molten phosphonic acid h3po3. *Solid State Ionics 179*, 1516 (2008), 523 – 528.

[56] Singh, Kundan. Why python? `http://www.39peers.net/index.php?option=com_content&view=article&id=47:why-python&catid=31:general&Itemid=46`, 2008. [Online blog posting; accessed 19-February-2013].

[57] Tipler, Paul A., and LLewellyn, Ralph A. Chapter 11: Nuclear physics. In *Modern Physics*, 3rd ed. W. H. Freeman and Company, New York, NY, 1999.

[58] Tsai, T., Versek, C., Thorn, M., Tuominen, M., and Coughlin, E. Block copolymers containing quaternary benzyl ammonium cations for Alkaline Anion Exchange Membrane Fuel Cells (AAEMFC). *ACS Books, Symposium Series Chapter* (submitted 2011).

[59] Tsai, T.H., Maes, A.M., Vandiver, M.A., Versek, C., Seifert, S., Tuominen, M., Liberatore, M.W., Herring, A.M., and Coughlin, E.B. Synthesis and structure–conductivity relationship of polystyrene-block-poly (vinyl benzyl trimethylammonium) for alkaline anion exchange membrane fuel cells. *Journal of Polymer Science Part B: Polymer Physics* (2012).

[60] Versek, C., Thorn, M., and Tuominen, M.T. Using open-source scripting languages for rapid-development of informatics capabilities. *Presented at Nanoinformatics 2010 Conference, Arlington VA* (2010).

[61] Walker, C.N., Versek, C., Touminen, M., and Tew, G.N. Tunable networks from thiolene chemistry for lithium ion conduction. *ACS Macro Letters 1*, 6 (2012), 737–741.

[62] Woudenberg, R.C., Yavuzcetin, O., Tuominen, M.T, and Coughlin, E.B. Intrinsically proton conducting polymers and copolymers containing benzimidazole moieties: glass transition effects. *Solid State Ionics 178* (2007), 11351141.

[63] Woudenberg, Richard C. *Anhydrous proton conducting materials for use in high temperature polymer electrolyte membrane fuel cells*. PhD thesis, University of Massachusetts Amherst, January 2007. Paper AAI3289247.

[64] Wright, Peter V. in polymer electrolytes for lithium batteries. *MRS bulletin* (2002), 597.

[65] Wu, D.H., Chen, A.D., and Johnson, C.S. An improved diffusion-ordered spectroscopy experiment incorporating bipolar-gradient pulses. *Journal of Magnetic Resonance, Series A 115*, 2 (1995), 260 – 264.

[66] Zhou, Zhen, Li, Siwen, Zhang, Yuelan, Liu, Meilin, and Li, Wen. Promotion of proton conduction in polymer electrolyte membranes by 1h-1,2,3-triazole. *Journal of the American Chemical Society 127*, 31 (Aug. 2005), 10824–5.